ON THE DESIGN OF LENS ARRAY ARCHITECTURES FOR THE TIFUUN IMAGING SPECTROMETER

Alexandra Mavropoulou

Student Number: 5493579

Thesis Advisor: Prof. dr. Nuria Llombart
Thesis Supervisor: Dr. Shahab Oddin Dabironezare

TUDelft

The work presented in this thesis was performed at:

Tera-Hertz Sensing Group

Department of Microelectronics

Faculty of Electrical Engineering, Mathematics and Computer Science

Delft University of Technology

Preface

In the framework of this MSc thesis, the analysis and design guidelines for part of the quasi-optical system of a proposed astronomical instrument, called TIFUUN, are presented. The TIFUUN instrument is an imaging spectrometer, planned to be placed in the ASTE telescope to perform ground-based astronomical observations in the mm-submm wavelength regime. Part of the instrument development involves the design of the quasi-optical system coupling the radiation from the telescope's main dish to the spectrometer array. In this thesis, the focal plane array of antennas, as well as the first component of the quasi-optical chain are analyzed and two different design approaches are presented, as candidate geometries. Each of them satisfies the requirements of different science surveys targeted by TIFUUN. The first examined architecture is comprised of a focal plane array of on-chip feeding elements under a single hyper-hemispherical lens, which is then coupled geometrically to a hyperbolic lens. The second geometry is instead comprised of an array of integrated elliptical lenses, with a single on-chip feeding element per lens, diffractively coupled to a hyperbolic lens. The methodologies to efficiently analyze these kinds of geometries are Geometrical Optics (GO) combined with analysis in reception for the first design approach and Coherent Fourier Optics (CFO) for the second one. During the design process, the performance of both architectures is optimized throughout the field of view, using methodologies to correct for phase aberrations, such as feed displacement inside the lenses and symmetric shaping of dielectric surfaces. The design guidelines provided and insights obtained during this MSc project will be utilized to develop the quasi-optical system of the TIFUUN instrument, within the limited space of its cryostat.

Acknowledgements

On the Design of Lens Array Architectures for the TIFUUN Imaging Spectrometer

This thesis is submitted in partial fulfilment of the requirements for the degree of:

MASTER OF SCIENCE

in

ELECTRICAL ENGINEERING,

Track: Wireless Communication & Sensing

by

Alexandra Mavropoulou

Student Number:	5493579
Defense Date	July 19, 2023
Thesis Committee:	Prof. dr. Nuria Llombart
	Dr. Shahab Oddin Dabironezare
	Dr. ir. Rob Remis

Contents

Chapter 1. Introduction

1.1. Terahertz Astronomy

The plethora of astronomical phenomena observable in the submillimetre and far infrared frequency regimes have driven the development of highly sensitive detectors and instruments for THz astronomy. Dust and gas absorb visible light, rendering dust-rich environments invisible to optical telescopes. On the contrary, such environments are transparent in far-infrared (FIR) and terahertz (THz) frequencies, and on top of that, FIR/THz light is radiated by the products of star formation, either in the form of dust black body radiation (continuum spectrum emitted by dust), or in the form of emission lines. Therefore, observing dust obscured and line-emitting galaxies, as well as mapping the evolution of star formation throughout the cosmic history are some of the targeted applications of mm and submm-wave astronomy.

Some of the brightest spectral lines probing star formation are $[C_{II}], [H_I]$ and $[CO]$ [1], all being powerful diagnostics of physical and chemical conditions in astronomical objects [1]. Even though the spectral signatures of some of those lines cannot be directly observed by Earth-based instruments due to the frequency dependency of atmospheric absorption/emission, if radiated by distant objects (both in space and in time), the expansion of the universe can contribute to their detection by ground-based instruments. In particular, along with the extension of the interstellar space between astronomical objects, the travelling light is also stretched, which leads to the extension of the observed wavelength, a phenomenon called cosmological redshift (Eq. 1.1).

$$z = \frac{\lambda_{obs}}{\lambda_{emitted}} - 1 \tag{1.1}$$

where λ_{obs} is the observed wavelength and $\lambda_{emitted}$ is the wavelength emitted by the source.

The cosmological redshift is crucial for astronomical observations, since it can change the observed wavelength in such a way that light from a certain source penetrates the Earth's atmosphere (in other words falls into an Earth's atmospheric window), and thus it can be detected by proper instruments (i.e. λ_{obs} could penetrate the atmosphere, while $\lambda_{emitted}$ might not). High redshift galaxies for example can be probed from Earth-based instruments using the bright $[C_{II}]$ line, falling within Earth's atmospheric windows due to redshift.

To further investigate the ever-rising questions of mm-wave astronomy, large format imaging arrays and broad-band spectrometers are required to complement the high spatial and spectral resolution of mm/submm interferometers such as ALMA (Atacama Large mm/submm Array) and NOEMA (Northern Extended Millimeter Array). Even though interferometry has provided the opportunity for extreme spatial resolution, with the Event Horizon Telescope [2] pushing the limits of the achieved resolution by forming an Earth-sized equivalent telescope, coherent detectors lack in scalability, while also featuring relatively narrow bandwidth. Thus, due to the abundance of targeted surveys that require not high resolution, but rather

---

[1] $[C_{II}]$ line, at 1.9THz is often the brightest in a sub-mm galaxy spectrum and it indicates emissions from C^+, due to ion's fine structure transitions.

$[CO]$ lines and its harmonics at $115 \times n$ GHz are produced by rotational transitions of the CO molecule and act as tracers of $[H_2]$, which hardly radiates within cold interstellar matter.

$[H_I]$, at 21cm wavelength is emitted by interstellar hydrogen atoms due to atomic transitions of an electron between two hyperfine levels of the hydrogen 1-s ground state and thus probes the dark ages before the formation of stars.

wideband/ large field of view instruments, attention is also driven towards the development of multi-pixel, sensitive and wideband detector arrays.

1.2. Detector Technologies & Spectroscopy

Although there are multiple detector technologies that can reach the sensitivity required by the aforementioned instruments, in most cases multiplexing is challenging, if at all possible. Some examples of detectors achieving sufficient sensitivity are, Quantum Capacitance Detectors (QCD) [3]- [4], Transition Edge Sensors (TES) [5], small-volume hot-electron bolometers [6] and Microwave Kinetic Inductance Detectors (MKID) [7]. For array scaling, combined with high sensitivity, MKIDs are the best candidate [8]. This derives from their inherent ability for large-scale multiplexing in the frequency domain, in contrast to other detector technologies.

However, MKIDs are direct detectors, meaning that no phase information is restored post-detection and the spectral properties of the signal can only be recovered by means of filtering prior to the power detection. As a result, to achieve the requirements of a large format array of sensitive spectrometers, the instrument design is directed towards an Integral Field Unit (IFU), i.e. a two dimensional array of spectrometers that instantaneously measures the spectrum of all spatial pixels formed in the sky, [9]. The basic principle of operation of an IFU is showcased in Figure 1-1. To realize such an instrument in a compact manner, i.e. in a single commercial wafer, integrated (on-chip) spectrometers are required. Superconductor technology can be employed here as well, for the development of Integrated Superconducting Spectrometers (ISS) [10].

However, for detecting THz radiation, except for a readout line and one or more spectrometers, a radiation coupling system is also needed. For coupling the radiation, while also preserving the spectral information of the source, antenna coupling is required. If a broadband antenna is employed, "multicolor" detection becomes possible, through post reception filtering of the THz radiation.
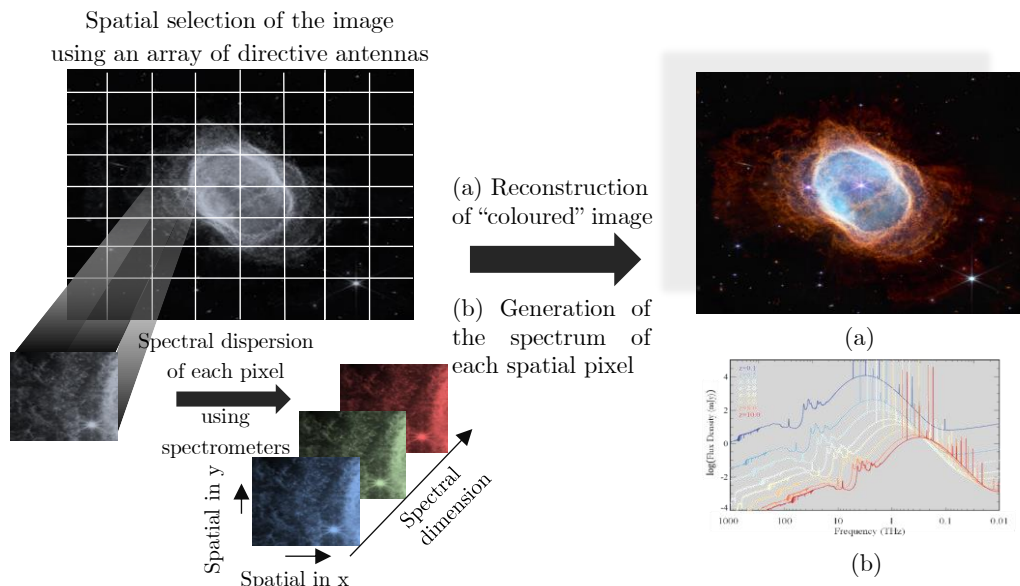
Figure 1-1. Principle of operation of an Integral Field Unit (IFU). The Field of View (FoV) of the instrument is divided into spatial pixels, with the use of an array of directive antennas. The received signal from each pixel is divided into spectral channels. In this manner, a "coloured" image can be reconstructed, and the spectrum of each spatial pixel can be generated. Image Credit: NASA / ESA / CSA / STScI, James Webb Space Telescope, Southern Ring Nebula.

To conclude, an Integral Field Unit that can satisfy the requirements of future far infrared astronomy challenges is comprised of an array of wideband antennas to couple the radiation incident on the telescope to the circuit (N_{ant} antennas per IFU), an integrated spectrometer with N_{ch} channels, following each antenna, and a highly sensitive detector, following each of the spectrometer's channels ($N_{det} = N_{ant} \times N_{ch}$ detectors per IFU), as illustrated in Figure 1-2. To satisfy the required resolution and scalability, integrated superconducting spectrometers in combination with Microwave Kinetic Inductance Detectors can be utilized.

Such a system is currently being developed as a collaboration of Delft University of Technology, the Netherlands Institute for Space Research (SRON) and Institut Néel, as a continuation of the DESHIMA project [10], [11]. The project is named "Terahertz Integral Field Unit with Universal Nanotechnology (TIFUUN)" and includes the design of multiple IFUs that are planned to perform a number of astronomical surveys.

1.3. Antenna Coupled Detector Systems

For Earth-based astronomy applications, the detector systems are coupled to large telescopes, to take advantage of their high gain and narrow beamwidth. Thus, part of the instrument design includes the development of a Quasi-Optical (QO) system to couple the radiation all the way from the telescope's main dish to the detectors. In this case, due to the superconducting nature of the detector technology utilized, the IFUs need to be cryogenically cooled, meaning that the telescope's optical chain needs to be refocused inside the cryostat hosting the detectors. Therefore, the QO chain is comprised of the telescope's main dish setup (e.g. Cassegrain or Gregorian), the warm optics inside the telescope's cabin and the cold optics inside the cryostat hosting the IFUs. At the focal plane of this QO chain, an array of antennas is placed, coupling the radiation to the IFUs.

To satisfy the requirements of future astronomical surveys, this QO system should operate within a wide bandwidth and feature a wide field of view. In the framework of the TIFUUN project, the wide bandwidth enables the analysis of the spectral information of the source. However, even in applications where spectroscopy is not required, increasing the bandwidth can contribute to higher sensitivity [12]. Regarding the widening of the field of view, it significantly improves the image acquisition speed, by minimizing the required telescope repointings. Therefore, the antenna feeder of such a QO system should feature wideband characteristics and allow for covering wide fields of view.
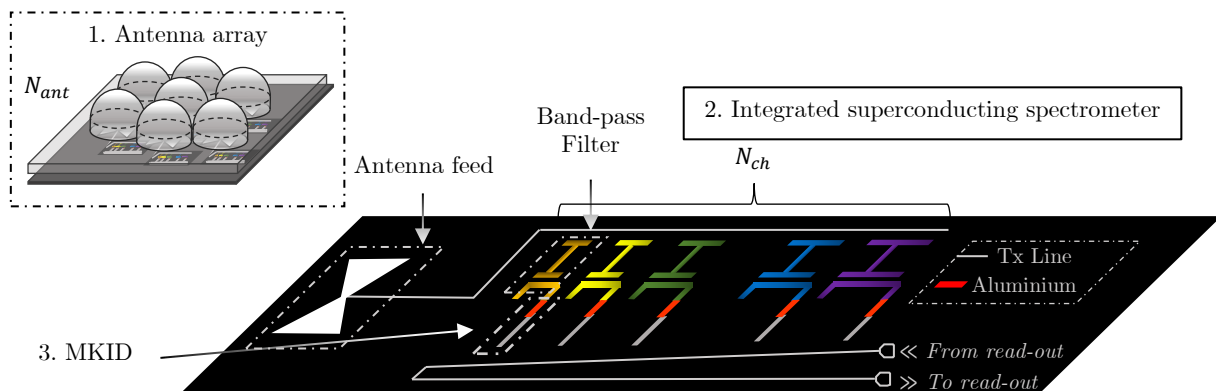
Figure 1-2. An Integral Field Unit operating in the submm frequency regime, consisting of: 1. An antenna array, with N_{ant} elements per IFU, 2. An integrated superconducting spectrometer (ISS), with N_{ch} spectral channels, following each antenna and 3. A Microwave Kinetic Inductance Detector (MKID), following every channel of the ISS. In total, there are $N_{det} = N_{ant} \times N_{ch}$ detectors per IFU.

Even though there is an abundance of wideband antennas proposed in literature; most of them do not satisfy the demanding requirements for efficient illumination of large f-number quasi-optical systems, with wide scanning capabilities[2], while also exhibiting difficulty in integration on a chip. Antennas such as the Eleven antenna [13], quadruple-ridged flared horns [14], corrugated horns [15] and Vivaldi antennas [16] show promising performance as reflector feeds, but still do not comply with the system's requirements. First and foremost, none of the proposed feeds can be integrated into a chip design. Furthermore, in mm/submm wavelengths, the fabrication of an array of antennas such as Eleven antennas, flared horns or Corrugated horns is challenging. On top of that, in order for a horn antennas' beamwidth to not vary with frequency, its length should be significant [13]. As for the Vivaldi antennas, even though they are matched within an ultra-wide bandwidth, when placed into tightly spaced arrays, they suffer from strong mutual coupling [17].

Lens antennas on the other hand can be integrated on chip together with the detector and are simpler in the fabrication, even in the mm-submm frequency regime. In terms of impedance matching, if the feeding element is chosen accordingly, a lens-based wideband design can be targeted. To increase the aperture efficiency bandwidth of the whole QO chain, geometrical coupling between QO components can be used where possible. Regarding the wide field of view requirement, Fly's eye lens arrays have shown promising performance for large format focal plane arrays (FPAs), especially if combined with synthesis techniques to optimize the shape and size of the off-focus lenses [18]- [19]. Alternatively, multi-lens architectures combined with proper shaping of the involved surfaces can be utilized to correct both for phase aberrations and for spill-over losses while scanning [20], enlarging the field of view.

Having introduced some of the needs of modern astronomical instrumentation, as well as some background, the rest of this document focuses on the specific case of the TIFUUN project and more specifically towards the design of its quasi – optical system.

1.4. Introduction to the TIFUUN Project

One of the challenges in mm and sub-mm astronomy lies in the mapping of statistically large cosmic volumes with complete spectral information. To address this, the TIFUUN project aims on developing IFUs, operating in the mm-submm frequency regime, with high sensitivity, a wide instantaneous bandwidth up to 1:2 and a sufficiently high spectral resolving power. In particular, to cover a variety of astronomical surveys, the TIFUUN system will host multiple IFUs, two of which will operate simultaneously each time. This is feasible due to the use of a polarizing grid, which directs the two polarizations in two different directions, allowing the detection of the two orthogonal polarizations, completely independently from one another, as shown in Figure 1-3. This "Plug and Play" compatibility, facilitates different science cases, by observing the same sky field simultaneously with two different instruments, or by doubling the imaging speed if two identical IFUs are employed at the same time.

---

[2] Scanning with a quasi-optical system is defined as receiving an EM wave incident on the primary quasi-optical component (telescope in this case) from an angular region different than broadside. The broadside direction is always aligned with the axis of the primary quasi-optical component. This can be achieved by laterally displacing the feeding elements in a focal plane, which inherently degrades their performance. Therefore, the scanning capabilities of a quasi-optical antenna system are characterized through the degradation in the performance of an off-broadside element, compared to that of the central one, pointing at broadside.
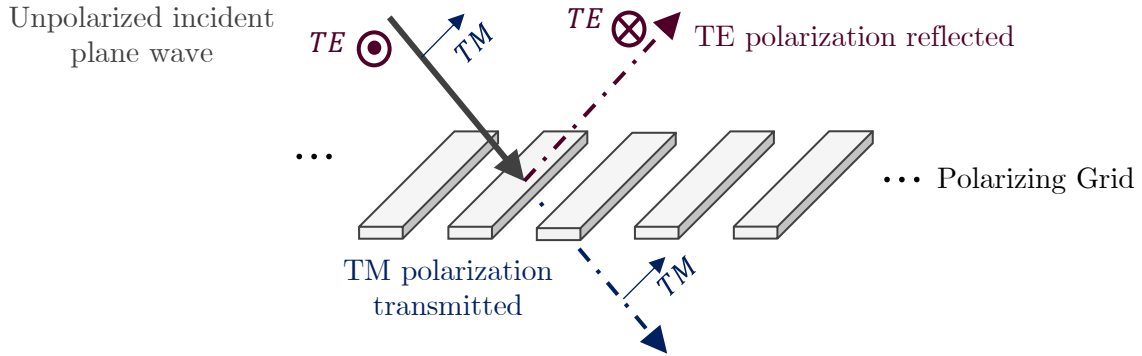
Figure 1-3. Basic principle of operation of an optical polarizing grid. Two orthogonal polarizations are redirected in two different directions, where two IFUs with different polarizations can be placed and operate simultaneously.

Besides the inclusion of the polarizing grid, there are more aspects of the system that drive the antenna and quasi – optical system design. Some of those aspects are discussed in this section, together with top-level proposed techniques to approach each challenge.

The first property of the TIFUUN system, which is of vital importance for the design of the radiation coupling system is the **"Plug-and-Play" compatibility**, meaning that IFUs with different requirements, in terms of bandwidth and field of view, need to couple to the same quasi – optical system. To achieve this, it is convenient to introduce a building block for each IFU, which consists of, not only the focal plane array of antennas, but also a focusing component (primary quasi-optical component of the building block). This way, the design approach of the FPA, the focal distance to diameter ratio (or usually referred to as f-number - $f_\#$), as well as the physical dimensions of the focusing component, can vary between the different IFU designs. The f-number can be utilized as a parameter to optimize both the performance of the broadside element of the focal plane array, as well as the scanning performance of the total quasi – optical system. The physical dimensions on the other hand can be adjusted depending on the frequency band of interest, as well as the requirements in terms of scanning.

To decide on the type of focusing component utilized, one should also take into account the **available physical space** inside the cryostat, where the focusing component, the focal plane array and the polarizing grid are positioned. Considering that, it is more convenient to realize the focusing component with a transmitting element, instead of a reflecting one. For this reason, a free-standing plano-hyperbolic lens is chosen as the focusing element.

Another important aspect of the design of the quasi – optical system for the TIFUUN project, is related to **the number of antennas operating simultaneously** on each IFU and thus the field of view that can be covered instantaneously by one instrument. To define those, it is important to recall the structure of an Integral Field Unit. An IFU is comprised of a focal plane array of antennas where each antenna is followed by a spectrometer. Therefore, one can characterize the IFU through the number of spectrometer pixels, defined here as spaxels, $N_{spaxels}$. Subsequently, depending on the bandwidth of operation, as well as the spectral resolution of each instrument, each spectrometer is divided into N_{ch} spectral channels (Figure 1-2). The information transmitted through each of the channels is received with a detector (MKID). Hence, the number of detectors per IFU is calculated as the product of the number of spaxels and the number of channels per spectrometer (Eq. 1.2).

$$N_{det} = N_{spaxels} \cdot N_{ch}, \qquad (1.2)$$

Since the number of MKIDs that can be read out by a single transmission line is limited, the maximum number of spaxels (or the maximum number of antennas) hosted by an IFU might be limited by the required spectral resolving power. For instance, when the required spectral

resolution is very high, only a small FPA can be supported by the system, decreasing the instantaneous field of view coverage.

Finally, it has already been discussed that **wideband and wide field of view** architectures need to be developed to satisfy the system requirements. In the framework of this thesis, different lens-based quasi-optical systems are examined, with the aim of achieving wideband and wide-scanning properties.

To conclude, the proposed building block of an IFU hosted by the TIFUUN system is comprised of a focal plane array of antennas, coupled to a free-standing hyperbolic lens and is placed inside a cryostat, at one of the positions created by the polarizing grid (Figure 1-4). This means that the antennas should be **linearly polarized**. It should be noted that this building block is only part of the cold optics, since to facilitate the operation of the cryostat, a converging wave should enter its aperture opening, which is subsequently converted to a locally plane wave, incident on the polarizing grid, as shown in Figure 1-4.

1.5. Objectives of this Thesis

The goal of this thesis is to examine, provide design guidelines and compare candidate geometries for the building block of an Integral Field Unit hosted by the TIFUUN system. As already discussed in this introductory chapter, to meet the requirements of the science goals of this project, the quasi-optical system (including the antennas), coupling the radiation from the telescope to the detectors should operate over a wide bandwidth, while also featuring wide scanning capabilities. To achieve a good trade-off between bandwidth and scanning, two approaches are investigated in this thesis.

Firstly, a hyperbolic lens, geometrically coupled to a hyper-hemispherical lens and fed by a focal plane array of feeding elements, is examined. This geometry allows for a nearly frequency independent performance for the central element of the array, while its scanning performance is inherently limited. The multiple lens surfaces of this architecture provide multiple degrees of freedom for symmetrically shaping the lenses to improve the scanning performance in all azimuthal planes, which is also explored in the framework of this work.
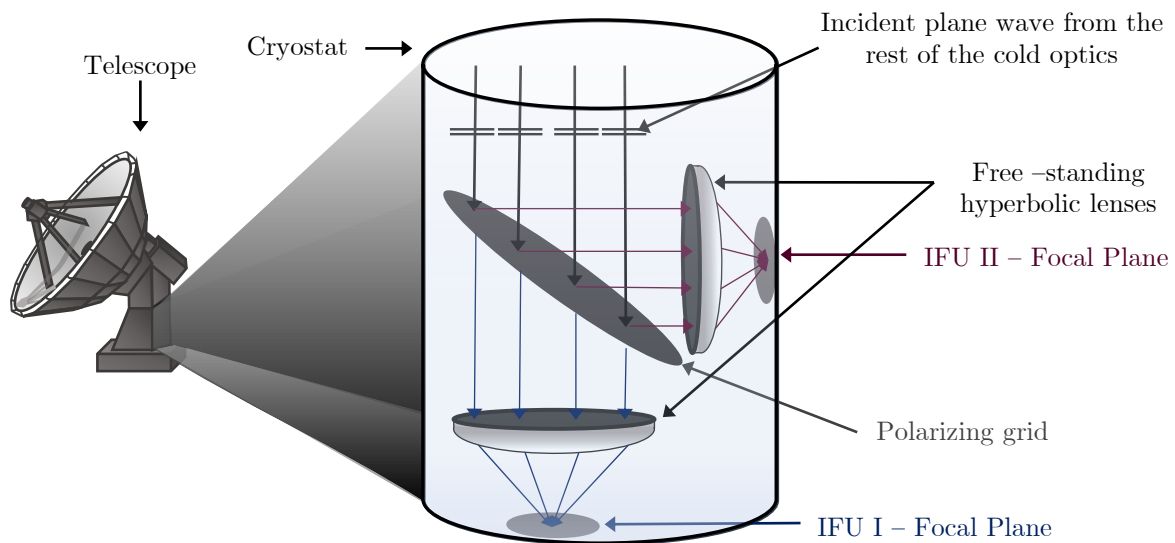
Figure 1-4. Overview of the proposed cold optics design for the TIFUUN system. Inside the cryostat, there is a polarizing grid, re-directing the two orthogonal polarizations into different regions, where the building block of an IFU is placed. The TIFUUN building block is comprised of a free-standing hyperbolic lens and a focal plane array of antennas.

The second geometry explored is instead based on a hyperbolic lens with a focal plane array of small integrated lenses, intrinsically trading off the frequency independent operation, for a better scanning performance. To correct for phase errors while scanning, lateral displacement of the feeding elements of the off-focus lenses is exploited in this case. For both architectures, the design process of the quasi-optical systems, as well as the feeding elements is presented in the framework of this work. To conclude the discussion, the two design approaches are compared against each other and linked to specific science cases targeted by the TIFUUN project, depending on the requirements of each survey as well as the capabilities of each architecture.

The outline of the thesis is provided in the following section (1.6).

1.6. Outline

In **Chapter 2**, the theoretical framework for the analysis of the candidate geometries for the building block of an Integral Field Unit hosted by TIFUUN is set. In particular, the analysis of a chain of QO components is divided into two main steps, the transmission/reflection through the involved surfaces and the coupling between QO components. Regarding the latter, depending on the proximity of the source to caustic (focal) points, it can be characterized as geometric or diffractive. To render the analysis of both types of coupling time efficient, two analysis methodologies are discussed, namely a combination of geometrical optics (GO) propagation with an analysis in reception technique for the geometrically coupled system and the Coherent Fourier Optics (CFO) methodology for the diffractively coupled system.

In **Chapter 3**, the geometrically coupled architecture, comprised of a hyperbolic lens, a hyper-hemispherical lens and a focal plane array of feeding elements, is analysed. The analysis methodologies presented in Chapter 2 are applied to the specific case of this geometry and before proceeding to the actual design, some theoretical limitations of this configuration are discussed. Subsequently, a preliminary design, fed by an ideal feeding element, with a Gaussian shaped far field is examined. Taking into account the deductions derived through this Gaussian-fed architecture, the actual feeding element, i.e. a tapered leaky wave slot, is designed. Finally, to improve the scanning performance of this geometry, symmetric shaping of the lens surfaces is applied.

In **Chapter 4**, the analysis of the diffractively coupled architecture, comprised of a hyperbolic lens and a focal plane array of small focal lenses, is presented. Similarly to Chapter 3, the analysis methodologies presented in Chapter 2 are applied to this geometry. Afterwards, a discussion about the difference between hyper-hemispherical and elliptical lenses of various diameters is presented, in order to facilitate the choice of the type of focal lens utilized in this design. Once the type of lens is selected, as a first step in the design phase, the quasi-optical system is again fed by an ideal feeding element, with a Gaussian shaped far field in order to identify the desired properties of the actual feeding element (tapered leaky wave slot). With this in mind, the feeding element is designed and laterally displaced inside the off-focus lenses, if necessary, to improve the scanning performance.

In **Chapter 5**, the specific science cases targeted by TIFUUN are introduced and the criteria of selecting one design approach over another for the quasi-optical system design are discussed. To facilitate the choice of the optimal geometry, the two designs presented in Chapter 3 and Chapter 4 are compared against each other in section 5.1, both as single element architectures and in an array configuration. The two designs are then applied to indicative surveys, where their potential as building blocks of an Integral Field Unit hosted by TIFUUN is showcased.

The conclusions and future work are presented in **Chapter 6**.

Chapter 2.
Chains of Quasi-Optical Components - Types and Analysis Methodologies

The analysis of chains of transmitting Quasi-Optical Components is comprised of two main steps, the transmission of EM fields through the involved surfaces as well as their propagation between successive surfaces. Regarding the step of the transmission, it is performed by assuming locally flat interfaces and multiplying the incident field with a transmission dyad ($\bar{\bar{\tau}}$), which takes into account both the change in amplitude and the change in polarization a field is experiencing when interacting with the examined structure (Eq. 2.1).

$$\vec{E}_{Tx} = \bar{\bar{\tau}} \cdot \vec{E}_{inc}, \tag{2.1}$$

The transmission (Tx) coefficients are derived either through directly applying boundary conditions on Maxwell's Equations (Fresnel coefficients), or through transversalizing the original problem and representing it through an equivalent transmission line problem. The latter also facilitates the inclusion of a simplified model of matching layers in the examined interfaces. As for the change in polarization between the incident and transmitted field, this depends on the curvature of the surface. The complete process is analytically described in Appendix B.

For the propagation of the fields between two surfaces, one can consider one as the radiating aperture and the other as the receiving one. Subsequently, by employing a Physical Optics (PO) approach, the Surface Equivalence Theorem can be utilized to replace the radiating surface with an equivalent current distribution. Then, the field propagating to the receiving aperture can be derived by convoluting the current distribution with the Green's function of the medium. Depending on the distance and electrical dimensions of the involved surfaces, this process can also be simplified, eliminating the need for any integration, using a Geometrical Optics (GO) approximation. The Geometrical Optics approximation can be applied, provided that the radiating and receiving apertures are electrically large and far from any caustic (focal) points. If the GO approximation is applicable, the coupling between successive components is referred to as geometric, otherwise as diffractive. Both are discussed in detail in the following section.

2.1. Geometric and Diffractive Coupling

Based on the Surface Equivalence Theorem [21], the field radiated by any source, can be calculated by substituting the source with a current distribution on top of an arbitrary closed surface, radiating in the absence of the source (Figure 2-1). In the Love's Formulation of the theorem, this equivalent current distribution can be calculated by applying the boundary conditions on the equivalent closed surface, such that the electric and magnetic fields are zero inside the surface and equal to the radiation produced by the actual source outside of it (Eq. 2.2). This way both the boundary conditions, as well as the Uniqueness Theorem are satisfied.
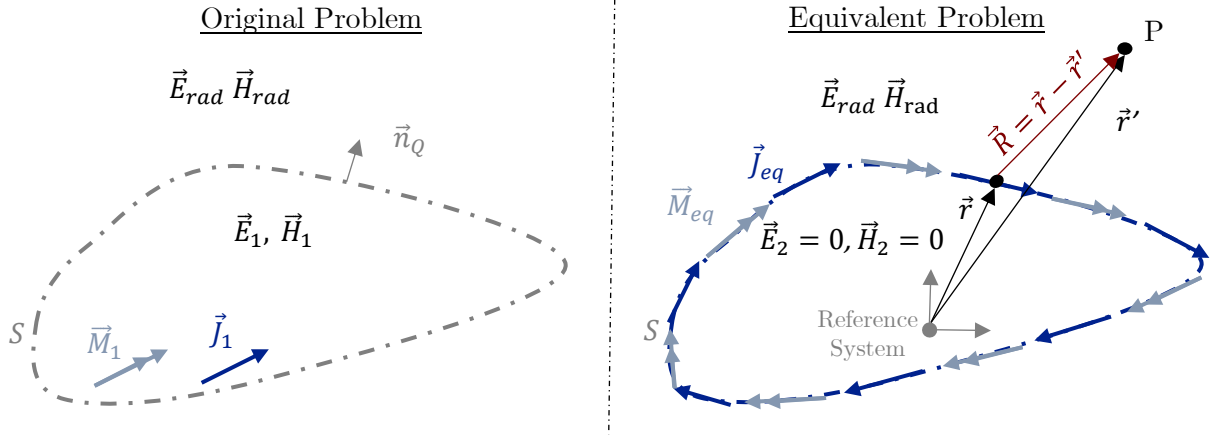
Figure 2-1. Surface Equivalence Theorem visualization (Love's Formulation). On the left, the original problem consists of a number of sources surrounded by an imaginary closed surface S. On the right, everything within the closed surface S is substituted by a set of suitable equivalent surface currents, such that the boundary conditions are satisfied. The field outside the surface S is the same in both problems, to satisfy the Uniqueness Theorem.

$$\vec{J}_{eq}(\theta,\varphi) = \hat{n}_Q \times \vec{H}(r,\theta,\varphi)|_S$$
$$\vec{m}_{eq}(\theta,\varphi) = -\hat{n}_Q \times \vec{E}(r,\theta,\varphi)|_S \tag{2.2}$$

where $\hat{n}_Q$ is the normal vector on the auxiliary surface (S) and $\vec{E}|_S, \vec{H}|_S$ are the electric and magnetic field radiated by the source and evaluated on the surface S.

Once this current distribution is known, the field radiated by the original sources can be evaluated at any observation grid through the convolution between the Green's Function of the medium in the absence of the original source, and the equivalent currents of Eq. 2.2, as expressed in Eq. 2.3.

$$\vec{E}_{rad}(\vec{r}) = \iint_S \bar{\bar{G}}_{ej}(\vec{r} - \vec{r}') \cdot \vec{J}_{eq}(\vec{r}')dS' + \iint_S \bar{\bar{G}}_{em}(\vec{r} - \vec{r}') \cdot \vec{m}_{eq}(\vec{r}')dS', \tag{2.3}$$

where $\vec{r}$ and $\vec{r}'$ correspond to the observation and the source grids respectively, and dS' describes the domain of integration (Figure 2-1).

If the medium outside the surface S is free space (unbounded, isotropic and homogenous medium), the spatial Green's functions can be expressed as in Eq. 2.4 - 2.5.

$$\bar{\bar{G}}_{ej}^{FS}(\vec{r} - \vec{r}') = -j\omega\mu \left[\bar{\bar{I}} - \frac{1}{k^2}\vec{\nabla} \cdot \vec{\nabla}\right] \frac{e^{-jk|\vec{r}-\vec{r}'|}}{4\pi|\vec{r}-\vec{r}'|}, \tag{2.4}$$

$$\bar{\bar{G}}_{em}^{FS}(\vec{r} - \vec{r}') = -\left[\vec{\nabla} \times \bar{\bar{I}}\right] \frac{e^{-jk|\vec{r}-\vec{r}'|}}{4\pi|\vec{r}-\vec{r}'|}, \tag{2.5}$$

Focusing on the EM radiation far from the source region, the Green's functions of Eq. 2.4 - 2.5 can be approximated using only their radiative parts, i.e. $\vec{\nabla} \cong -jk\hat{R}$, $\hat{R} = \frac{\vec{r}-\vec{r}'}{|\vec{r}-\vec{r}'|}$,. The field of Eq. 2.3 can then be simplified through the expression of Eq. 2.6.

$$\vec{E}_{rad}(\vec{r}) = \iint_S \left\{jk\left[\hat{R} \times \vec{m}_{eq}(\vec{r}')\right] - j\omega\mu\left[\vec{J}_{eq}(\vec{r}') - \left\{\hat{R} \cdot \vec{J}_{eq}(\vec{r}')\right\} \cdot \hat{R}\right]\right\} \frac{e^{-jk|\vec{r}-\vec{r}'|}}{4\pi|\vec{r}-\vec{r}'|} dS', \tag{2.6}$$

In this representation, the field on the observation grid is derived through spatial integration on the source surface (Eq. 2.6), meaning that in order to calculate the field at any observation point P, one takes into account the contribution of the whole field distribution over the equivalent source S. If the involved surfaces feature curvatures large in terms of

wavelength and are far from any caustic points (focal points), the integral of Eq. 2.6 is dominated by the contribution of the direct ray, i.e. the point P_0 on the surface S, for which the ray connecting it with the observation point P is parallel to the direction of propagation of the field $\left(i.e., \ \hat{R} = \frac{\vec{r}-\vec{r}'}{|\vec{r}-\vec{r}'|} = \hat{k}\right)$, as shown in Figure 2-2. This means that the integral can be asymptotically evaluated, eliminating the need for any integration [22], [23].

The above mentioned approximation, where the field is dominated by the ray picture is referred to as Geometrical Optics (GO). To calculate the field on an observation grid $\vec{r}$ with this technique, one can start the analysis by expressing the field distribution on the surface S as an astigmatic wave front propagating inside a homogeneous medium, characterised by the radii of curvature ρ_1, ρ_2, as well as the principal directions of the wave front $\hat{X}_1, \hat{X}_2$, as shown in Figure 2-3. The combination of these parameters can describe any wave front type; for instance, a spherical wave front features radii of curvature finite and equal to one another $(\rho_1 = \rho_2 = R)$, while a plane wave features infinite radii of curvature $(\rho_1 = \rho_2 = \infty)$. In both cases the direction of propagation $(\hat{k})$ is orthogonal to the principal directions of the wave front, i.e. $\hat{k} = \hat{X}_1 \times \hat{X}_2$.

According to the GO method, as the wave front propagates inside a homogeneous medium, the power flows along the axial ray AA', from the point P_0 to the point P [24], [21], Figure 2-3. If dA_1 and dA_2 are elemental areas surrounding the wave front at these points, due to the conservation of energy within the tube: $\left|\vec{E}(P_0)\right|^2 dA_1 = \left|\vec{E}(P)\right|^2 dA_2$. As a result, the amplitude spreading of the electric field is expressed as in Eq. 2.7.

$$\left|\vec{E}(P)\right| = \sqrt{\frac{\rho_1\rho_2}{(\rho_1+s)(\rho_2+s)}} \left|\vec{E}(P_0)\right|, \tag{2.7}$$

where ρ_1, ρ_2 are the radii of curvature of the wave front, $s = |P_0P|$ is the distance covered by the axial ray (Figure 2-3) and $\frac{dA_1}{dA_2} = \sqrt{\frac{\rho_1\rho_2}{(\rho_1+s)(\rho_2+s)}}$. As for the phase of the propagating field, it progresses from the point P_0 to the point P by e^{-jks}, where k the propagation constant of the medium. So, the field at the point P, after propagation of the wave inside a homogeneous medium by a distance s, is given as in Eq. 2.8.

$$\vec{E}(P) = \vec{E}(P_0)\sqrt{\frac{\rho_1\rho_2}{(\rho_1+s)(\rho_2+s)}} \cdot e^{-jks}, \tag{2.8}$$
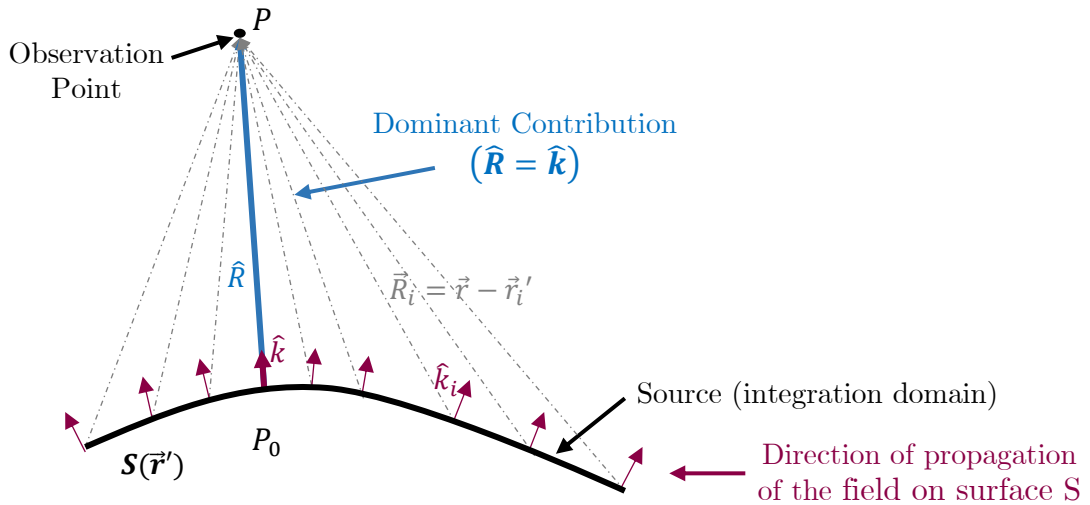
Figure 2-2. In Geometrical Optics approximation, the field on an observation point P is dominated by the contribution of the point P_0 on the source S, for which the ray connecting it with the point P is parallel to the direction of propagation of the field (solid, blue coloured line).
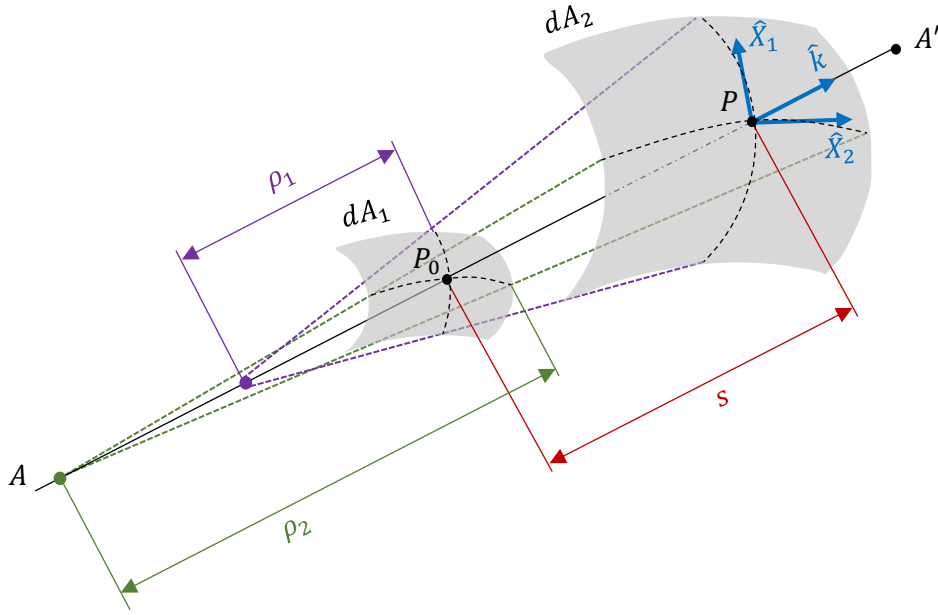
Figure 2-3. Propagation of an astigmatic wave front along an axial ray AA'. The radii of curvature of the wave front (ρ_1, ρ_2) describe the propagation of the wave in the two orthogonal planes.

Having discussed the generic methodology of calculating GO fields, let us go back to the original discussion concerning the propagation of the fields between successive surfaces of a chain of QO components. If the Geometrical Optics approximation is applicable, to calculate the field through Eq. 2.8, one needs to know the radii of curvature of the respective wave front, as well as the distance between the two surfaces. When transmitting components, such as lenses, are examined, the characteristics of the transmitted wave front $(\rho_{1,2}^t, \hat{X}_{1,2}^t)$, can be calculated as a function of the characteristics of the incident wave front $(\rho_{1,2}^i, \hat{X}_{1,2}^i)$, the surface of refraction (radii of curvature R_1, R_2 and principal unit directions $\hat{U}_1, \hat{U}_2$, Figure 2-4) and the relative permittivities of the mediums of incidence and transmission $(\varepsilon_r^i, \varepsilon_r^t)$. The analytical expressions are given in [24].

$$\rho_1^t, \rho_2^t = f\big(\varepsilon_i, \varepsilon_t, \rho_1^i, \rho_2^i, \hat{X}_1^i, \hat{X}_2^i, R_1, R_2, \hat{U}_1, \hat{U}_2\big), \tag{2.9}$$

The length of the axial ray (ray parallel to the direction of propagation, connecting the two surfaces) can be calculated using ray tracing techniques, analytically discussed in Appendix C.
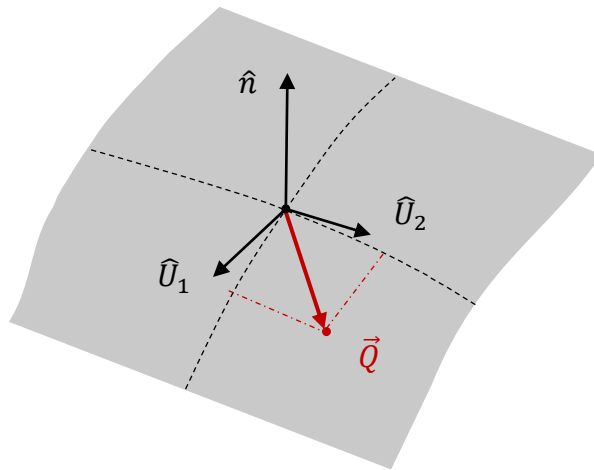
Figure 2-4. Local representation of a point $\vec{Q}$ on a surface S, which is described through its principal unit directions $\hat{U}_1, \hat{U}_2$, as well as its principal radii of curvature R_1, R_2.

As already discussed, the Geometrical Optics approximation is applied in cases where both components are electrically large and are far from caustic points. When one of the components is instead positioned near a caustic point, the rays are converging in the vicinity of the surface and thus the argument of having a dominant ray determining the field value is not accurate. In this case, diffraction effects become relevant and an integration over the surface (Eq. 2.6) is required to derive the field values. Based on this difference, the coupling between sequential components is characterized as geometrical or diffractive.

To examine two indicative examples of these coupling types, let us assume a hyperbolic lens, fed by a hyper-hemispherical lens. To properly feed the hyperbolic lens, its focal point should coincide with the virtual focus of the hyper-hemispherical lens, i.e. the position from which the transmitted field seems to originate from. Since the distance between the lens surface and the virtual focus depends on the diameter of the lens (Appendix A.1 $F_v = R_{sph}(\sqrt{\varepsilon_r} + 1)$), by altering its radius, the coupling between the two components transitions from the diffractive to the geometrical region (Figure 2-5). In particular, for a small diameter, the hyper-hemispherical lens is positioned very close to the focal point of the hyperbola, entering the diffraction region. On the other hand, when the lens' diameter is comparable to that of the free-standing hyperbolic lens, the fields can be approximated using a Geometrical Optics approach.

a. Diffractive Coupling   b. Geometrical Coupling
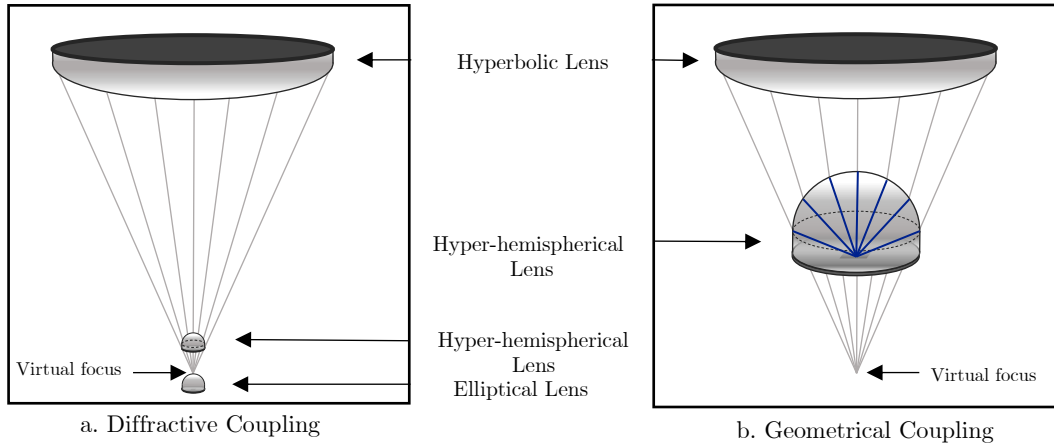
Figure 2-5. A diffractively coupled (a) and a geometrically coupled (b) system of a hyperbolic lens and a hyper-hemispherical lens. Depending on the diameter of the hyper-hemispherical lens, its surface is far or close to the caustic point, dictating the type of its coupling with the hyperbolic lens. An elliptical lens is also depicted in the diffractive coupling case, since it behaves similarly to a small hyper-hemispherical lens.

Once the two types of coupling have been discussed, in the following subsection, two techniques for analysing quasi-optical systems are mentioned. Those are the Analysis in Reception and the Coherent Fourier Optics methodologies.

2.2. Analysis Methodologies

2.2.1. Analysis in Reception

The performance of a quasi-optical system can be analysed by employing either an analysis in transmission or analysis in reception formalism [18]. In this work, the structures are analysed mainly in reception, by examining the response of the antenna systems to an incident plane wave (Eq. 2.10).

$$\vec{E}_{inc} = E_0^{pw} e_0^{-j\vec{k}_{inc}\cdot\vec{r}} \hat{p}_{pw}, \qquad (2.10)$$

where $\vec{k}_{inc} = k_0(sin\theta_{inc}cos\varphi_{inc}\hat{x} + sin\theta_{inc}sin\varphi_{inc}\hat{y} + cos\theta_{inc}\hat{z})$ is the propagation vector of the incident field, $\hat{p}_{pw}$ is the polarization of the plane wave and $\vec{r}$ is the grid on which the field is evaluated on.

To evaluate the response of an antenna to an incident plane wave, one can resort to an equivalent Thevenin circuit [18], where the field received by the antenna is represented through a voltage generator (open circuit voltage V_{oc}), the antenna as an impedance Z_a and the load connected to the antenna as Z_l. The open circuit voltage can be expressed as the reaction integral between the incident field (reception problem) and the currents induced by the antenna in transmission mode, as in Eq. 2.11. Those currents can be equivalent currents replacing any antenna system through the Surface Equivalence Theorem, discussed in section 2.1. If both the incident fields and the equivalent currents are evaluated over an arbitrary surface, the power received by the antenna can be expressed through Eq. 2.12, or for conjugate matching conditions between the antenna and the load, through Eq. 2.13.

$$V_{oc}I_{Tx} = \iint\{\vec{H}_{inc}(\theta_{inc},\varphi_{inc},\theta,\varphi) \cdot \vec{m}_{eq}(\theta,\varphi) - \vec{E}_{inc}(\theta_{inc},\varphi_{inc},\theta,\varphi) \cdot \vec{j}_{eq}(\theta,\varphi)\}dS, \quad (2.11)$$

$$P_{Rx}(\theta_{inc},\varphi_{inc}) = \frac{1}{2}|V_{oc}|^2 \frac{Re\{Z_L\}}{|Z_a+Z_L|^2}, \quad (2.12)$$

$$P_{Rx}(\theta_{inc},\varphi_{inc}) = \frac{|V_{oc}I_{Tx}|^2}{16P_{feed}}, \quad (2.13)$$

where $P_{feed} = |I_{Tx}|^2 Re\{Z_a\}/2$ is the total power radiated by the antenna feeding element in transmission mode and I_{Tx} is the current feeding the antenna.

Expressing the currents of Eq. 2.11 as equivalent currents, allows the evaluation of the reaction integral at any convenient surface throughout a quasi-optical system. For the lens chains presented in Figure 2-5, the flat surface of the plano-hyperbolic lens is chosen. Therefore, the incident field corresponds to the incident plane wave, while the equivalent currents (Eq. 2.2) are calculated through the field value radiated by the feeding element and propagated through the whole quasi-optical system, until it reaches the top surface of the plano-hyperbolic lens, forming the field distribution $\vec{E}_t(\theta,\varphi)$, $\vec{H}_t(\theta,\varphi)$, shown in Figure 2-7.

Once the power received by the antenna is estimated, the performance of the designed geometry can be evaluated through the aperture efficiency, i.e. the ratio of the received over the incident power (Eq. 2.15).

$$\eta_{ap}(\theta_{inc},\varphi_{inc}) = \frac{P_{Rx}(\theta_{inc},\varphi_{inc})}{P_{inc}}, \quad (2.15)$$

where the incident power corresponds to the power of the plane wave (Eq. 2.16), incident on an aperture with a given area A.

$$P_{inc} = \frac{|E_0^{pw}|^2}{2\zeta_0}A, \quad (2.16)$$

where for this case $A = A_{hb} = \pi\left(\frac{D_{hb}}{2}\right)^2$ is the area of the hyperbolic lens top surface.
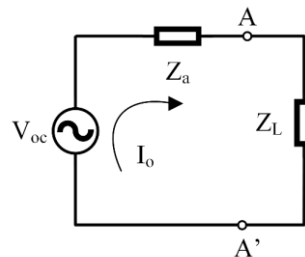
Figure 2-6. Equivalent Thevenin circuit representing an antenna in reception mode.

Equations $2.11 - 2.15$ imply that in order to maximize the aperture efficiency of the system, a field matching condition is required, i.e. the field transmitted out of the top surface of the hyperbolic lens should be conjugately matched to the incident plane wave. Therefore, the targeted phase profile created from the antenna side corresponds to a flat phase for broadside incidence and a linearly progressive phase for scanning, as shown in Figure 2-8.

To evaluate the scanning performance of a quasi-optical system, the scan loss can be utilized. This metric is defined as the ratio between the aperture efficiency corresponding to a plane wave incident from broadside (feeding element at the focus of the quasi-optical system) and the aperture efficiency corresponding to an off-broadside incidence (feeding element displaced on the focal plane), Eq. 2.17.

$$Scan\ Loss = 10\log_{10}\left(\frac{\eta_{ap}(0,0)}{\eta_{ap}(\theta_{inc},\varphi_{inc})}\right), \tag{2.17}$$

This analysis methodology is convenient for the geometry of Figure 2-5, since once the field on the upper surface of the hyperbolic lens is known, one can utilize it for the calculation of the far field pattern of the whole QO system, using an analysis in transmission technique. In particular, one can employ the Surface Equivalence Theorem to substitute the whole antenna system with a set of equivalent surface currents, radiating in free space and derive the far field of the geometry through Eq. 2.6. Alternatively, the problem can be approached in the spectral domain, where the Stationary Phase Point Approximation can be applied for the derivation of the far field.
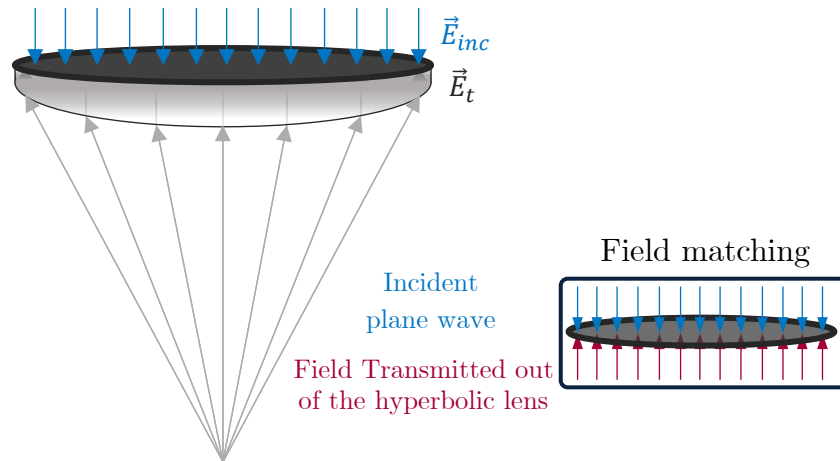
Figure 2-7. Analysis in reception methodology, applied for the case of a hyperbolic lens, fed by a generic spherical wave originating from its focal point. The field matching is examined on the top surface of the hyperbola, as shown in the inset.
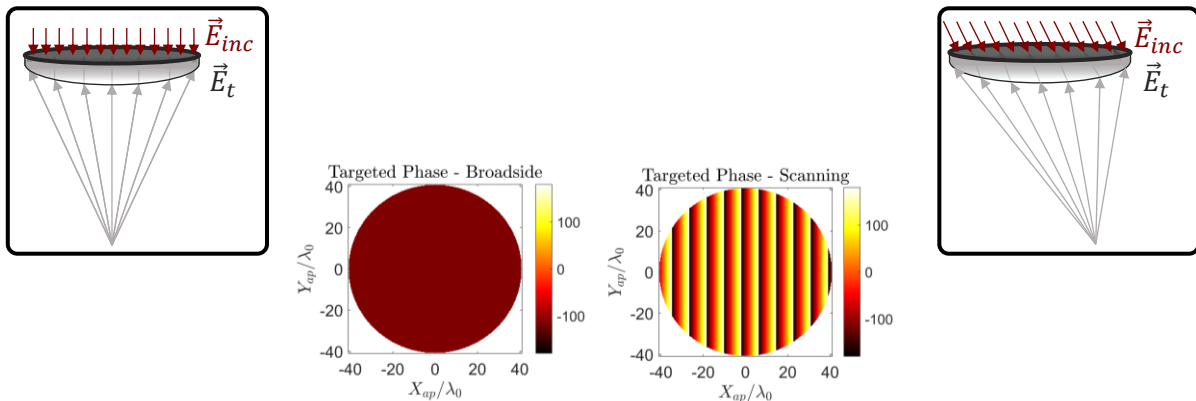
Figure 2-8. Targeted phase profile (created in transmission) on a planar surface to maximize the aperture efficiency, in a plane wave incidence scenario.

The technique described in this section can be applied for any feeding element. However, when the Geometrical Optics Approximation is applicable, this methodology is very time efficient, since the field transmitted on the top of the hyperbolic lens can be derived by cascading GO propagation between successive surfaces, without the need of any integration. However, when the source of the quasi-optical system is positioned close to a caustic point, a Physical Optics approach needs to be adopted for the calculation of the field and thus a double spatial integration is required for every observation point, which is a very time consuming step. To avoid this, the modelling of such QO systems (e.g. lens-based focal plane arrays) can be performed using a Coherent Fourier Optics technique, described in detail in [19] and summarized in the following subsection (2.2.2).

2.2.2. Coherent Fourier Optics

With the Coherent Fourier Optics methodology, the focal field of the primary quasi-optical component (such as the hyperbolic lens of Figure 2-5a), can be derived as a Plane Wave Spectrum (PWS) in reception. Subsequently, the performance of the system can be evaluated using an analysis in reception similar to that described in section 2.2.1, but with the reaction integral directly evaluated on the surface of the small focal lens. This methodology enables the derivation of the optimal radiation pattern of the source, by applying a conjugate field match condition.

Based on the analysis performed in [19], using an auxiliary sphere, referred to as FO sphere (Figure 2-9), the CFO Plane Wave Spectrum around the focal point is expressed as in Eq. 2.18.

$$\vec{E}_{CFO}(\vec{k}_\rho) \cong e^{-\frac{jk|\vec{\rho}_{CFO}|^2}{2R_{FO}}} \vec{E}_{FO}(\vec{k}_{CFO} - \vec{k}_\rho)e^{j(\vec{k}_{CFO} - \vec{k}_\rho)\cdot\vec{\rho}_{CFO}}, \tag{2.18}$$

where $\vec{k}_{CFO} = (k/R_{FO})\vec{\rho}_{CFO}$, with R_{Fo} being the radius of the FO sphere and $\vec{\rho}_{CFO}$ the lateral displacement of the examined source position, in relation to the FO sphere's centre, as shown in Figure 2-9. $\vec{E}_{FO}$ is the PWS of the direct field, as given in Eq. 2.19.

$$\vec{E}_{FO}(\vec{k}_\rho) = \frac{j2\pi R_{FO}e^{-jkR_{FO}}}{\sqrt{k^2 - k_\rho^2}} \hat{R} \times [\vec{E}_{GO}(\vec{R}) \times \hat{R}], \tag{2.19}$$

where $\hat{R} = \hat{k}_\rho + \sqrt{1 - (k_\rho^2/k^2)}\hat{z}$, $\vec{k}_\rho = k\sin\theta\hat{\rho}$ corresponding to the direction of propagation of the examined plane wave, and $\hat{R} \times [\vec{E}_{GO}(\vec{R}) \times \hat{R}]$ is the GO field component tangent to the equivalent FO sphere. The GO field can be calculated using a GO propagation between the primary quasi-optical component (hyperbolic lens in this case) and the FO sphere.

To evaluate the performance of a QO system, comprised of a primary focusing component (e.g. a hyperbolic lens or a parabolic reflector), diffractively coupled to a lens (e.g. elliptical lens), the plane wave spectrum calculated through Eq. 2.18, should be coherently summed on top of the lens surface, as in Eq. 2.20.

$$\vec{E}_l^{Rx}(\vec{r}_l) = \iint \vec{E}_{CFO}(\vec{k}_\rho)e^{j\vec{k}_\rho\cdot\vec{Q}_l}k_\rho dk_\rho d\alpha, \tag{2.20}$$

where $\vec{Q}_l$ indicates the positions on the lens surface. It is noted that this methodology is much faster than the PO technique, since in the PO, to calculate the field on an observation grid, a double integration is required for each observation point, while in the CFO, only one double integral needs to be calculated.

To perform the reaction integral on top of the lens surface, the field transmitted by the feeding antenna, should also be calculated, as in Eq. 2.21.

$$\vec{E}_l^{Tx}(\vec{r}_l) = \bar{\bar{\tau}} \cdot \vec{E}_{feed}(\theta, \varphi) \frac{e^{-jk_l r_l(\theta)}}{r_l(\theta)}, \tag{2.21}$$

where $\vec{E}_{feed}(\theta, \varphi)$ is the pattern of the feeding element, $k_l = k_0\sqrt{\varepsilon_r^l}$ is the propagation constant inside the lens material, $r_l(\theta)$ is the radial distance between the phase centre of the feeding element and the surface of the lens and $\bar{\bar{\tau}}$ is the transmission dyad. It is noted that if the lateral displacement of the lens is large, an off-focus FO sphere can be utilized instead to accurately represent the focal field. In this case $\vec{\rho}_{CFO} = \vec{\rho}_{lens} - \vec{\rho}_{FO}$.
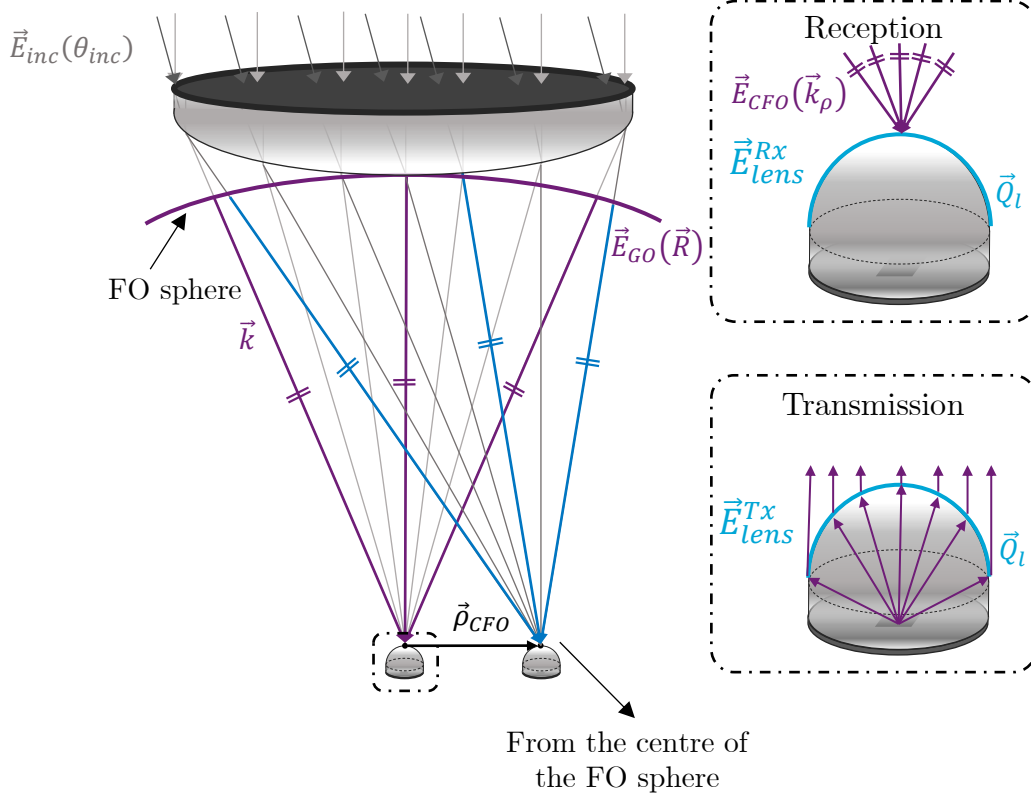
Figure 2-9. Coherent Fourier Optics technique representation. The focal field is expressed as a summation of plane waves around the small focal lens region.

Once the theoretical basis for analysing lens chain architectures has been discussed in Chapter 2, two specific types of lens chains will be discussed in the following chapters, as potential solutions for the suggested building blocks of the TIFUUN antenna system. In particular, in Chapter 3 a geometrically coupled system of a hyper-hemispherical and a hyperbolic lens will be discussed, while in Chapter 4, a diffractively coupled solution will be explored, comprised of a hyperbolic lens and a focal plane array of either small hyper-hemispherical, or elliptical lenses. In both cases, the performance will be explored both as a single pixel solution, as well as in an array configuration.

Chapter 3.
Geometrically Coupled Lens Chain

Hyperbolic Lens coupled to a Hyper-hemispherical Lens

3.1. Analysis Methodology

The first geometry examined is shown in Figure 2-5b, and deals with a multi-surface propagation scenario, where an electrically large hyper-hemispherical lens is geometrically coupled to a hyperbolic lens. The procedure followed to analyse such a system is based on the analysis techniques discussed in Chapter 2, i.e. transmission through locally flat surfaces and propagation between surfaces, using the Geometrical Optics approximation. The steps for the analysis are summarized below and in Figure 3-1.

1. Calculate the field incident on the inner surface of the hyper-hemispherical lens $\left(\vec{E}_1^i\right)$.
2. Transmit the field to the outer surface of the hyper-hemispherical lens $\left(\vec{E}_2^t\right)$.
3. Propagate the field from the outer surface of the hyper-hemispherical lens, to the bottom outer surface of the hyperbolic lens $\left(\vec{E}_2^i\right)$, using GO propagation.
4. Transmit the field to the lower inner surface of the hyperbolic lens $\left(\vec{E}_3^t\right)$.
5. Propagate the field from the bottom inner surface to the top inner surface of the hyperbolic lens $\left(\vec{E}_3^i\right)$, using GO propagation.
6. Transmit the field to the upper outer surface of the hyperbolic lens $\left(\vec{E}_4^t\right)$.
7. Calculate the equivalent currents on the top outer surface of the hyperbolic lens.
8. Using analysis in transmission, calculate the far field radiated by this geometry.
9. Using analysis in reception, calculate the aperture efficiency.

To apply the process described above, the first step is to define the properties of the wave front radiated by the feed. Assuming that the hyper-hemispherical lens surface is in the far field of the feeding antenna, the radiated wave front is represented by a spherical wave originating from the phase centre of the antenna, Figure 3-2. Thus, the radii of curvature are equal to one another and equal to the radial distance between the lens surface and the phase centre of the antenna $(\rho_{1,2}^i = r(\theta))$, while the field incident on the lens is given in Eq. 3.1.
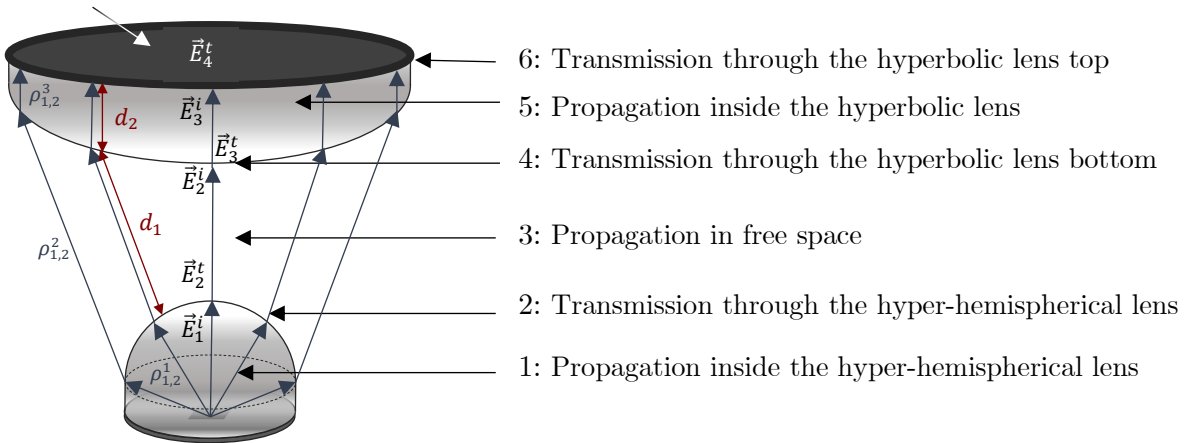
Figure 3-1. Candidate Geometry I: Hyper-hemispherical Lens, Geometrically Coupled to Hyperbolic Lens.
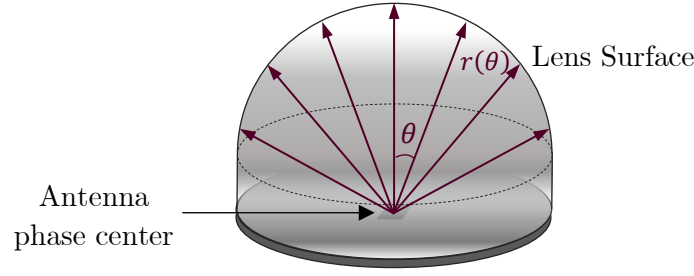
Figure 3-2. Hyper-hemispherical lens geometry.

$$\vec{E}_1^i = \vec{E}_{feed}^{FF}(\theta, \varphi) \cdot \frac{e^{-jk_1 \cdot r(\theta)}}{r(\theta)}, \tag{3.1}$$

where $\vec{E}_{feed}^{FF}(\theta, \varphi)$ is the radiation pattern of the feed, $k_1 = k_0 \sqrt{\varepsilon_r^{hh}}$ is the propagation constant inside the hyper-hemispherical lens material, with permittivity ε_r^{hh}, and $r(\theta)$ is the radial distance from the antenna phase centre to the lens surface.

Subsequently, the field transmitted from the lens surface is calculated as the product of the incident field and the transmission dyad, as in Eq. 3.2.

$$\vec{E}_2^t = \bar{\bar{\tau}}_1 \cdot \vec{E}_1^i \tag{3.2}$$

The transmission dyad can be calculated as explained in Appendix B.

The next step involves the propagation through the homogeneous medium between the two lenses, described by Eq. 3.3.

$$\vec{E}_2^i = \vec{E}_2^t \sqrt{\frac{\rho_1^2 \rho_2^2}{(\rho_1^2 + d_1)(\rho_2^2 + d_1)}} \cdot e^{-jk_2 d_1}, \tag{3.3}$$

where $k_2 = k_0$ for propagation in free space, $d_1 = \left| \overrightarrow{Q_{hh} Q_{hb}^{bot}} \right|$ is the distance between the two lens surfaces, calculated using ray tracing, as discussed in Appendix C and $\rho_{1,2}^2$ are the radii of curvature of the wave front transmitted from the hyper-hemispherical lens, which can be calculated as a function of the properties of the incident wave front, the curvature of the surface of incidence and the permittivity of the hyper-hemispherical lens.

Steps 4-6 are similar to steps 2 and 3, i.e. they involve the transmission through the bottom and top surfaces of the hyperbolic lens, as well as the propagation inside the lens (homogeneous medium). The field expressions are given in Eq. 3.4-3.6.

$$\vec{E}_3^t = \bar{\bar{\tau}}_2 \cdot \vec{E}_2^i \tag{3.4}$$

$$\vec{E}_3^i = \vec{E}_3^t \sqrt{\frac{\rho_1^3 \rho_2^3}{(\rho_1^3 + d_2)(\rho_2^3 + d_2)}} \cdot e^{-jk_3 d_2}, \tag{3.5}$$

$$\vec{E}_4^t = \bar{\bar{\tau}}_3 \cdot \vec{E}_3^i \tag{3.6}$$

where $\bar{\bar{\tau}}_2$ is the transmission dyad corresponding to transmission through the lower surface of the hyperbolic lens and $k_3 = k_0 \sqrt{\varepsilon_r^{hb}}$ is the propagation constant inside the hyperbolic lens' dielectric. Furthermore, $\rho_{1,2}^3$ are the radii of curvature of the wave front propagating inside the hyperbolic lens (calculated as a function of the properties of the incident wave front, the curvature of the surface of incidence and the material properties) and $d_2 = \left| \overrightarrow{Q_{hb}^{bot} Q_{hb}^{top}} \right|$ is the distance between the bottom and top surfaces of the hyperbola (calculated using ray tracing,

Appendix C). Finally, $\bar{\bar{\tau}}_3$ is the transmission dyad corresponding to transmission through the upper surface of the hyperbola.

Once the field on the upper surface of the hyperbolic lens is known, one can employ the analysis methodology described in Section 2.2 to evaluate the aperture efficiency of the system (Eq. 2.15), as well as to derive the far field pattern of the whole geometry (Eq. 2.6).

The above described methodology is also applicable for a scanning scenario, i.e. a feeding element laterally displaced inside the hyper-hemispherical lens. Thus, a focal plane array of feeding elements under the hyper-hemispherical lens can be analysed following the same steps and adjusted parameters.

3.2. Design Guidelines

When a hyper-hemispherical lens is geometrically coupled to a primary focusing component (Figure 3-3), its geometry poses an inherent limitation on the f-number of the primary quasi-optical component. This limit comes from the angular region for which a spherical wave is transmitted through the hyper-hemispherical lens. In particular, above a certain subtended angle, part of the primary focusing component is left unilluminated, reducing the taper efficiency of the system. To avoid this, a maximum subtended angle equal to θ_v (angle between the virtual focus and the edge of the hyper-hemispherical lens) can be defined, as given in Eq. 3.7 and shown in Figure 3-3.

$$\theta_v = \tan^{-1}\left(\frac{D_{hh}}{2\left(F_v^{hh} - R_{sph}^{hh} + h_{hh}\right)}\right), \tag{3.7}$$

where D_{hh} is the diameter of the hyper-hemispherical lens, R_{sph}^{hh} is the radius of the hemispherical part of the lens, $F_v^{hh} = R_{sph}^{hh}\left(\sqrt{\varepsilon_r^{hh}} + 1\right)$ is the vertical distance between the virtual focus and the tip of the lens and h_{hh} is the vertical distance between the center of the hemisphere and the edge of the truncated lens, as shown in Figure 3-3. A more detailed discussion on the geometry of the hyper-hemispherical lens is given Appendix A.1.

For a **reflector** as the primary focusing component, the relation between its $f_\#$ and the subtended angle (θ_0) is given in Eq. 3.8.

$$\theta_0 = 2\tan^{-1}\left(\frac{1}{4f_\#}\right), \tag{3.8}$$

So, the minimum $f_\#$, i.e. when $\theta_v = \theta_0$, is analytically calculated as in Eq. 3.9.

$$f_\#^{min} = \left\{4\tan\left(0.5 \cdot \tan^{-1}\left(\frac{D_{hh}}{2(F_v - R_{sph} + h)}\right)\right)\right\}^{-1}, \tag{3.9}$$

For a **hyperbolic lens**, the relation between the $f_\#$ and the subtended angle is not as straightforward as in the reflector case, since it also depends on the material of the lens (Eq. 3.10).

$$\theta_0 = \tan^{-1}\left(\sqrt{\varepsilon_r} + 1 \cdot \left\{2f_\# \cdot \left(\sqrt{1 + \frac{1}{4f_\#^2 \cdot \frac{\varepsilon_r - 1}{(\sqrt{\varepsilon_r} + 1)^2}}} + \sqrt{\varepsilon_r}\right)\right\}^{-1}\right), \tag{3.10}$$

Hence, a curve can be utilized instead of an analytical expression to calculate the minimum acceptable $f_\#$, for an angle θ_v of the hyper-hemispherical lens (Eq. 3.7). For three commonly utilized dielectric materials, this curve is given in Figure 3-4.

(a) Hyper-hemispherical Lens fed by Reflector   (a) Hyper-hemispherical Lens fed by Hyperbolic Lens
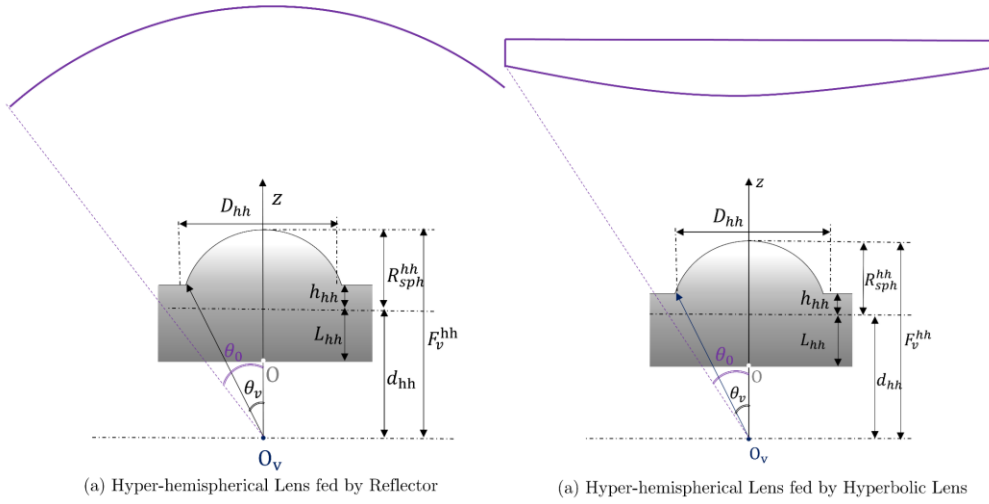
Figure 3-3. Hyper – Hemispherical Lens Geometrically Coupled to: (a) Reflector, (b) Hyperbolic Lens
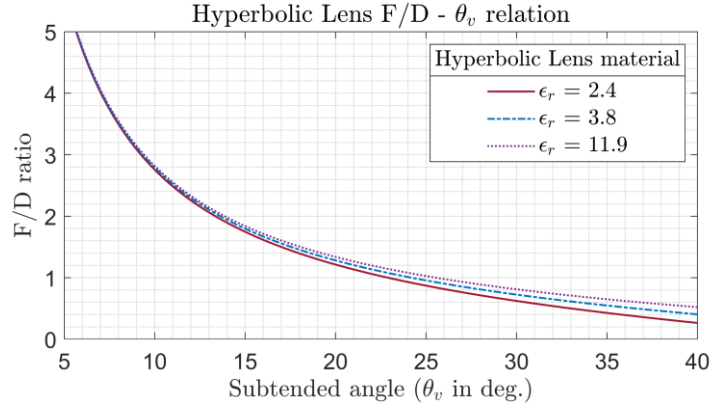
Figure 3-4. Relation between the focal distance to diameter ratio and the subtended angle of hyperbolic lenses made of commonly used dielectrics, $\varepsilon_r = 2.4$ (TOPAS), $\varepsilon_r = 3.8$ (fused silica), $\varepsilon_r = 11.9$ (silicon).

3.3. Scanning Capabilities and Limitations

When an array of feeding elements is placed under a hyper-hemispherical lens, which is geometrically coupled to a hyperbolic lens, the field incident on the geometry experiences multiple refractions until it reaches the focal plane of the lens. By studying this system geometrically, one can estimate the optimal position of a feeding element, such that the power received by its load is maximized for a plane wave incident with an angle θ_{inc}. The first step towards this goal is to determine the relation between the displacement of the feeding element inside the hyper-hemispherical lens $\left(\rho_{feed}\right)$ to the position of a virtual source $\left(\rho_v\right)$ on the focal plane of the hyperbola, as shown in Figure 3-5. Then, by examining the hyperbolic lens in reception (Figure 3-6), one can define the relation between the incident angle and the virtual focus position. It is noted that the ray picture in the inset of Figure 3-5 is performed by backward ray tracing of the transmitted field.

Assuming a small horizontal displacement of the feed, the vertical displacement of the virtual source can be considered negligible and thus the distance from the tip of the lens can be approximated through the virtual focus distance F_v, i.e. $z_v \cong F_v$. Following the central (dominant) ray, shown in Figure 3-5, the angles of incidence and transmission through the hyper-hemispherical lens, θ_{in} and θ_{out} are:

$$\theta_{in} = \tan^{-1}\left(\frac{\rho_{feed}}{R_{sph}^{hh} + L_{hh}}\right), \quad \theta_{out} = \tan^{-1}\left(\frac{\rho_v}{F_v^{hh}}\right)$$

By employing Snell's Law, the relation between ρ_{feed} and ρ_v can be calculated through Eq. 3.11, assuming small angles of incidence and transmission and thus $sin\theta_{in} \cong tan\theta_{in} = \frac{\rho_{feed}}{R_{sph}^{hh}+L_{hh}}$ and $\sin\theta_{out} \cong \tan\theta_{out} = \frac{\rho_v}{F_v^{hh}}$.

$$n_1 sin\theta_{in} = n_2 \sin\theta_{out} \xrightarrow{\begin{subarray}{c} L = R_{sph}^{hh}/\sqrt{\varepsilon_r^{hh}} \\ F_v^{hh} = R_{sph}^{hh}\left(1+\sqrt{\varepsilon_r^{hh}}\right) \end{subarray}} \sqrt{\varepsilon_r^{hh}} \cdot \frac{\rho_{feed}}{\frac{R_{sph}^{hh}}{\sqrt{\varepsilon_r^{hh}}}\left(1+\sqrt{\varepsilon_r^{hh}}\right)} = \frac{\rho_v}{R_{sph}^{hh}\left(1+\sqrt{\varepsilon_r^{hh}}\right)} \Rightarrow$$

$$\rho_v = \varepsilon_r^{hh} \cdot \rho_{feed}, \tag{3.11}$$

To maximize the power delivered to a load from an incident angle $\theta_{inc} = N\lambda_0/D_{hb}$ (N-beams scanning), the virtual focus of the hyper-hemispherical lens should ideally coincide with the flashpoint of the hyperbolic lens. An initial estimation of the flashpoint position can be made geometrically for small incident angles, by applying the Snell's Law on the dominant ray passing though the hyperbola, shown in Figure 3-6.

$$\begin{cases} n_1 \sin(\theta_{inc}) = n_2 \sin(\theta_{t2}) = n_3 \sin(\theta_{t3}) \\ \rho_v = F_{hb} tan\theta_{t3} \end{cases} \xrightarrow{sin\theta_{t3} \cong tan\theta_{t3} = \frac{\rho_v}{F_{hb}}}$$

$$\rho_v \cong N\lambda_0 \frac{F_{hb}}{D_{hb}}, \tag{3.12}$$

Although this is a good first estimation of the flashpoint position, as it can be observed from the ray picture of the inset of Figure 3-6, for larger angles of incidence, the convergence of rays into a single position is less clear, degrading the scanning performance. Overall, Eq. 3.11 and 3.12 feature certain approximations, which are more accurate for large f-numbers and small angles of incidence.
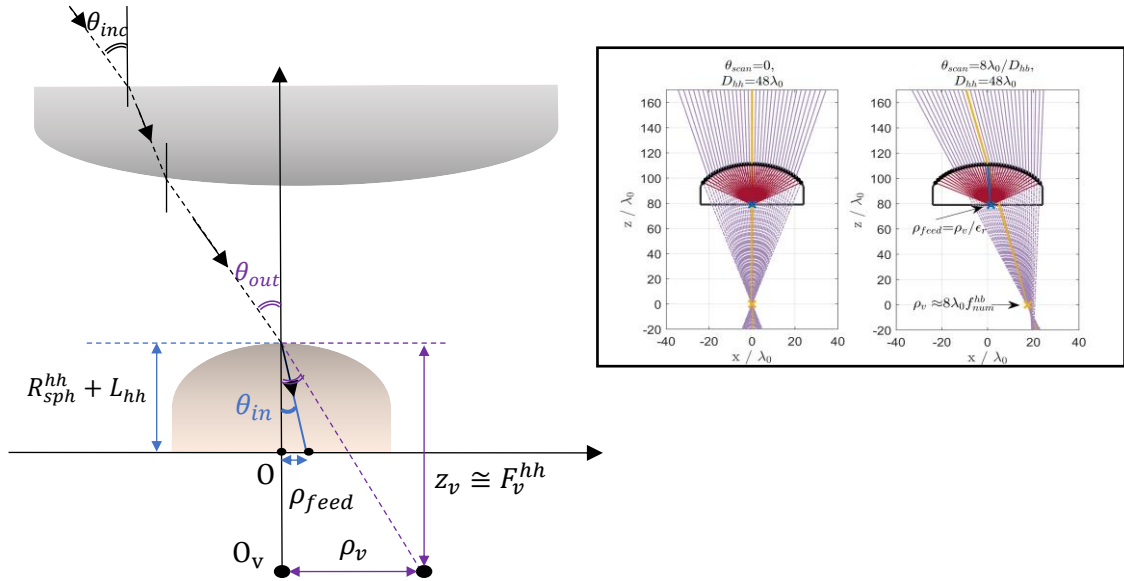
Figure 3-5. Relation between the feed displacement inside a hyper-hemispherical lens and the displacement of its virtual focus. The inset shows an indicative ray tracing example (backward ray tracing of the transmitted field) for broadside and scanning to $\theta_{scan} = 8\frac{\lambda_0}{D_{hb}}$.
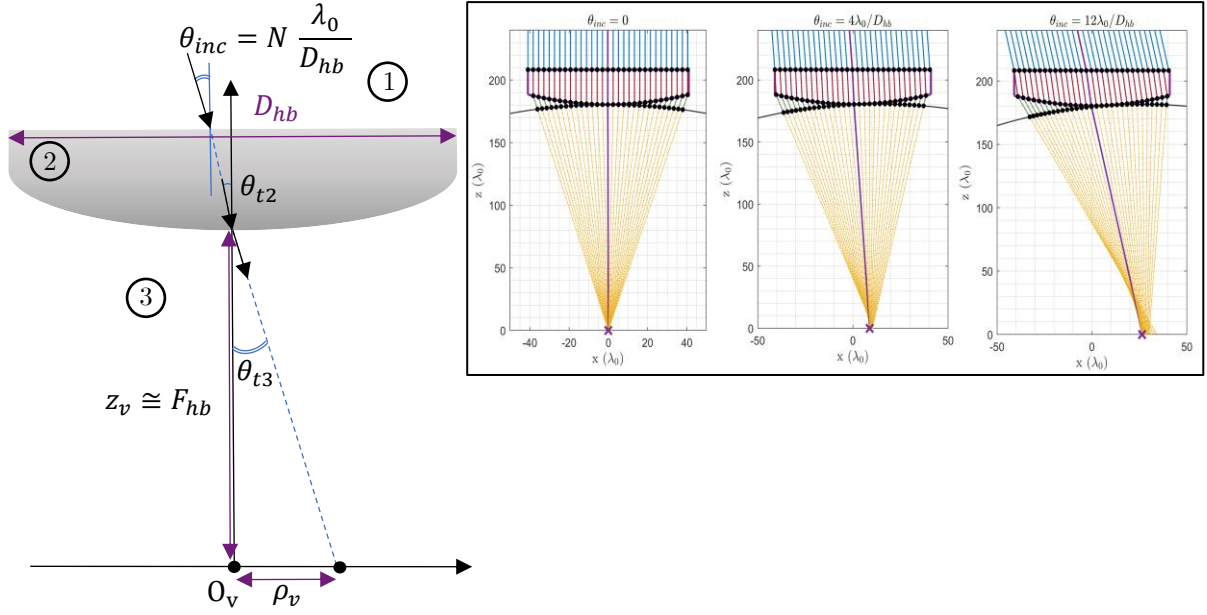
Figure 3-6. Flashpoint estimation for hyperbolic lenses. The ray picture shown in the inset corresponds to focal distance to diameter ratio of $\frac{F_{hb}}{D_{hb}} = 2.2$, diameter of the hyperbolic lens $D_{hb} = 82\lambda_0$ and $\theta_{inc} = 0, \theta_{inc} = 4\frac{\lambda_0}{D_{hb}}$ and $\theta_{inc} = 12\frac{\lambda_0}{D_{hb}}$ respectively.

An immediate consequence of the relation between the position of the virtual source and the position of the actual feeding element is the maximum acceptable dimensions of adjacent feeds in an array configuration. In particular, as indicated in Eq. 3.11 and Figure 3-5, the displacement of a feeding element inside the hyper-hemispherical lens $\left(\rho_{feed}\right)$, is smaller than that of a virtual source placed on the focal plane of the primary focusing component $\left(\rho_v\right)$. As a result, to be able to scan at small angles, adjacent feeds inside the hyper-hemispherical lens must be placed closer to one another, compared to feeding elements directly placed at the focal plane of the primary quasi-optical component. To achieve this, the physical size of the feeding elements should be reduced, potentially affecting the illumination efficiency of the hyper-hemispherical lens, due to insufficient directivity of the feed. To avoid the latter, one can utilize feeding elements large enough to increase the illumination efficiency and under-sample the image plane. It is noted that the above described phenomenon is more dominant when high permittivity materials are utilized for the hyper-hemispherical lens design, since from Eq. 3.11, the feed displacement is equal to the virtual source displacement divided by the permittivity of the lens $\left(\rho_{feed} \cong \frac{\rho_v}{\varepsilon_r^{hh}}\right)$.

Another unique feature of utilizing two focusing components in the same configuration, is that their focal planes do not coincide. In particular, even though the geometry is designed such that the focal point of the two components is shared, due to the different surface curvatures, their focal planes feature different shapes. This causes an additional scan loss, when the feed is displaced from the focus of the hyper-hemispherical lens, especially for small radii of the hyper-hemispherical lens, as shown in Figure 3-7. The reason for that is that as the hyper-hemispherical lens diameter increases, the focal plane of the hyper-hemispherical lens approaches the one of the hyperbolic lens. To showcase this behaviour, the ray tracing picture is shown in Figure 3-8 for three different diameters of the hyper-hemispherical lens, where it is clear that for smaller diameters of the hyper-hemispherical lens, the spill-over efficiency as well as the taper efficiency of the quasi-optical system decreases significantly, due to improper illumination of the hyperbolic lens.
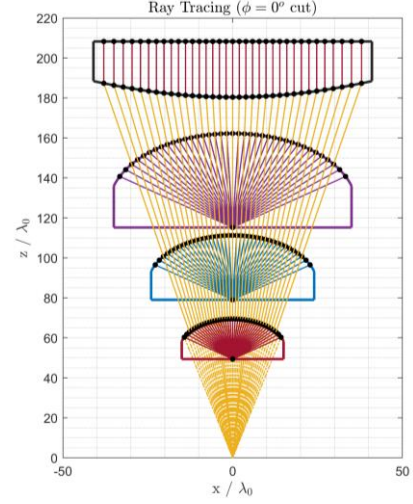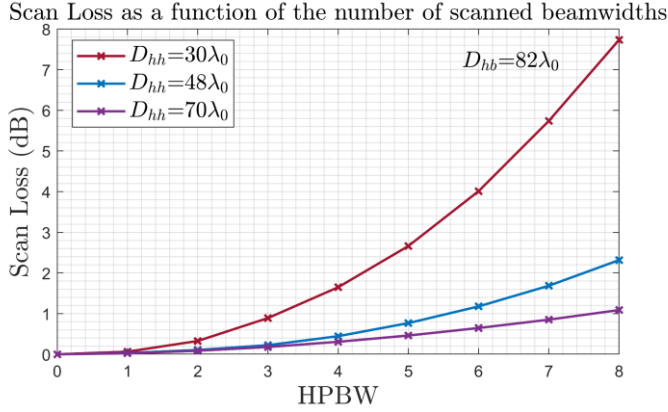
Figure 3-7. Impact of the variation of the hyper-hemispherical lens radius in the scanning performance of a geometrically coupled system of a hyper-hemispherical and a hyperbolic lens ($F_{hb}/D_{hb} = 2.2$). The scanning performance is improved, as the radius of the hyper-hemispherical lens is increased.
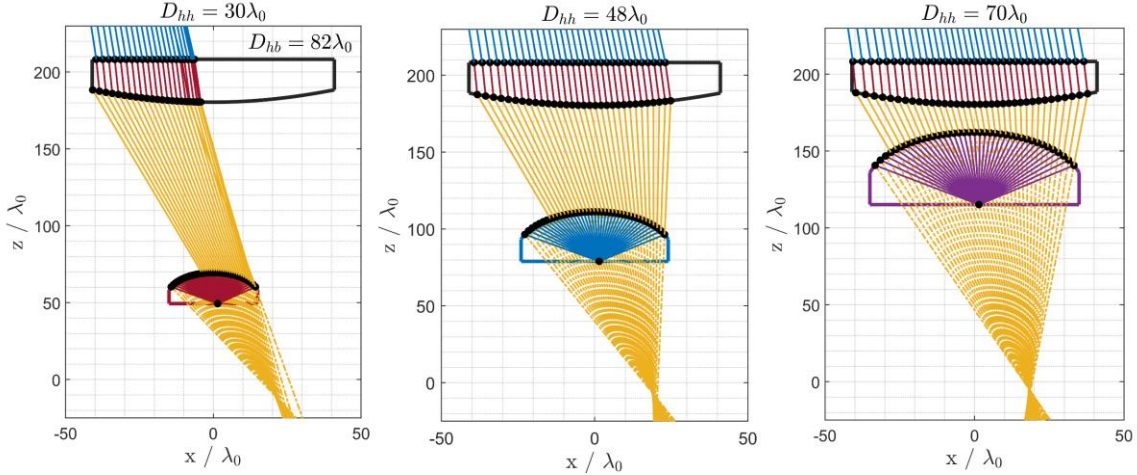
Figure 3-8. Ray Tracing of a geometrically coupled system of a hyper-hemispherical and a hyperbolic lens ($F_{hb}/D_{hb} = 2.2$), in scanning configuration, for three different diameters of the hyper-hemispherical lens. The scanning angle for all cases is $\theta_{scan} \cong 8\lambda_0/D_{hb}$, while the diameter of the hyperbola is $D_{hb} = 82\lambda_0$.

3.4. Figures of Merit

Following the guidelines given in section 3.2, one can design a quasi-optical system comprised of a focal plane array of feeding elements, under a hyper-hemispherical lens, geometrically coupled to a hyperbolic lens. To facilitate the design process, the total aperture efficiency of the system is decomposed into a number of efficiency terms. In this case the decomposition is as follows:

- **Illumination efficiency of the hyper-hemispherical lens $\boldsymbol{\eta_{hh}}$**, i.e. reflections and spill-over in the hyper-hemispherical lens (Eq. 3.14).

$$\eta_{hh} = \eta_{ref}^{hh} \cdot \eta_{so}^{hh} = \frac{P_2^t}{P_{feed}}, \tag{3.14}$$

where P_2^t is the power transmitted out of the hyper-hemispherical lens, related to the field distribution $\vec{E}_2^t$ of Figure 3-1 and P_{feed} the power radiated by the feeding element.

- **Efficiency terms related to the hyperbolic lens $\boldsymbol{\eta_{hb}}$**, i.e. reflections and spill-over, both in the top and in the bottom surface of the hyperbola (Eq. 3.15).

$$\eta_{hb} = \eta_{ref}^{\text{hb}} \cdot \eta_{so}^{hb} = \frac{P_4^t}{P_2^t}, \tag{3.15}$$

where P_4^t is the power at the top surface of the hyperbolic lens, related to the field distribution $\vec{E}_4^t$ of Figure 3-1.

- **Field matching efficiency $\boldsymbol{\eta_{FM}}$.** For the analysis described in section 2.2.1, the field matching efficiency is the equivalent of the taper efficiency, since the reaction integral is performed directly on the radiating aperture (top of the hyperbola). Thus, it describes the decrease in directivity due to its inefficient illumination of this aperture.

$$\eta_{FM} = \frac{|V_{oc}I_{Tx}|^2}{16P_4^t P_{inc}}, \tag{3.16}$$

where P_{inc} is the power of the incident plane wave, V_{oc} is the open-circuit voltage and I_{Tx} is the current feeding the antenna (Eq. 2.11, 2.16).

- **Cross-polarization efficiency $\boldsymbol{\eta_{cx}}$**, i.e. the power related to the co-pol component of the feeding element $\left(P_{feed}^{co}\right)$ divided by the total power radiated by the feed.

$$\eta_{cx} = \frac{P_{feed}^{co}}{P_{feed}}, \tag{3.17}$$

It is noted that the cross-pol efficiency is also included in the field matching efficiency, via the scalar product between the incident and transmitted fields (Eq. 2.11). Thus, the aperture efficiency is given as the product of the first three terms, as in Eq. 3.18. Furthermore, to minimize the reflections, matching layers can be introduced in each lens surface (hyper-hemispherical lens top, hyperbolic lens bottom and hyperbolic lens top).

$$\eta_{ap} = \eta_{hh} \cdot \eta_{hb} \cdot \eta_{fm}, \tag{3.18}$$

As for the scanning performance of the geometry, it can be evaluated through the scan loss, i.e. the ratio between the aperture efficiency of a displaced element and that of the central element, as given in Eq. 2.17.

3.5. Preliminary Design, based on a Gaussian-shaped Feeding Element

Having defined the methodology to analyse the geometry of Figure 3-1, one can proceed to the design of such a QO system. This process is divided into two stages. In the first stage, which is described in the current section (3.5), a y-polarized Gaussian feeder is considered as the feeding element, while in the following section (3.6), a real feeding element, i.e. a tapered leaky wave slot, is introduced. Performing the analysis with the Gaussian feeder in a first stage allows us to focus on the response of the quasi − optical system, without considering any frequency-dependent phenomena coming from the antenna. Subsequently, having studied the performance of the Gaussian-fed architecture, one can design the leaky wave feed to either enhance any desired behaviours, or partly counteract any undesired ones. The expression of the far field pattern of a y-polarized Gaussian feeder is given in Eq. 3.13 and an indicative example of such a feeding element's far field, with -11dB field taper at 45º is shown in Figure 3-9.

Gaussian Feed Far Field, Y-component
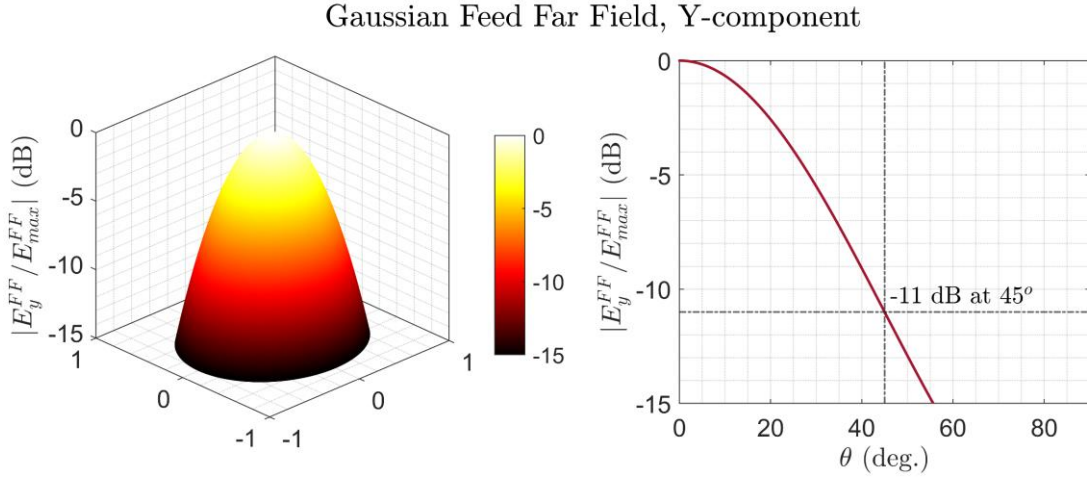
Figure 3-9. Ideal feeding element, with a Gaussian-shaped far field, -11dB field taper at 45°.

$$\vec{E}_{Gaussian} = E_0 \cdot e^{-\left\{\left[\frac{u}{u_0}\right]^2 + \left[\frac{v}{v_0}\right]^2\right\}} \cdot \left(sin\varphi \cdot \hat{\theta} + cos\varphi \cdot \hat{\varphi}\right), \tag{3.13}$$

where u_0, v_0 are the Gaussian feeder parameters, determining the directivity of the pattern, E_0 is the amplitude of the electric field and $u = sin\theta cos\varphi$, $v = sin\theta sin\varphi$ correspond to the UV coordinates.

Except for the frequency independent behaviour, the Gaussian feeder features some more characteristics that cannot represent the actual performance of a leaky-wave feed, resulting to an overestimation of the performance, compared to the final design. Those are, rotationally symmetric pattern, lack of side-lobes and lack of cross-polarization.

3.5.1. Design & Performance

The parameters of the hyper-hemispherical lens utilized in this preliminary design phase, together with the Gaussian far field tapering, are given in Table 1. The tapering of the far field of the feeding element indicates the normalized field value at a certain angle and is chosen to maximize the illumination efficiency of the lens (Eq. 3.14), as well as the aperture efficiency of the primary component, through determining the spill-over, as well as the edge taper of the field distribution on the radiating aperture.

For the lens of Table 1 (for which $\theta_v = 14.4°$), the minimum f-number for a hyperbolic lens of permittivity 2.4 is equal to 1.8 (calculated through Figure 3-4 of the analysis presented in section 3.2). Since this work focuses on the design of a focal plane array under the hyper-hemispherical lens, the optimal f-number does not only depend on the aperture efficiency of the central element, but also on the scanning performance of the structure. After a parametric analysis, shown in Figure 3-10, the optimal f-number of the hyperbolic lens is chosen equal to 2.1. The f-number choice is made taking into account that f-numbers above 1.8 lead to a good broadside performance, while to optimize the scanning, a slightly larger value is required. All parameters of the hyperbolic lens are given in Table 1, the geometry is shown in Figure 3-11 and the radiation patterns for three frequencies in a bandwidth of 1:2 are presented in Figure 3-12. The definition of the geometrical characteristics of both lenses are given in Appendix A (A.1 and A.2).

Regarding the scanning with this geometry, it should be noted that adjacent feeding elements at a distance of ρ_{feed}, create neighbouring beams in the image plane with an angular distance equal to $\Delta\theta \cong \varepsilon_r^{hh}\rho_{feed}/F_{hb}$, meaning that the sampling condition is determined by the physical dimensions of the feed. Since the Gaussian feed is an ideal model, this aspect will be further discussed when the real antenna is introduced, in section 3.6.
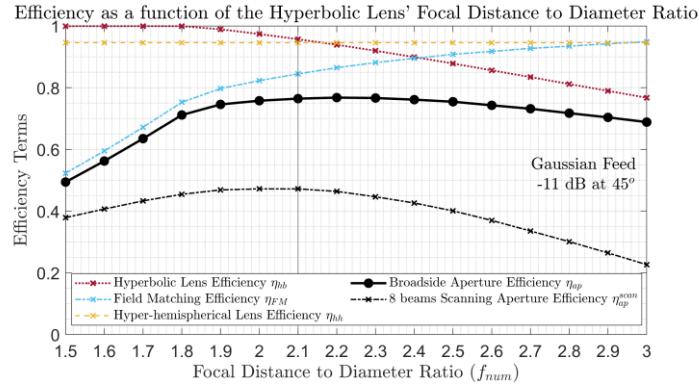
Figure 3-10. Efficiency Terms as a function of the Focal Distance to Diameter ratio $\left(f_{\#}^{hb}\right)$ of the hyperbolic lens. Both the aperture efficiency at broadside, as well as the aperture efficiency for a scanning case (8 beams in this case) are examined to derive the optimal F-number.

Table 1. Parameters of Geometry I (Figure 3-1)

Hyper-hemispherical Lens		Hyperbolic Lens	
Permittivity ε_r^{hh}	11.9	Permittivity ε_r^{hb}	2.4
Diameter D_{hl}	$48\lambda_0$	Diameter D_{hb}	$82\lambda_0$
Truncation Angle θ_0	59.3^o	F-number $f_{hb}^{\#}$	2.1
Gaussian far field taper	$-11\ dB\ at\ 45^o$	Thickness h_{hb}	$19.8\lambda_0$

a. Central element (Broadside)

b. Displaced element (8 beams scanning)
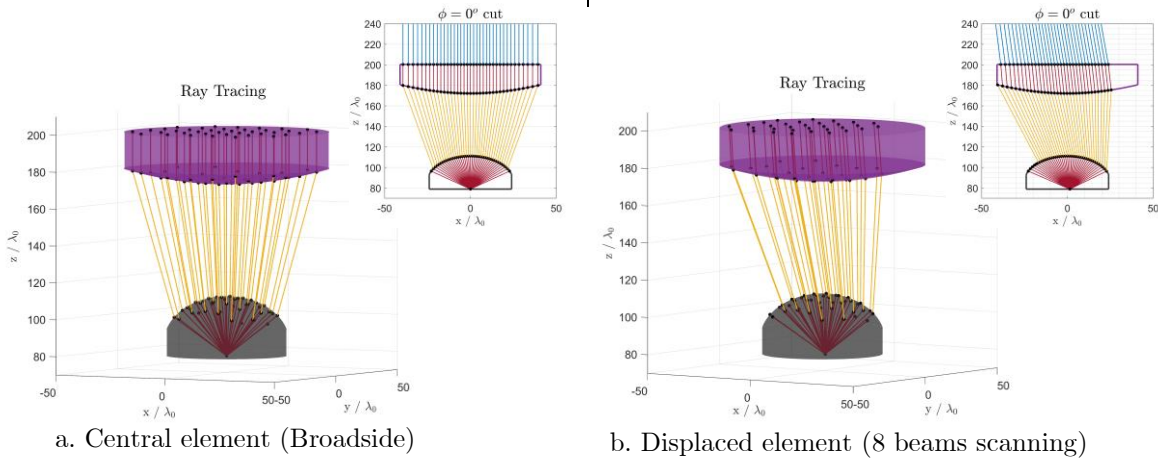
Figure 3-11. Geometry I: Focal Plane array of feeding elements under a Hyper-hemispherical Lens, Geometrically Coupled to a Hyperbolic Lens. In (a) the central element is examined (broadside), while in (b) a displaced element scanning at $\theta_{scan} \cong 8\lambda_0/D_{hb}$ is shown.
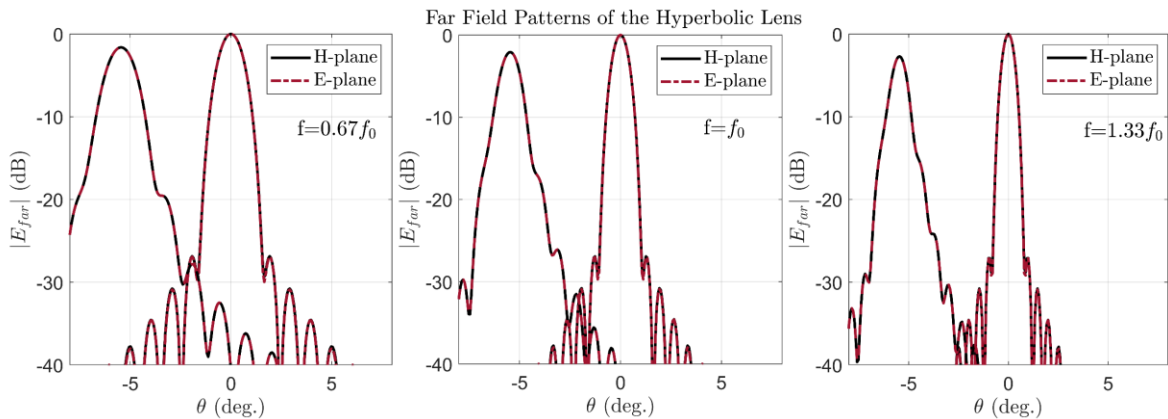
Figure 3-12. Far field pattern of the lens chain of Geometry I (Figure 3-11, Table 1), fed by a Gaussian feed, at three frequencies within a 1:2 bandwidth, for broadside and scanning to $\theta_{scan} \cong 8\lambda_0/D_{hb}$

The performance of the geometry described in Table 1 is shown in Figure 3-13, assuming (a) quarter wavelength matching layers at all surfaces, designed at the central frequency and (b) ideal wideband matching layers at all surfaces, operating over a bandwidth of 1:2. It can be observed that except for the effect of the matching layer, the performance of the central element is independent of frequency, due to the geometrical coupling between the lenses. As for the scanning performance, it is shown in Figure 3-14, for three different frequencies within a bandwidth of 1:2, where it can be observed that the scan loss increases with frequency, due to the phase matching between the field $\vec{E}_4^t$ (Figure 3-1), on the top surface of the hyperbolic lens and the plane wave incident on it. In fact, the higher the frequency, the more rapid the phase variation and thus the higher the loss due to scanning.
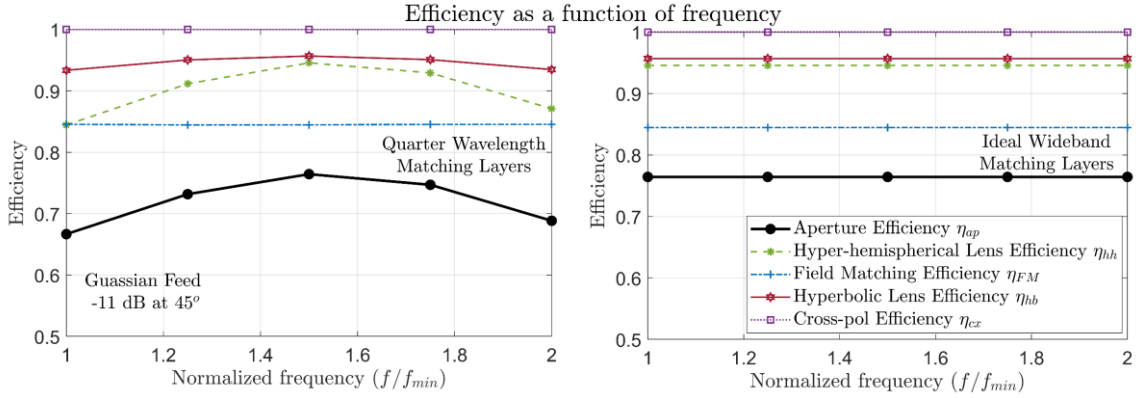
(a) Quarter wavelength matching layers at f_c (b) Ideal Wideband matching layers

Figure 3-13. Efficiency terms of Geometry I (Figure 3-11, Table 1), fed by a Gaussian feed. Green: illumination efficiency of the hyper-hemispherical lens, Red: efficiency terms related to the hyperbolic lens, Blue: field matching efficiency and Black: total aperture efficiency. In (a), quarter wavelength matching layers are considered in all surfaces, while in (b) wideband matching layers are considered in all surfaces.
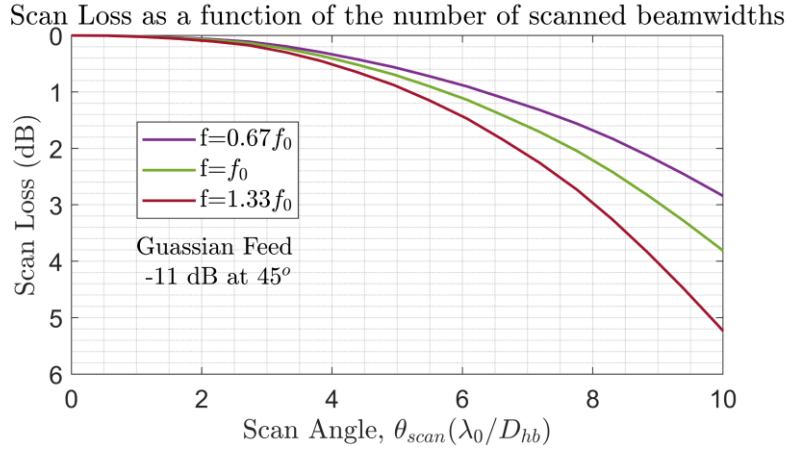
Figure 3-14. Scan Loss of Geometry I (Figure 3-11, Table 1), fed by a Gaussian feed, as a function of the number of scanned beamwidths, for different frequencies, within a bandwidth of 1:2.

3.5.2. Validation Using Physical Optics

The results presented in the previous section have been derived using an in-house GO code, developed based on the analysis methodology described in section 3.1. To evaluate the accuracy of this methodology, a validation has been performed using a much more computationally intensive multi-surface PO code. In Figure 3-15 the far field amplitude and phase derived using the methodology of section 3.1 are compared against a multi-surface PO code for (a) the central element (broadside), (b) a displaced element corresponding to $N = 4$ beamwidths scanning and (c) a displaced element corresponding to $N = 7$ beamwidths

scanning. Furthermore, the fields on the aperture on top of the hyperbolic lens are compared for the same cases in Figure 3-16. It is noted that the validation is performed for a similar design as the one presented in section 3.5.1 and an f-number of 2.2.

(a) Broadside

(b) $N = 4$ beams scanning
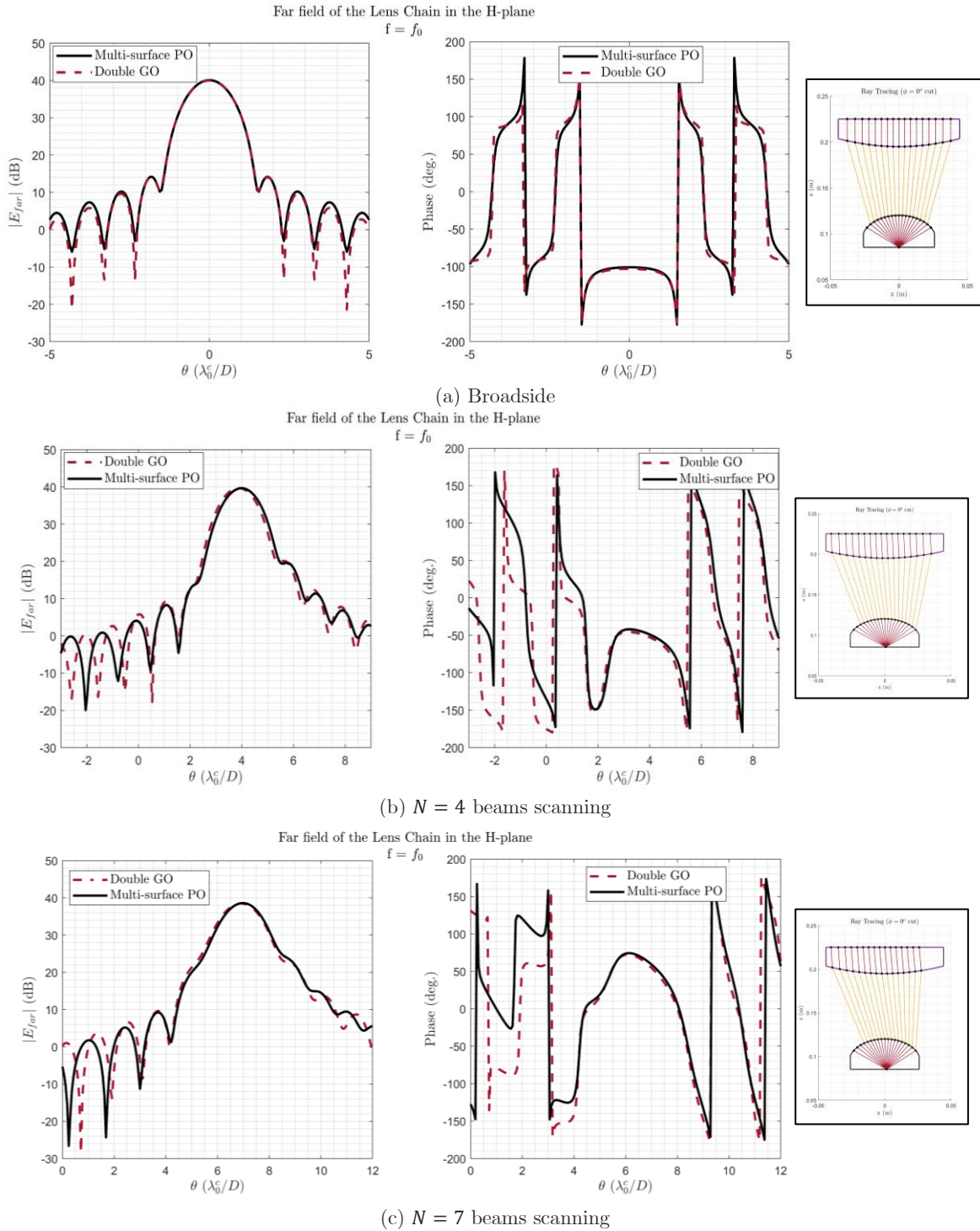
(c) $N = 7$ beams scanning

Figure 3-15. Amplitude and Phase of the far-field radiated by the Geometry I (Figure 3-11, Table 1), obtained by a double GO code as described in section 3.1 and compared against a multi-surface PO code: (a) broadside, (b) $N = 4$ beams scanning and (c) $N = 7$ beams scanning.

(a) Broadside

(b) $N = 4$ beams scanning
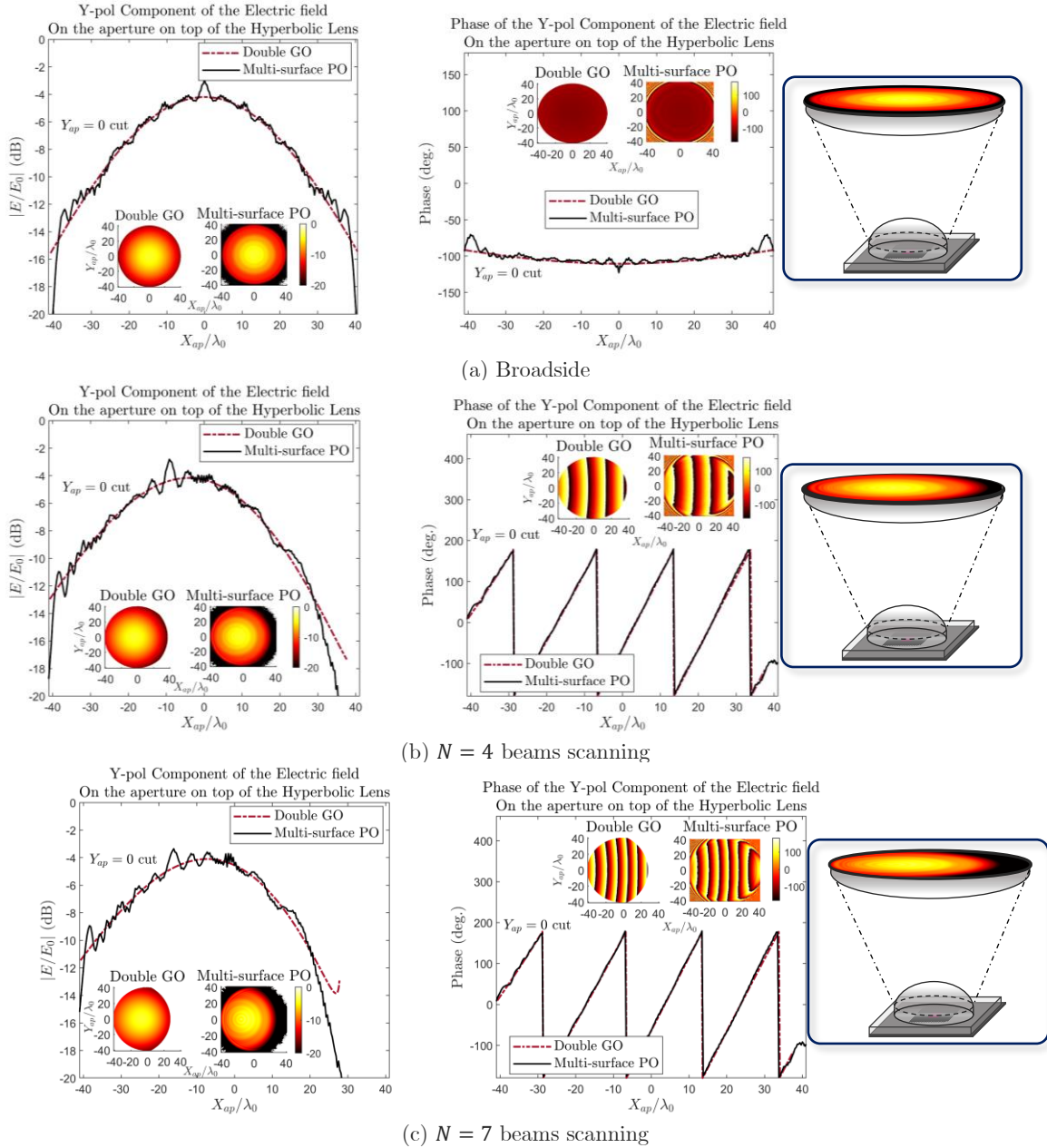
(c) $N = 7$ beams scanning

Figure 3-16. Field distribution on the top surface of the hyperbolic lens of Geometry I (Figure 3-11, Table 1), obtained by a double GO code as described in section 3.1 and compared against a multi-surface PO code: (a) broadside, (b) $N = 4$ beams scanning and (c) $N = 7$ beams scanning.

As observed from Figure 3-15 and Figure 3-16, the GO methodology is in excellent agreement with the multi-surface PO approach, rendering it reliable for the analysis of this geometry. It is noted that the oscillations in Figure 3-16 are related to artifacts of the PO analysis, due to the proximity of the surfaces.

The main advantage of the double GO approach is related to the calculation speed. In fact, the multi-surface PO code requires about 1,5 hour to analyse the geometry in a computer with 12$^\text{th}$ generation i5 processor with 3.00 GHz clock speed and 16,0 GB RAM memory, while the double GO method only 15 seconds for the same configuration.

3.6. Design based on a Tapered Leaky-Wave Slot Feeding Element

One of the main requirements of the TIFUUN quasi-optical system is its wide bandwidth of operation. Therefore, for the choice of the feeding element of the examined architectures, it is important to ensure wideband impedance matching, as well as to make sure that the feeding element in combination with the rest of the quasi-optical system feature a frequency-stable aperture efficiency. The chosen feeding element is a tapered leaky wave slot, i.e. a bowtie-shaped slot, etched on a metallic plane (ground plane) and kept at a small distance h_{gap} from the lens' dielectric. This geometry is matched throughout a wide frequency band, while also featuring certain parameters that allow us to partly influence its radiation pattern.

In particular, the far field radiated by such an antenna can be calculated using the Stationary Phase Point approximation of the spectral integral of the field radiated by a magnetic current distribution, as in Eq. 3.19.

$$\vec{E}_{FF} = jk_z\bar{\bar{G}}_{em}(k_x, k_y, z, z')e^{jk_z z}\vec{M}(k_x, k_y)\frac{e^{-jkr}}{2\pi r} , \qquad (3.19)$$

where $\bar{\bar{G}}_{em}(k_x, k_y, z, z')$ is the spectral Green's Function of the medium surrounding the antenna, and $\vec{M}(k_x, k_y)$ is the Fourier Transform of the equivalent magnetic current representing the slot. In this case, the medium is stratified, comprised of a ground plane with an etched slot, an air gap of height h_{gap} and a semi-infinite dielectric.

As a result of Eq. 3.19, the far field of a tapered leaky wave slot can be influenced either by the current distribution, or by the stratification, which in this case supports the excitation of leaky waves. Thus, the parameters that can have an impact on the pattern are, the cavity height h_{gap}, the length of the slot L_a and the tapering angle γ (Figure 3-17).

The design of the feeding element is performed in a full-wave simulator, namely CST Microwave Studio [25]. Prior to the design phase, a parametric analysis of this antenna is performed, similar to that presented in [26]- [27], which is then utilized for the design of the feeding element in order to satisfy the requirements of the geometry of Figure 3-1. To identify those requirements, one can resort to the analysis of the same geometry, fed by a Gaussian (or any ideal) feeding element, since in this case the performance of the quasi-optical system is evaluated independently of any frequency-dependent characteristics of the real antenna. For the geometry of a hyper-hemispherical lens geometrically coupled to a hyperbolic lens, this analysis is performed in section 3.5, where it is identified that due to the geometrical coupling, it features an inherently frequency independent behaviour for broadside and a scan loss that increases with frequency for off-broadside. The increase of scan loss with frequency is related to the phase distribution on the radiating aperture and cannot be easily controlled with the design of the feeding element. However, to enhance the frequency independent behaviour of the central element, one can design a feeding element with a far field pattern as frequency stable as possible.

Following this thought process, a tapered leaky wave slot is designed for this geometry, the parameters of which are shown in Table 2, while its far field patterns radiating into a semi-infinite dielectric (primary patterns) are presented in Figure 3-18. It is noted that once the leaky-wave feed is introduced, the parameters of the lenses are also tweaked to optimize the performance of the lens chain for this feed. The updated parameters are also given in Table 2, while in Figure 3-19 the far field patterns of the hyperbolic lens are presented for three different frequencies, within a bandwidth of 1:2.
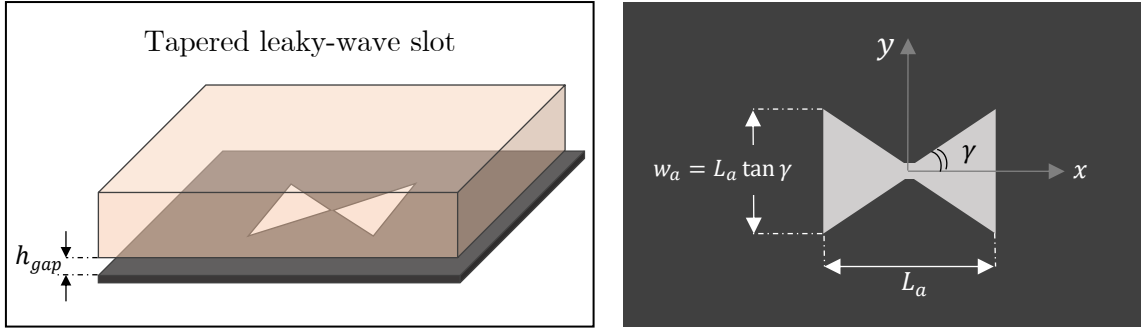
Figure 3-17. Tapered leaky-wave slot, radiating in a semi-infinite material with the permittivity of the lens.
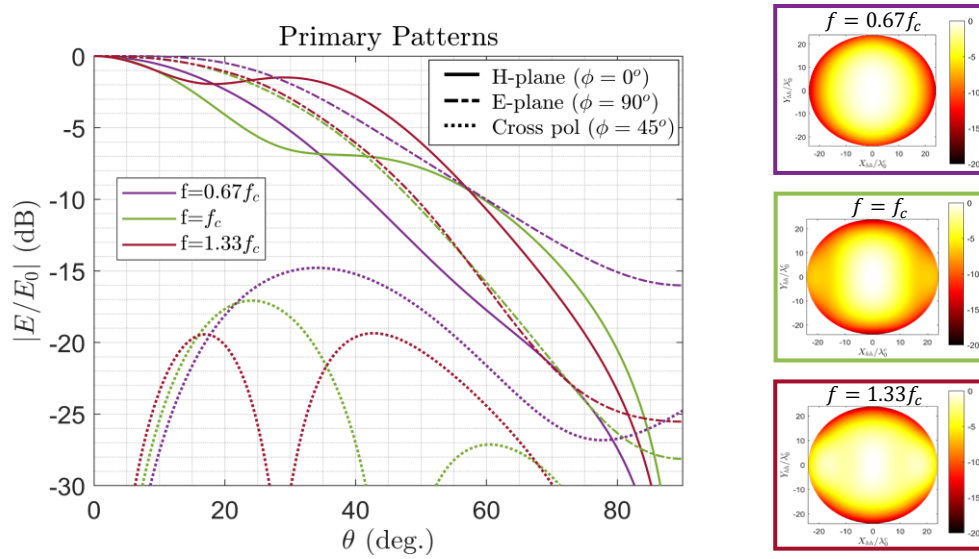
Figure 3-18. Primary patterns of the feeding element throughout a frequency band of 1:2. In the inset, the field incident of the hyper-hemispherical lens is shown in a surface plot.

Table 2. Parameters of Final Design of a hyper-hemispherical lens geometrically coupled to a hyperbolic lens

Tapered leaky wave slot		Hyper-hemispherical Lens		Hyperbolic Lens	
Slot Length L_a	$0.5\lambda_0$	Permittivity ε_r^{hh}	11.9	Permittivity ε_r^{hb}	2.4
Cavity height h_{gap}	$0.01\lambda_0$	Diameter D_{hh}	$48\lambda_0$	Diameter D_{hb}	$82\lambda_0$
Tapering Angle γ	40°	Truncation Angle θ_{trun}	54°	F-number $f_{hb}^{\#}$	2
Phase Centre Position (from the ground plane)	$-0.72\lambda_0$			Thickness h_{hb}	$19.8\lambda_0$
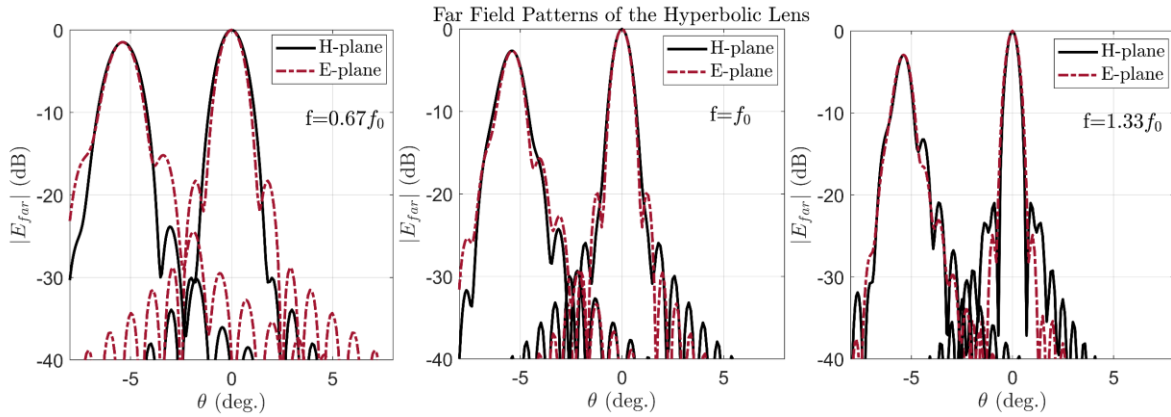
Figure 3-19. Far field pattern of the lens chain of Geometry I, fed by a Tapered Leaky Wave Slot (Table 2), at three frequencies within a 1:2 bandwidth, for broadside and scanning towards $\theta_{scan} \cong 8\lambda_0/D_{hb}$.

As observed from Figure 3-18, the primary patterns do not change significantly within a frequency band of 1:2, leading to an aperture efficiency for broadside, being also relatively stable with frequency, as shown in Figure 3-20. However, they are not rotationally symmetric, leading to a difference in the scanning performance with respect to the azimuthal angle of scanning. The scan loss in the two main planes is shown in Figure 3-21.

It is important to note at this point that due to the physical size of the feeding element, two adjacent feeds positioned inside the hyper-hemispherical lens, at a distance equal to $d_{feed} = L_a / \cos(\gamma)$, as shown in Figure 3-22, would create neighbouring beams in the image plane at an angular distance of $\Delta\theta \cong \varepsilon_r^{hh} d_{feed}/F_{hb}$. This is derived through Eq. 3.11-3.12 and it means that to fully sample the image plane, repointing of the telescope is required. For the parameters of Table 2, the distance in the image plane is $\Delta\theta \cong 4\lambda_0/D_{hb}$, as in Figure 3-22.

Overall, the geometry discussed in the current chapter features a high aperture efficiency for broadside, with a frequency dependency arising from the matching layers, as well as the feeding element. This means that the design of the feed is focused on achieving a wideband impedance matching, as well as a frequency stable radiation pattern. As for the scanning performance, the difference in the focal planes of the two quasi-optical components lead to a phase error when scanning, which increases the scan loss. As shown in section 3.3, the scanning performance could be improved by further increasing the diameter of the hyper-hemispherical lens. However, when the two lenses become too similar in size, it makes more sense to totally remove the hyperbolic lens and use a single elliptical lens instead.
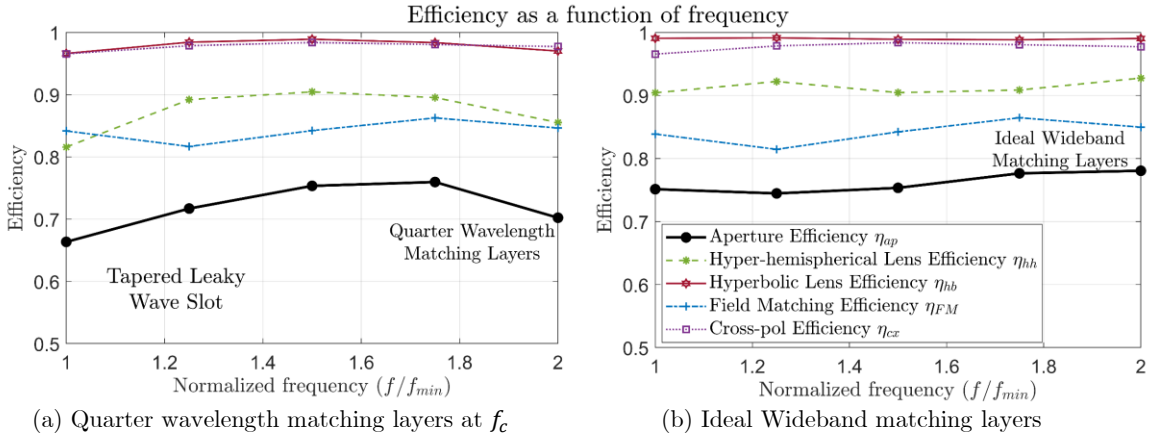
(a) Quarter wavelength matching layers at f_c (b) Ideal Wideband matching layers

Figure 3-20. Efficiency terms for the geometry of Figure 3-1, fed by a Tapered leaky wave slot. Green: illumination efficiency of the hyper-hemispherical lens, Red: efficiency terms related to the hyperbolic lens, Blue: field matching efficiency and Black: total aperture efficiency. In (a), quarter wavelength matching layers are considered in all surfaces, while in (b) wideband matching layers are considered in all surfaces.
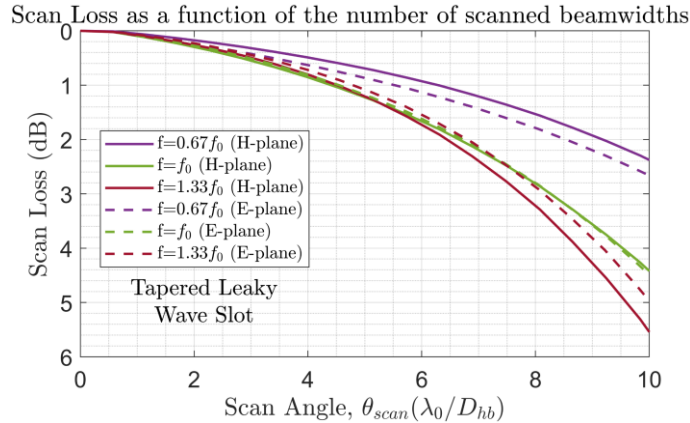
Figure 3-21. Scan Loss for the geometry of Figure 3-11, fed by a Tapered leaky wave slot, as a function of the number of scanned beamwidths, for different frequencies, within a bandwidth of 1:2. Solid lines are for scanning in the H-plane ($\varphi = 0^o$), while dashed lines correspond to scanning in the E-plane ($\varphi = 90^o$).
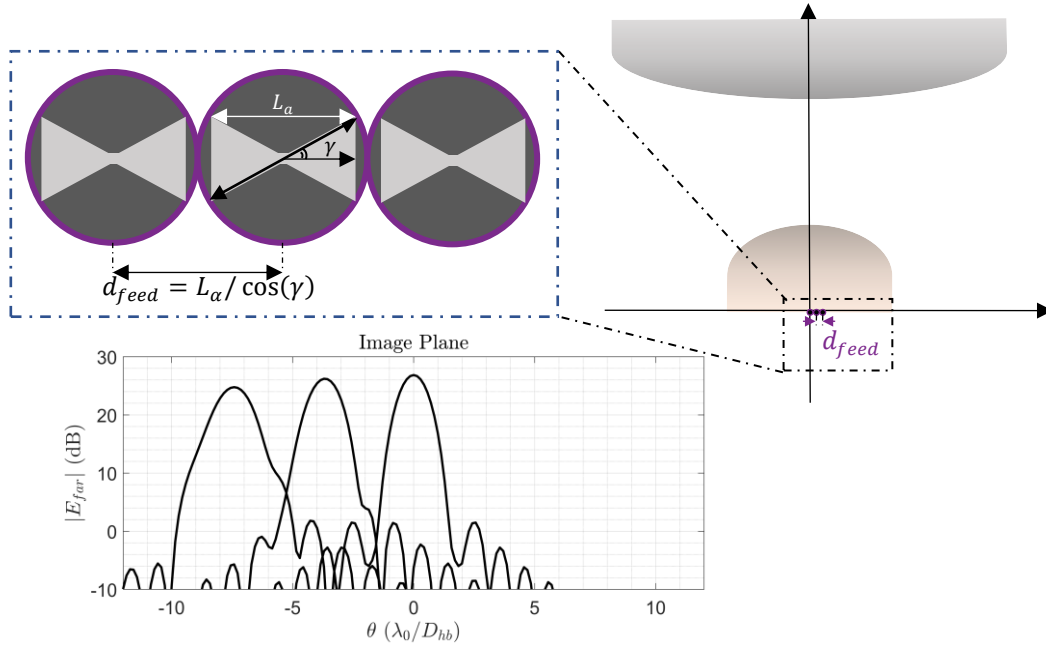
Figure 3-22. Adjacent feeds positioned inside the hyper-hemispherical lens, create neighbouring beams in the image plane at an angular distance of $\Delta\theta \cong \varepsilon_r^{hh} d_{feed}/F_{hb}$.

3.7. Shaping of the Lenses to Improve the Scanning Performance

Although increasing the diameter of the hyper-hemispherical lens can improve the scanning performance, it is not the only way to do so. Properly shaping the involved structures can be utilized instead to correct both for phase aberrations and for spill-over losses while scanning. In this case, chains of quasi-optical components provide more degrees of freedom to the shaping process, since there are more interfaces that can be used to decrease the phase error [20]. It is important to note though that the shaping also affects the frequency-dependency of the geometry.

In the framework of this work, the surface of the hyper-hemispherical lens, as well as the two surfaces of the hyperbolic lens are optimized to achieve the best trade-off between the broadside performance, as well as that of the edge elements of the focal plane array. Attention is also given to ensure that the optimization is valid throughout the frequency band of interest. The general process for symmetric shaping, using a genetic algorithm for the optimization of the surfaces, is described in Appendix D and suggests that the surface to be optimized can be expressed as a conic surface plus higher order polynomials. To optimize the performance of the structure, the kernel utilized is based on the analysis methodology described in section 3.1. This is possible since the GO propagation is performed numerically, by estimating the radii of curvature of the transmitted field, through the radii of curvature of the incident one in combination with the surface properties. This allows the use of this methodology, regardless of the types of surfaces, i.e. without the need of using only canonical components. However, attention should be given to the ray tracing step, since once the equations describing the surfaces become more complex, the analytical solution of the ray tracing equations becomes cumbersome. For this reason, in the framework of this work, the ray tracing after shaping is performed using an iterative Newton-Raphson technique, as described in Appendix C.

Regarding the choice of a cost function utilized for the optimization of the surfaces, since in this case the shaping is focused on improving mostly the phase matching between the

incident plane wave and the field transmitted from the hyperbolic lens, the inverse of the aperture efficiency for two cases, broadside and scanning towards $\theta_{scan} = 8\lambda_0/D_{hb}$, are utilized. In this case, the efficiency in the central frequency is assessed during the optimization, but the results are also evaluated based on the performance of the system over the operation frequency. An alternative approach would be to use the average of the aperture efficiency throughout the frequency band of interest, i.e. $\bar{\eta}_{ap} = (1/3)\sum_{i=1}^{3}\eta_{ap}(f_i)$, where $f_1 = f_{min}$, $f_2 = f_c$, $f_3 = f_{max}$.

It is noted that if the shaping was aimed at improving both spill-over and taper, both efficiency terms should have been used as objective functions to ensure that the optimization converges to the best trade-off between the two. The equations of the three surfaces that are optimized are given in Eq. 3-20-3.22 and illustrated in Figure 3-23, where c_m are the curvatures of the conic surfaces, κ_m are the conic constants and a_i^m are the polynomial coefficients.

$$z_1 = \frac{c_1\rho^2}{1+\sqrt{1-\kappa_1 c_1^2\rho^2}} + a_1^0 + \sum_{i=1}^{M} a_1^i\rho^{2i}, \tag{3.20}$$

$$z_2 = \frac{c_2\rho^2}{1+\sqrt{1-\kappa_2 c_2^2\rho^2}} + a_2^0 + \sum_{i=1}^{M} a_2^i\rho^{2i}, \tag{3.21}$$

$$z_3 = a_3^0 + \sum_{i=1}^{M} a_3^i\rho^{2i}, \tag{3.22}$$

The optimization is performed using a multi-objective genetic algorithm (matlab gamultiobj), as described in Appendix D. The polynomials utilized are of maximum 10th order, i.e. $M = 5$, and a set of solutions derived through this algorithm is given in Figure 3-24, where it can be verified that the scanning performance can be improved at the cost of the broadside performance. From this set of solutions, two are further examined, one that keeps the broadside efficiency in similar levels as the original design and improves slightly the scanning performance, and one that significantly improves the scanning by slightly degrading the broadside efficiency. It is noted though that for both cases, a high efficiency for the broadside element is targeted. Those points are marked in Figure 3-24, and their parameters are given in Table 3 and Table 4. For the definition of these parameters, the reference system is considered to be at the central feed location (Figure 3-23).
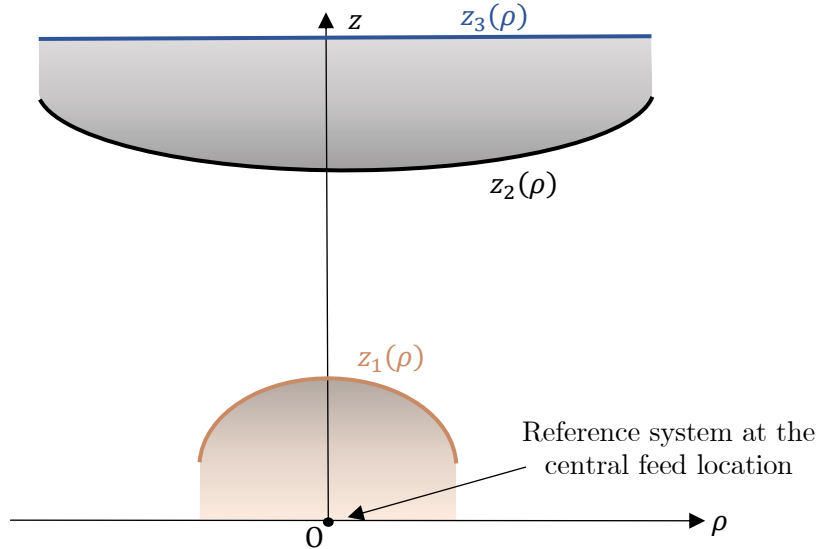
Figure 3-23. Multi-surface shaping performed to optimize the scanning performance of the geometry. The equations of the surfaces are expressed as conic surfaces plus higher order polynomials (Eq. 3-20-3.22), with the reference system at the location of the central feed.
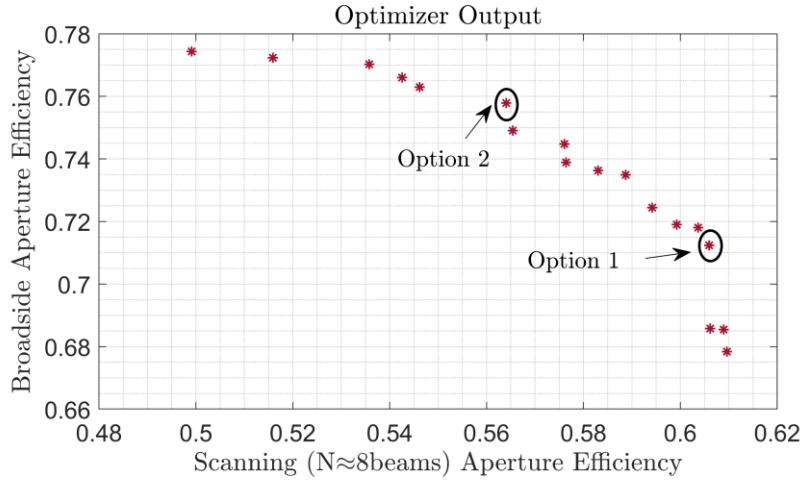
Figure 3-24. Output of the multiobjective genetic algorithm optimization for Geometry I, in terms of broadside and scanning aperture efficiency.

Table 3. Optimization parameters for shaping the three surfaces of Geometry I – Option 1

Lens Surface 1 (originally hyper-hemispherical)

$c_1(m^{-1})$	κ_1	a_1^0	$a_1^1(m^{-1})$	$a_1^2(m^{-3})$	$a_1^3(m^{-5})$	$a_1^4(m^{-7})$	$a_1^5(m^{-9})$
-3.33 $\times 10^4 \lambda_0$	$918.24\lambda_0$	$33.01\lambda_0$	$129.25\lambda_0$	1.98 $\times 10^5 \lambda_0$	1.36 $\times 10^8 \lambda_0$	-1.64 $\times 10^{11}\lambda_0$	-1.18 $\times 10^{14}\lambda_0$

Lens Surface 2 (originally hyperbolic bottom)

$c_2(m^{-1})$	κ_2	a_2^0	$a_2^1(m^{-1})$	$a_2^2(m^{-3})$	$a_2^3(m^{-5})$	$a_2^4(m^{-7})$	$a_2^5(m^{-9})$
9.389 $\times 10^3 \lambda_0$	-1.326 $\times 10^3 \lambda_0$	$88.47\lambda_0$	$42\lambda_0$	7.38 $\times 10^4 \lambda_0$	2.39 $\times 10^6 \lambda_0$	2.99 $\times 10^8 \lambda_0$	1.03 $\times 10^{13}\lambda_0$

Lens Surface 3 (originally hyperbolic top)

$c_3(m^{-1})$	κ_3	a_3^0	$a_3^1(m^{-1})$	$a_3^2(m^{-3})$	$a_3^3(m^{-5})$	$a_3^4(m^{-7})$	$a_3^5(m^{-9})$
0	0	$109.325\lambda_0$	$-44.42\lambda_0$	6.92 $\times 10^3 \lambda_0$	2.28 $\times 10^7 \lambda_0$	9.76 $\times 10^9 \lambda_0$	5.21 $\times 10^{12}\lambda_0$
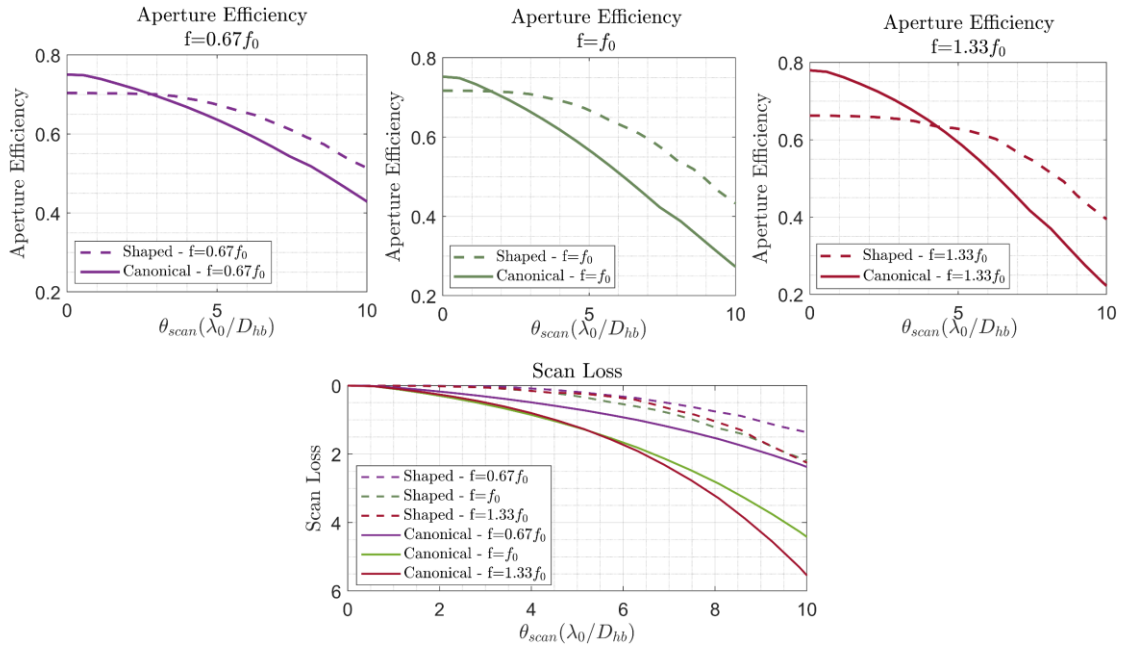
Figure 3-25. Aperture Efficiency (top) and scan loss (bottom), as a function of the scan angle before and after shaping the lens surfaces, for three frequency points within a 1:2 bandwidth. The parameters of this shaping option are given in Table 3 (Option 1).

Table 4. Optimization parameters for shaping the three surfaces of Geometry I – Option 2

Lens Surface 1 (originally hyper-hemispherical)							
$c_1(m^{-1})$	κ_1	a_1^0	$a_1^1(m^{-1})$	$a_1^2(m^{-3})$	$a_1^3(m^{-5})$	$a_1^4(m^{-7})$	$a_1^5(m^{-9})$
$-3.299 \times 10^4 \lambda_0$	$922.274\lambda_0$	$33.45\lambda_0$	$70.65\lambda_0$	$1.95 \times 10^5 \lambda_0$	$6.18 \times 10^7 \lambda_0$	$-4.22 \times 10^{10} \lambda_0$	$-7.88 \times 10^{13} \lambda_0$
Lens Surface 2 (originally hyperbolic bottom)							
$c_2(m^{-1})$	κ_2	a_2^0	$a_2^1(m^{-1})$	$a_2^2(m^{-3})$	$a_2^3(m^{-5})$	$a_2^4(m^{-7})$	$a_2^5(m^{-9})$
$9.324 \times 10^3 \lambda_0$	$-1.349 \times 10^3 \lambda_0$	$87.79\lambda_0$	$7.52\lambda_0$	$4.66 \times 10^4 \lambda_0$	$-5.89 \times 10^6 \lambda_0$	$-4.71 \times 10^8 \lambda_0$	$5.84 \times 10^{12} \lambda_0$
Lens Surface 3 (originally hyperbolic top)							
$c_3(m^{-1})$	κ_3	a_3^0	$a_3^1(m^{-1})$	$a_3^2(m^{-3})$	$a_3^3(m^{-5})$	$a_3^4(m^{-7})$	$a_3^5(m^{-9})$
0	0	$109.96\lambda_0$	$22.1\lambda_0$	$9.75 \times 10^3 \lambda_0$	$1.11 \times 10^7 \lambda_0$	$1.43 \times 10^9 \lambda_0$	$4.28 \times 10^{12} \lambda_0$
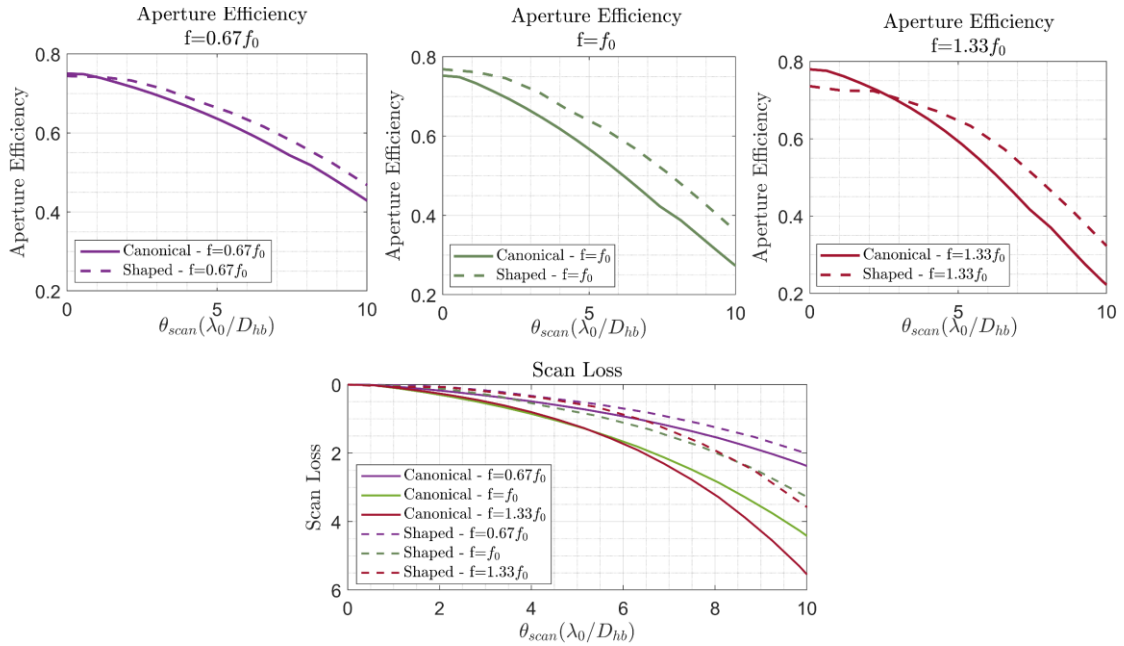
Figure 3-26. Aperture Efficiency (top) and scan loss (bottom), as a function of the scan angle before and after shaping the lens surfaces, for three frequency points within a 1:2 bandwidth. The parameters of this shaping option are given in Table 5 (Option 2).

It is interesting to note that between the two solutions examined, the main difference in the parameters is in the higher order polynomial coefficients. This further supports the fact that since the utilized components are electrically large, the focus of the optimization is to correct for phase aberrations. Therefore, the higher order polynomials are those that determine the difference in the scanning performance. Off course, the convergence of the algorithm into certain solutions also depends on the objective function chosen for the optimization, as well as the initial conditions. Therefore, it is interesting as a future step to explore more the algorithmic aspect of this process, since it determines the output of the optimizer.

From the two examined cases, the first one (Table 3 and Figure 3-25) is more interesting, since without significant impact on the broadside efficiency, the scanning performance is clearly improved. It is though expected that without affecting the broadside efficiency, as in the second example presented, it is difficult, if not impossible, to significantly improve the scanning performance. To showcase the impact of the shaping in the first case (Table 3, Figure 3-25), the ray picture, as well as the far field patterns for broadside and scanning towards $\theta_{scan} = 10\lambda_0/D_{hb}$ is shown in Figure 3-27. In this figure, it is clearly observed that while for broadside the difference in pattern properties and gain is minimal, for the scanning case, after shaping,

the gain is higher, the main lobe is narrower and the relative level of the sidelobes is lower, indicating an overall better performance.
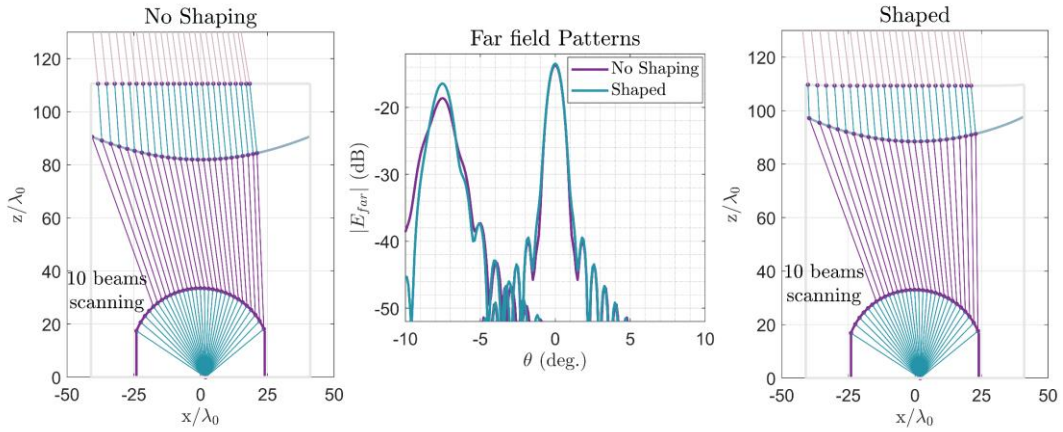
Figure 3-27. Ray tracing picture before (left) and after (right) shaping the dielectric-air surfaces, for scanning towards $\theta_{scan} = 10\lambda_0/D_{hb}$. In the middle figure, the far field patterns before and after shaping are showcased for broadside and scanning towards $\theta_{scan} = 10\lambda_0/D_{hb}$.

Chapter 4.
Diffractively Coupled Lens Chain

Hyperbolic Lens coupled to an Array of Small Focal Lenses

4.1. Analysis Methodology

The second candidate geometry for the TIFUUN building block, is shown in Figure 2-5(a), and similarly to the one discussed in Chapter 3, it deals with a multi-surface propagation scenario. In this case, the feeding lens is positioned close to the focal point of the hyperbola and thus the double GO approach discussed in section 3.1 cannot be applied. Instead, as discussed in section 2.2 a Coherent Fourier Optics technique is the preferred technique for analysing such geometries. The steps of this methodology are summarized below.

1. Calculate the field incident on the hyperbolic lens top $\left(\vec{E}_1^i\right)$.
2. Transmit the field to the inner surface of the hyperbolic lens top $\left(\vec{E}_1^t\right)$.
3. Propagate the field from the top inner surface to the bottom inner surface of the hyperbolic lens $\left(\vec{E}_2^i\right)$, using GO propagation.
4. Transmit the field to the bottom outer surface of the hyperbolic lens $\left(\vec{E}_2^t\right)$.
5. Propagate the field from the bottom outer surface of the hyperbolic lens, to the FO sphere, using GO propagation $\left(\vec{E}_{GO}\right)$.
6. Derive the field incident on the surface of the small focal lens, by coherently summing the Plane Wave Spectrum derived using the CFO technique $\left(\vec{E}_l^{Rx}\right)$.
7. Derive the field transmitted through the surface of the small focal lens by the feed, in transmission mode $\left(\vec{E}_l^{Tx}\right)$.
8. Perform the reaction integral on the surface of the focal lens to derive the aperture efficiency.
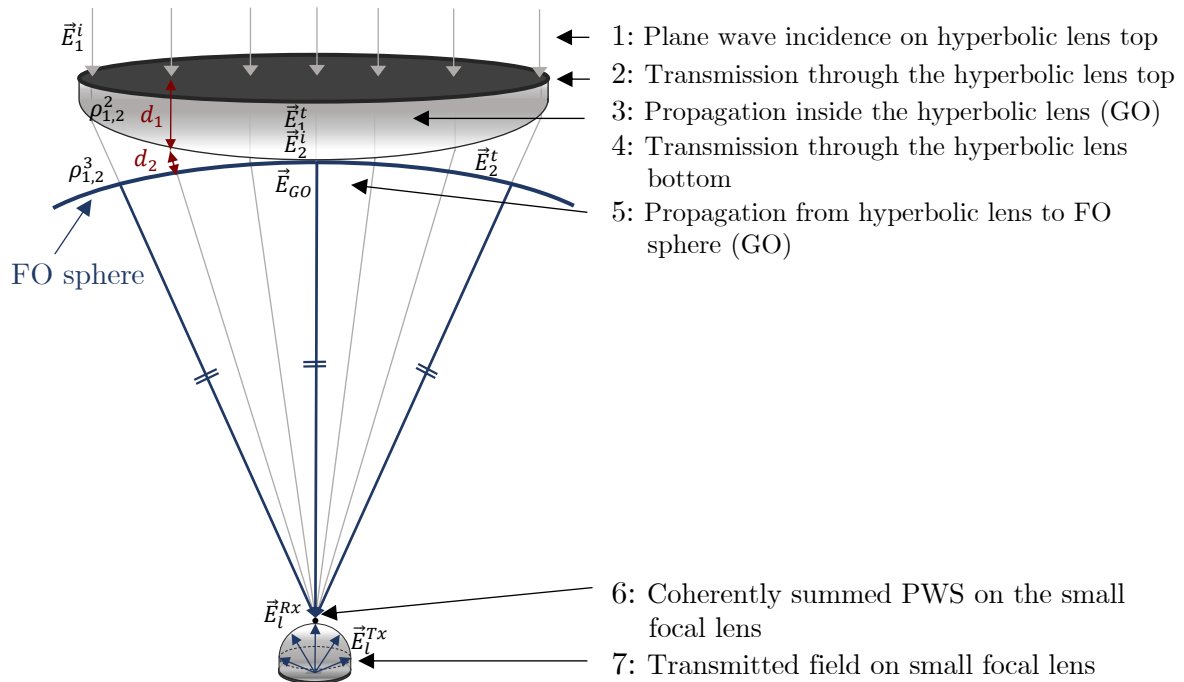
Figure 4-1. Candidate Geometry II: Small Focal Lens, Diffractively Coupled to Hyperbolic Lens.

To apply the CFO technique to the geometry of Figure 2-5(a), the first step is to evaluate a plane wave incident on the hyperbolic lens top $\left(\vec{E}_1^i = \vec{E}_{pw}^{inc}\right)$, as in Eq. 2.10. Subsequently, this field is transmitted through the top of the hyperbolic lens, propagated inside the dielectric material of the hyperbolic lens and transmitted through its bottom surface (Eq. 4.1 – 4.3).

$$\vec{E}_1^t = \bar{\bar{\tau}}_1 \cdot \vec{E}_1^i \tag{4.1}$$

$$\vec{E}_2^i = \vec{E}_1^t \sqrt{\frac{\rho_1^2 \rho_2^2}{(\rho_1^2 + d_1)(\rho_2^2 + d_1)}} \cdot e^{-jk_3 d_1}, \tag{4.2}$$

$$\vec{E}_2^t = \bar{\bar{\tau}}_2 \cdot \vec{E}_2^i \tag{4.3}$$

where $\bar{\bar{\tau}}_1$, $\bar{\bar{\tau}}_2$ are the transmission dyads corresponding to transmission through the top and bottom surfaces of the hyperbolic lens respectively, $k_3 = k_0 \sqrt{\varepsilon_r^{hb}}$ is the propagation constant inside the hyperbolic lens' dielectric and $\rho_{1,2}^2$ are the radii of curvature of the wave front transmitted from the hyperbolic lens top. Furthermore, $d_1 = \left|\overrightarrow{Q_{hb}^{top} Q_{hb}^{bot}}\right|$ is the distance covered by the rays inside the hyperbolic lens, calculated using ray tracing (Appendix C). The field on the bottom of the hyperbolic lens can be then propagated, using GO propagation to an auxiliary sphere, called FO sphere, to facilitate the calculation of the focal field as a summation of plane waves (CFO technique, Eq. 2-18-2.20). This is done through Eq. 4.4.

$$\vec{E}_{GO} = \vec{E}_2^t \sqrt{\frac{\rho_1^3 \rho_2^3}{(\rho_1^3 + d_2)(\rho_2^3 + d_2)}} \cdot e^{-jk_0 d_2}, \tag{4.4}$$

where $\rho_{1,2}^3$ are the radii of curvature of the wave front transmitted from the hyperbolic lens, which can be calculated as a function of the properties of the incident wave front ($\rho_{1,2}^2$), the curvature of the surface of incidence and the permittivity of the hyperbolic lens. k_0 is the propagation constant in free space and $d_2 = \left|\overrightarrow{Q_{hb}^{bot} Q_{FO}}\right|$ the distance covered by the rays from the hyperbolic lens bottom to the FO sphere (Figure 4-1), calculated with ray tracing (Appendix C).

Using the field distribution on the FO sphere, the field incident on top of the small focal lens can be derived through Eq. 2.18-2.20. The field transmitted through the same lens, from the feed side, can also be derived through Eq. 2.21 and subsequently, the aperture efficiency of the structure can be calculated through the reaction integral between those two field distributions $\left(\vec{E}_l^{Rx}, \vec{E}_l^{Tx}\right)$, using Eq. 2.11.

4.2. Design Guidelines

As mentioned in section 2.2.2 and 4.1, to examine the performance of a focal plane array comprised of a primary focusing component and an array of focal lenses with the Coherent Fourier Optics technique, an auxiliary sphere is used, referred to as FO sphere. The derivation of the focal field, as a function of the GO field evaluated on the FO sphere includes some approximations, leading to an applicability region for each of the utilized FO spheres (centered around O_m, as shown in Figure 4-2). This applicability region has been derived in [19] and the final expression is given in Eq. 4.5. It depends on the maximum acceptable errors in the magnitude (ε) and phase (ε_φ) of the evaluated integrand, the radius of the mth FO sphere (R_m), as well as the angle θ_m from the centre of the FO sphere to the edge of the focusing component, as shown in Figure 4-2 for a hyperbolic lens. This means that the examined feeding element should be within the applicability region of the respective FO sphere to accurately represent the focal field.
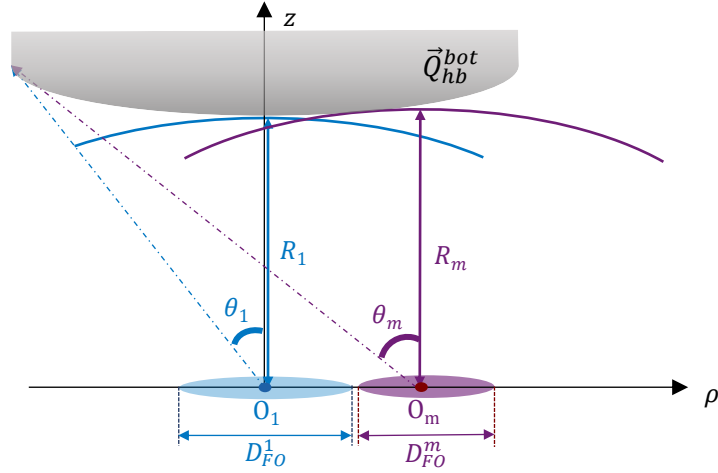
Figure 4-2. Representation of a hyperbolic lens and two FO spheres, one on-focus and one off-focus.

$$D_{FO}^m = 2 \min \left\{ \varepsilon R_m, \ \frac{1}{\sin(\theta_m)} \sqrt{\frac{\varepsilon_\varphi \lambda_0 R_m}{\pi}} \right\}, \tag{4.5}$$

where the radius of the m$^{\text{th}}$ FO sphere is derived such that the sphere is centered around O_m and tangent to the hyperbolic lens at a single position, i.e. $R_m = \min \left\{ \left| \overrightarrow{O_m Q_{hb}^{bot}} \right| \right\}$.

4.3. Feeding Lens

The small focal lens utilized as a feeding element of the hyperbolic lens can be either elliptical or hyper-hemispherical. In terms of the physical composition of the geometry, the difference between the two is the position of the lens with respect to the focus of the primary feeding element (hyperbolic lens). In the hyper-hemispherical lens case, the virtual focus should be shared with the focus of the hyperbolic lens, while in the elliptical lens case, the tip of the ellipse should coincide with the focus of the hyperbola, as shown in Figure 4-3.
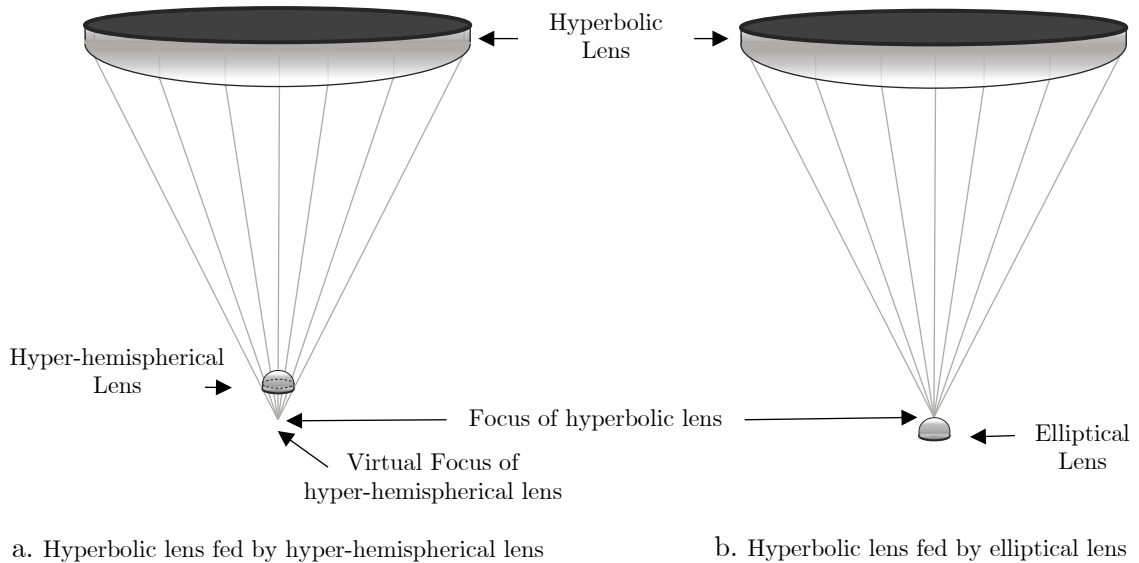
a. Hyperbolic lens fed by hyper-hemispherical lens

b. Hyperbolic lens fed by elliptical lens

Figure 4-3. Candidate Geometry II: Hyperbolic Lens, fed by (a) a hyper-hemispherical lens, and (b) an elliptical lens. In the two geometries, the focus of the primary component (hyperbolic lens) coincides (a) with the virtual focus of the hyper-hemisphere and (b) with the tip of the ellipse.

In terms of performance, the difference between these two lenses depends also on the diameter of the lenses. For small lens diameters in terms of wavelength, the performance of the hyper-hemispherical and elliptical lens is very similar, due the dominance of diffraction effects, as shown in Figure 4-4(a)-(b). However, this is not true when the lens diameter is increased. In particular, as the diameter of the lens increases, the far field patterns of the two lens types start to diverge significantly, with the elliptical lens featuring a much higher directivity, and the hyper-hemispherical lens featuring a broader but frequency-stable pattern (Figure 4-4(c)-(d)). This is due to the nature of the wave front radiated by an electrically large hyper-hemispherical lens, which, regardless of its size with respect to the wavelength, appears to originate from the same virtual focus. To further elaborate on this behaviour, one can examine different sizes of hyper-hemispherical lenses, operating at a single frequency. If those are electrically large, their radiation properties are very similar. An interpretation of this behaviour is that the field at each point of a far field sphere is dominated by the contribution of the direct ray transmitted out of the lens towards said direction. In other words, within the solid angle defined by the hyper-hemispherical lens, the far field is equivalent to the GO field and thus its properties are similar to those of the feeding element. This is not true for a small hyper-hemispherical lens, where diffraction effects play a much more important role. To showcase the above, the ray picture, as well as the far field patterns of hyper-hemispherical lenses with different diameters are plotted in Figure 4-5. The far-field patterns of Figure 4-5(b) are obtained using an in-house PO code. The GO fields are also calculated at the same far-field sphere and are plotted in Figure 4-5(b), together with the PO fields.

For the TIFUUN building block, the diameters of the lenses are limited by the physical space available inside the cryostat and it is required to be as small as possible. Therefore, a lens of around $D_{lens} \cong 3.5\lambda_0$ is chosen for this design. Smaller lenses would not perform as estimated with the methodologies discussed in Chapter 2, since the techniques used are not accurate for such electrically small curvatures. Between the hyper-hemispherical and the elliptical lens of this diameter, the elliptical lens features better defined main and side lobes and thus the rest of the design is focused on elliptical lenses as feeding elements of the hyperbolic lens.
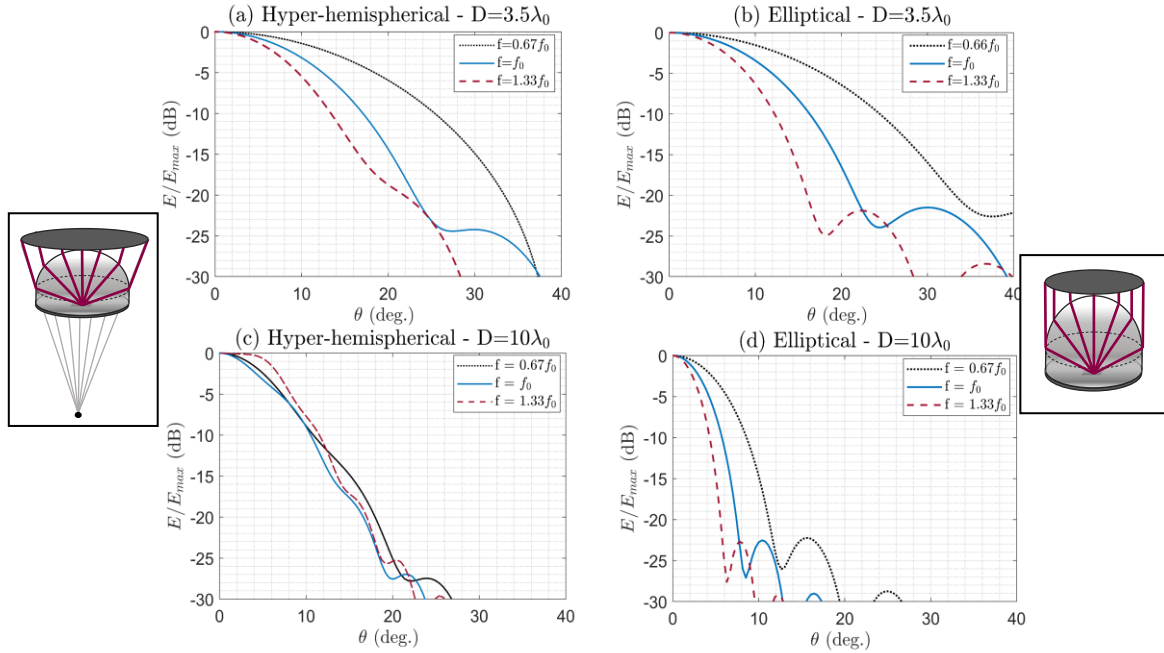
Figure 4-4. Far field patterns of (a) hyper-hemispherical and (b) elliptical lens of diameter $D = 3.5\lambda_0$ and $D = 10\lambda_0$ within a frequency range of 1:2, fed by similar ideal feeding elements, with Gaussian-shaped far fields.

(a) Ray picture   (b) Far field patterns
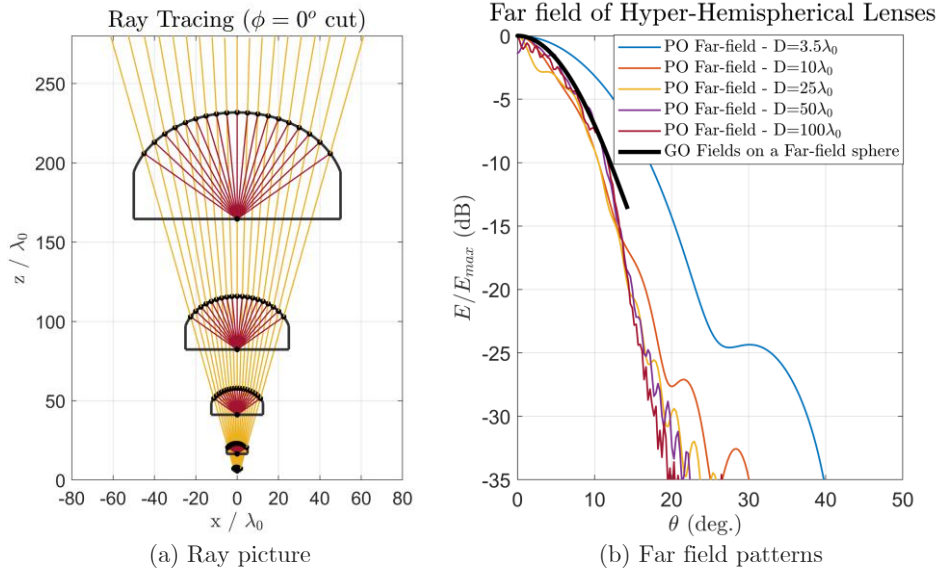
Figure 4-5. Hyper-hemispherical lenses with different diameters – (a) Ray Tracing and (b) Far Field Patterns.

4.4. Figures of Merit

To better evaluate the performance of this geometry, the aperture efficiency is decomposed into a number of efficiency terms. These are not the same as the ones presented in section 3.4, due to the different analysis methodology. However, the total aperture efficiency is the same, regardless of the analysis methodology.

- **Illumination efficiency of the focal lens η_{il}**, i.e. reflections and spill-over in the elliptical lens in transmission mode (Eq. 4.6).

$$\eta_{il} = \frac{P_l^{Tx}}{P_{feed}}, \tag{4.6}$$

where P_l^{Tx} is the power transmitted out of the lens and P_{feed} is the power radiated by the feeding element.

- **Quasi-optical radiation efficiency η_{QO}.** It is noted that this term depends on the hyperbolic lens f-number, as well as the diameter and truncation angle of the elliptical lens, but not on the feeding element of the elliptical lens.

$$\eta_{QO} = \frac{P_l^{Rx}}{P_{inc}}, \tag{4.7}$$

where P_l^{Rx} is the power related to the field incident on the small focal lens ($\vec{E}_l^{Rx}$ of Figure 4-1) and P_{inc} is the power of the incident plane wave (Eq. 2.16), over the flat side of the hyperbola.

- **Field matching efficiency η_{FM}**. This term depends on the field matching between the field transmitted out of the elliptical lens in transmission mode $\vec{E}_l^{Tx}$ and the received field $\vec{E}_l^{Rx}$ (Figure 4-1).

$$\eta_{FM} = \frac{|V_{oc}I_{Tx}|^2}{16P_l^{Rx}P_l^{Tx}}, \tag{4.8}$$

where $V_{oc}I_{Tx} = \iint\{\vec{H}_l^{Rx} \cdot \vec{m}_{eq} - \vec{E}_l^{Rx} \cdot \vec{j}_{eq}\}dS_l,\ \ \vec{m}_{eq} = -\hat{n}_Q \times \vec{E}_l^{Tx},\ \ \vec{j}_{eq} = \hat{n}_Q \times \vec{H}_l^{Tx}$ (Figure 4-1).

- **Cross-polarization efficiency η_{cx}**, as in Eq. 3.17. This term is already accounted for in the field matching efficiency. So the aperture efficiency is:

$$\eta_{ap} = \eta_{il} \cdot \eta_{hb} \cdot \eta_{FM}, \tag{4.9}$$

4.5. Preliminary Design, based on a Gaussian-shaped Feeding Element

4.5.1. Design & Performance

Similarly to the case of the geometrically coupled system, in the first stage of the design process, a Gaussian feeding element, as described in section 3.5, is utilized to illuminate the elliptical lens. Having chosen the diameter of the feeding lens equal to $D_{lens} = 3.5\lambda_0$, the focal distance to diameter ratio of the hyperbolic lens is chosen such that the N$^{\text{th}}$ element of the focal plane array receives optimally a plane wave incident from $\theta_{inc} = N\lambda_0/D_{hb}$, $N = 0,2,4\ldots$ (maximum gain sampling). As discussed in section 3.3, for a hyperbolic lens, the relation between the scan angle and the flash point is approximately $\rho_v \cong N\lambda_0 F_{hb}/D_{hb}$. However, since the rays do not converge to a single point for off-broadside incidence (Figure 3-6), to derive the optimal focal distance to diameter ratio of the hyperbola for a specific lens diameter, it is better to perform a parametric analysis, such as the one shown in Figure 4-6, where the aperture efficiency for broadside, as well as for plane wave incidence from $\theta_{inc} = 12\lambda_0/D_{hb}$ is presented as a function of the hyperbolic lens f-number. It is noted that for this analysis, the diameters of the lenses are the same, while the focal distance is altered.
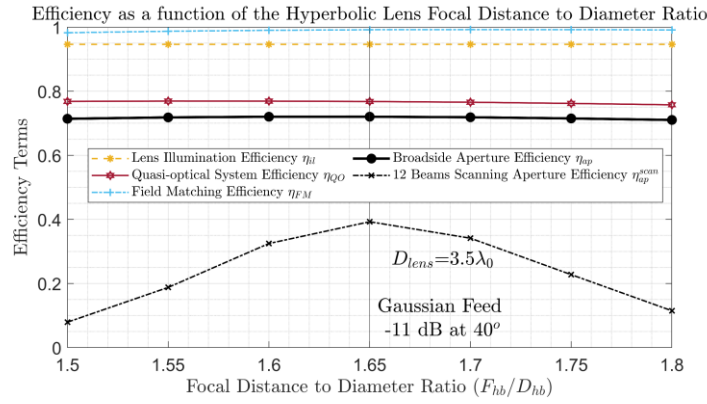
Figure 4-6. Efficiency Terms as a function of the Focal Distance to Diameter ratio $\left(f_\#^{hb}\right)$ of the hyperbolic lens. The diameters of the elliptical and hyperbolic lenses are kept constant and the focal distance is altered. Both the aperture efficiency at broadside, as well as the aperture efficiency for a scanning case ($\theta_{scan} = 12\lambda_0/D_{hb}$) are examined to derive the optimal F-number.

From the parametric analysis of Figure 4-6, it can be derived that the optimal focal distance to diameter ratio of the hyperbola is equal to 1.65, which means that $D_{lens} = 2.12\lambda_0 F_{hb}/D_{hb}$. All parameters of the lenses are given in Table 5, the geometry is shown in Figure 4-7 and the radiation patterns for three frequencies within a bandwidth of 1:2 are presented in Figure 4-8. The parameters presented in Table 5 are described in detail in Appendix A.3 and A.2.

Table 5. Parameters of Geometry II (Figure 4-7)

Hyper-hemispherical Lens		Hyperbolic Lens	
Permittivity ε_r^{hh}	11.9	Permittivity ε_r^{hb}	2.4
Diameter D_{hl}	$3.5\lambda_0$	Diameter D_{hb}	$82\lambda_0$
Truncation Angle θ_0	52°	F-number $f_{hb}^\#$	1.65
Gaussian feed taper	$-11\,dB\,at\,40^o$	Thickness h_{hb}	$19.8\lambda_0$
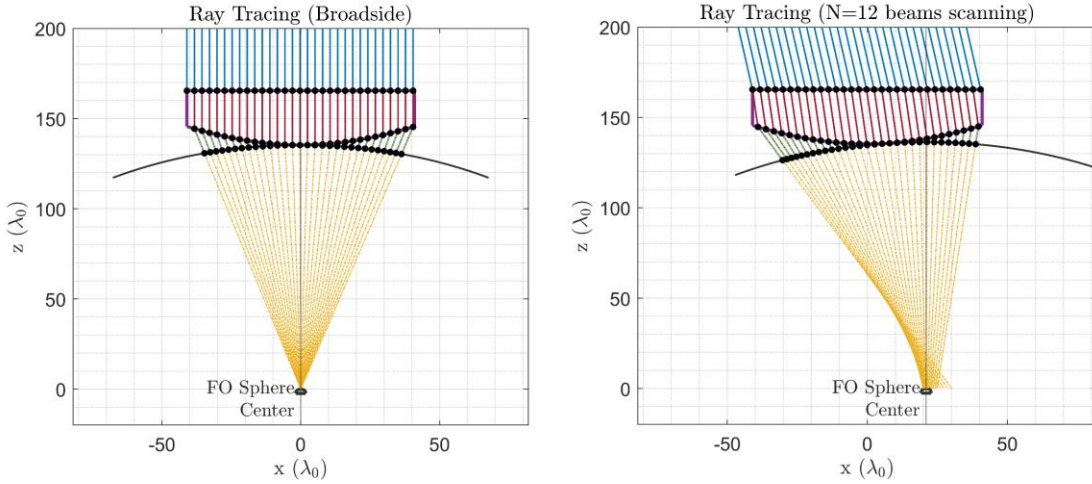
Figure 4-7. Geometry II: Focal Plane array of small focal lenses (elliptical), diffractively coupled to a hyperbolic lens. In (a) the central element is examined (broadside), while in (b) a displaced element scanning at $\theta_{scan} = 12\lambda_0/D_{hb}$ is shown.
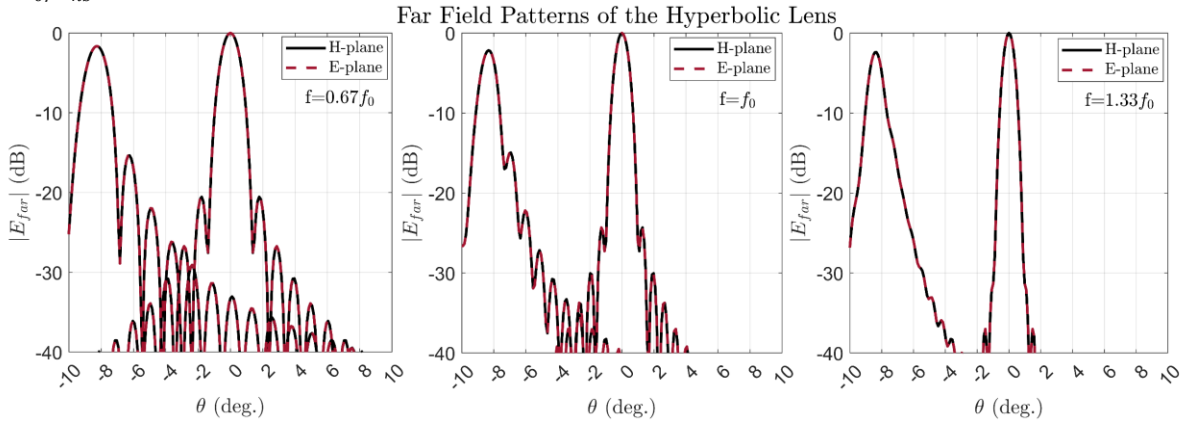
Figure 4-8. Far field pattern of the lens chain of Geometry II (Figure 4-7, Table 5), fed by a Gaussian feed, at three frequencies within a 1:2 bandwidth, for broadside and scanning to $\theta_{scan} = 12\lambda_0/D_{hb}$.

The broadside performance of the geometry described in Table 5 is shown in Figure 4-9, assuming (a) quarter wavelength matching layers at all surfaces, designed at the central frequency and (b) ideal wideband matching layers at all surfaces, operating over a bandwidth of 1:2. Contrary to Geometry I (Figure 3-20), the efficiency terms are frequency dependent, even when ideal wideband matching layers are utilized, due to the diffractive coupling between the quasi-optical components.

(a) Quarter wavelength matching layers at f_c (b) Ideal Wideband matching layers
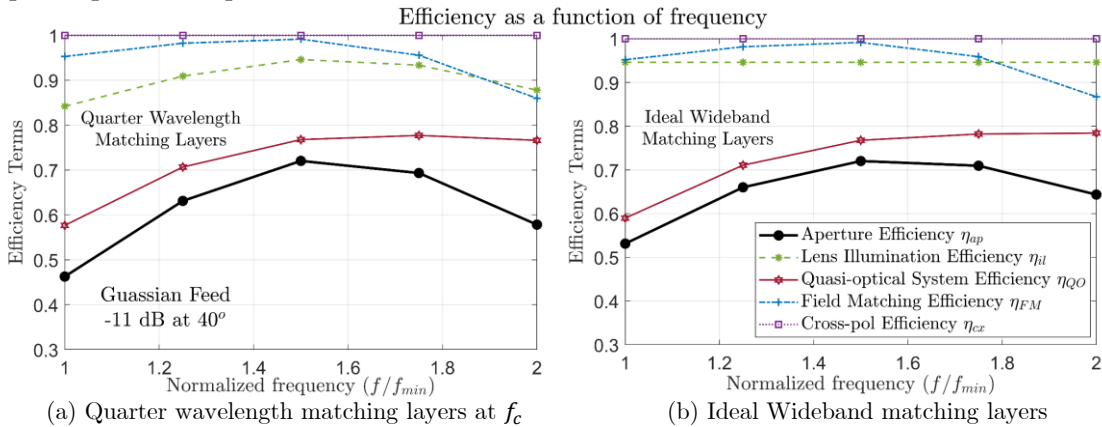
Figure 4-9. Efficiency terms for Geometry II (Figure 4-7, Table 5), fed by a Gaussian feed. Green: illumination efficiency of the elliptical lens, Red: quasi-optical system radiation efficiency, Blue: field matching efficiency and Black: total aperture efficiency. In (a), quarter wavelength matching layers are considered at all surfaces, while in (b) wideband matching layers are considered at all surfaces.

To analyse the scanning performance of this geometry, one needs to choose the FO spheres that are going to be utilized, taking into account the applicability region discussed in section 4.2. Starting with the on-focus FO sphere, centred around $O_1 = (0,0)$, with a radius of $R_1 = F_{hb}$ and $\theta_1 = \theta_{trun}^{hb}$ and accepting maximum errors of $\varepsilon = 0.2, \varepsilon_\varphi = \pi/8$, an applicability region equal to $D_{FO}^1 = 6.95\lambda_0 F_{hb}/D_{hb}$ is derived, meaning that this sphere gives accurate results for the analysis of the central element of the FPA, as well as ± 1 lens element ($D_{lens} = 2.12\lambda_0 F_{hb}/D_{hb}$) around it. To extend the analysis to more array elements, off-focus FO spheres should be employed. Since the GO fields on the FO sphere are calculated using numerical GO propagation, as in Eq. 4.4, the displacement of the FO sphere has no impact on the speed or complexity of the calculation. Therefore, to keep the analysis generic, the FO sphere is displaced every time such that it is centred around the examined feeding lens. This way, the analysis can be more generic and accurate. For a focal plane array with ± 6 elements, the ray picture for three indicative examples is presented in Figure 4-10, together with the FO spheres utilized. The scan loss associated to this array configuration is shown in Figure 4-11 and the effect in accuracy of the FO sphere choice is further discussed in subsection 4.5.2.
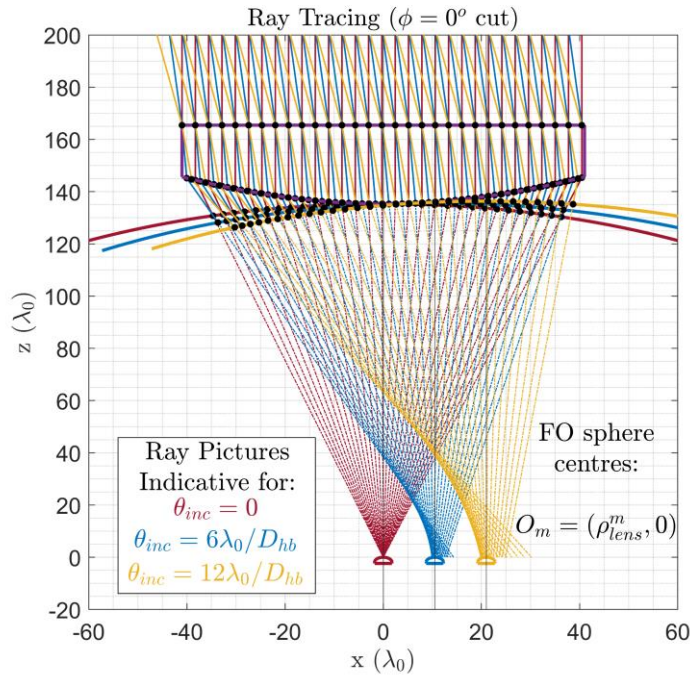
Figure 4-10. Ray picture for plane wave incidence from $\theta_{inc} = (0,6,12)\lambda_0/D_{hb}$. The FO spheres utilized for each case are also illustrated.
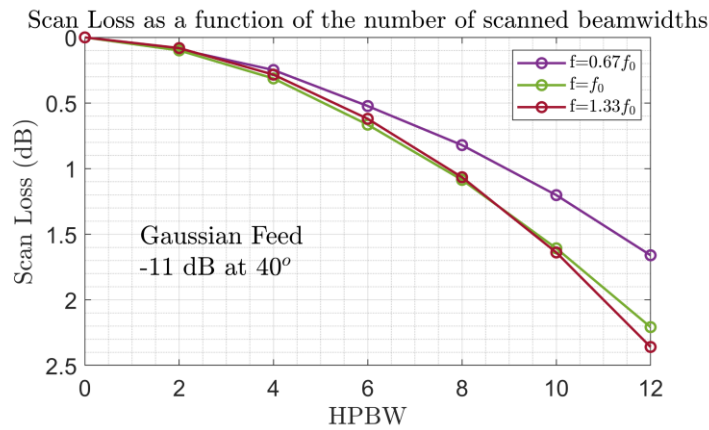
Figure 4-11. Scan Loss of Geometry II (Figure 4-7, Table 5), fed by a Gaussian feed, as a function of the scan angle, for different frequencies, within a bandwidth of 1:2.

4.5.2. Validation using Physical Optics

To validate the CFO analysis methodology, the resulting efficiency curves are compared to the ones derived by analysing the same geometry with a combination of PO for the propagation between the elliptical and the hyperbolic lens and GO for the propagation inside the hyperbolic lens. The accuracy of the GO propagation inside the hyperbolic lens has already been validated in section 3.5.2. To verify the accuracy of the CFO technique, as well as to evaluate the FO sphere applicability region as discussed in the previous section, the aperture efficiency for three frequency points within an 1:2 bandwidth, as a function of the half-power beamwidths scanned in a certain direction, is used for the comparison (Figure 4-12).
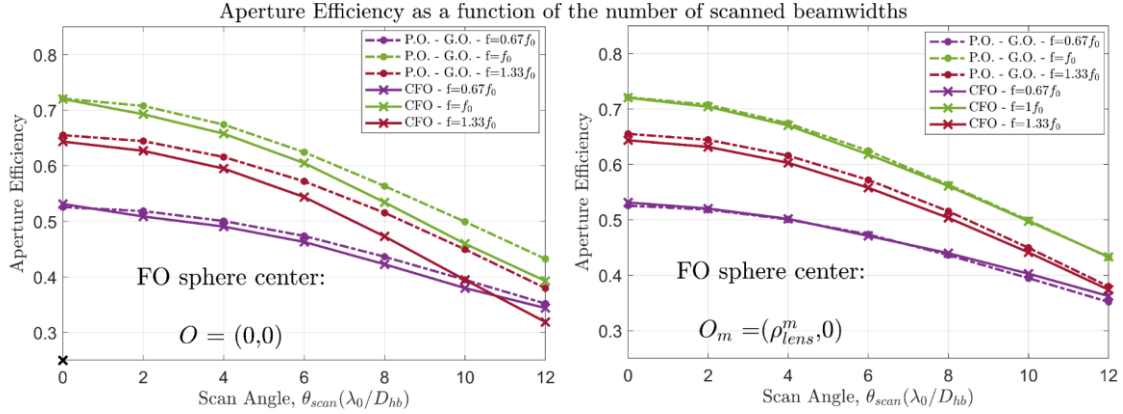
Figure 4-12. Aperture Efficiency of Geometry II (Figure 4-7, Table 5), fed by a Gaussian feed, as a function of the scan angle, for different frequencies, within a bandwidth of 1:2. The results of the CFO technique are compared with a PO-GO technique. In (a) the on-focus FO sphere is used, while in (b) off-focus FO-spheres are employed for the analysis of different FPA elements.

From Figure 4-12 it can be inferred that without the use of the off-focus FO spheres, the accuracy of the CFO methodology is degraded, especially at the higher frequencies, where the applicability region is smaller (Eq. 4.5). On the contrary, when using the off-focus FO spheres, the resulting efficiencies are in very good agreement with the ones derived through the PO-GO methodology.

4.6. Design based on a Tapered Leaky-Wave Slot Feeding Element

Similar to the design of the real feeding element for the first examined geometry in section 3.6, the desired properties of the primary pattern can be deduced through the analysis of the Gaussian-fed architecture. Contrary to the geometrically coupled system, the diffractively coupled focusing system of a small focal lens (elliptical in this case) and a hyperbolic lens features an inherent frequency dependency, due to the frequency dependency of the focal field. This means that to achieve the field matching condition throughout the whole frequency band, the field transmitted through the elliptical lens should also feature a frequency dependency and more specifically an increase in directivity with frequency. To achieve this, a resonant feeding element, with wideband impedance matching capabilities is required.

To ensure the wideband impedance matching, a tapered leaky-wave slot, as the one shown in Figure 3-17 is utilized and the parameters of the geometry are tweaked such as the feed directivity is increased with frequency. It is noted that although there are inherent limitations in the performance that can be achieved by this feeding element due to the properties of the current distribution and the stratification, a more frequency dependent performance can be achieved, as shown in Figure 4-13, with the parameters given in Table 6.
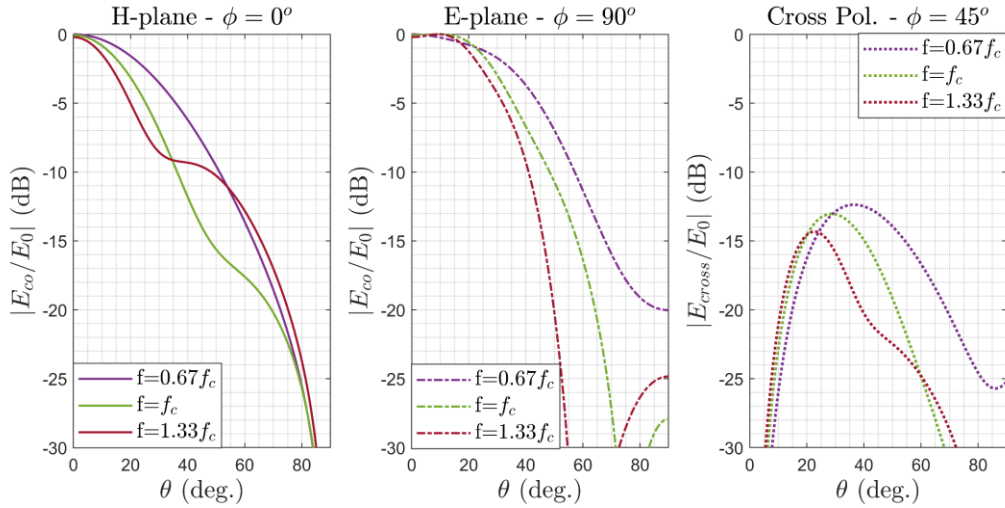
Figure 4-13. Primary patterns of the feeding element described in Table 6 throughout a frequency band of 1:2.

Table 6. Parameters of Final Design of an elliptical lens diffractively coupled to a hyperbolic lens

Tapered leaky wave slot		Hyper-hemispherical Lens		Hyperbolic Lens	
Slot Length L_a	$0.4\lambda_0$	Permittivity ε_r^{hh}	11.9	Permittivity ε_r^{hb}	2.4
Cavity height h_{gap}	$0.016\lambda_0$	Diameter D_{hh}	$3.5\lambda_0$	Diameter D_{hb}	$82\lambda_0$
Tapering Angle γ	35°	Truncation Angle θ_{trun}	52°	F-number $f_{hb}^{\#}$	1.65
Phase Centre Position (from the ground plane)	$-0.72\lambda_0$			Thickness h_{hb}	$19.8\lambda_0$
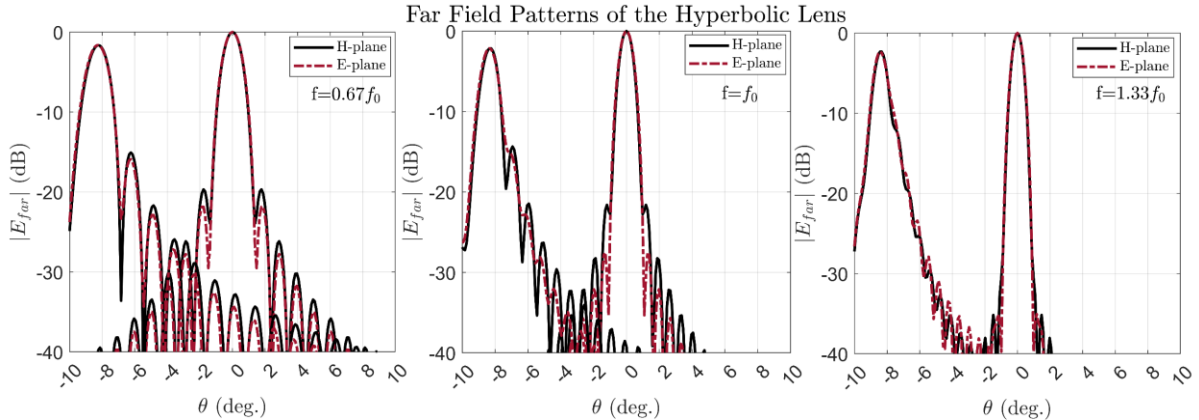
Figure 4-14. Far field pattern of the lens chain of Geometry II, fed by a Tapered Leaky Wave Slot (Table 6), at three frequencies within a 1:2 bandwidth, for broadside and scanning to $\theta_{scan} = 12\lambda_0/D_{hb}$.

As observed from Figure 4-13, the directivity of the primary pattern is increased with frequency, especially in the E-plane. In the H-plane, as the frequency is increased, the slot becomes electrically larger, rendering the effect of the so-called slot mode [28] more dominant, which in turn reduces the enhancement of its directivity. The resulting efficiencies are then shown in Figure 4-15. It is noted that the inherent frequency dependency of the diffractively coupled system does not allow for a more frequency independent behaviour of the system, as also indicated by the QO system radiation efficiency term (Eq. 4.7, shown in red in Figure 4-15), which is independent of the feeding element of the elliptical lens and thus posses an upper limit on the performance that can be achieved by this quasi-optical system. As for the feeding element, although the non-ideal properties of the leaky-wave feed could also add a frequency dependency, this is counteracted as much as possible by its proper design, as discussed earlier in this section.

(a) Quarter wavelength matching layers at f_c (b) Ideal Wideband matching layers
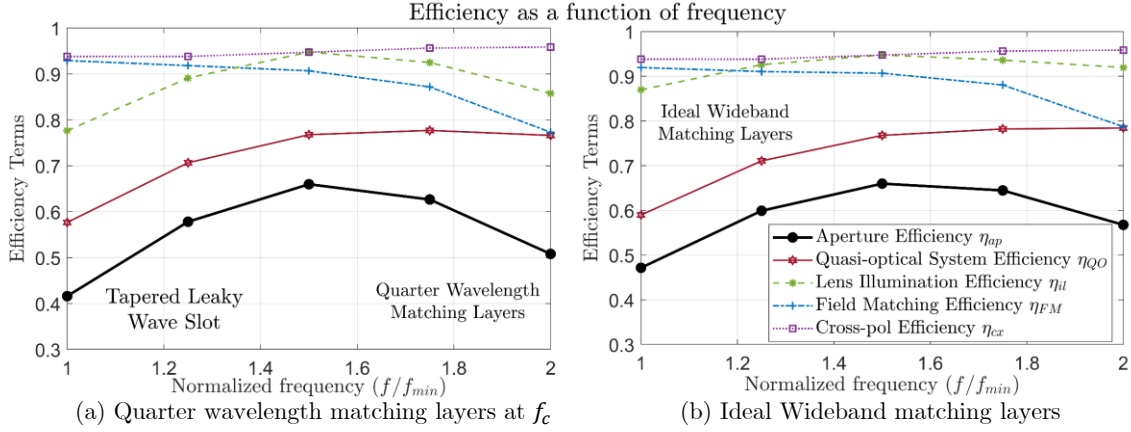
Figure 4-15. Efficiency terms for the geometry of Figure 3-1, fed by a Tapered leaky wave slot. Green: illumination efficiency of the hyper-hemispherical lens, Red: quasi-optical system radiation efficiency, Blue: field matching efficiency and Black: total aperture efficiency. In (a), quarter wavelength matching layers are considered at all surfaces, while in (b) wideband matching layers are considered at all surfaces.
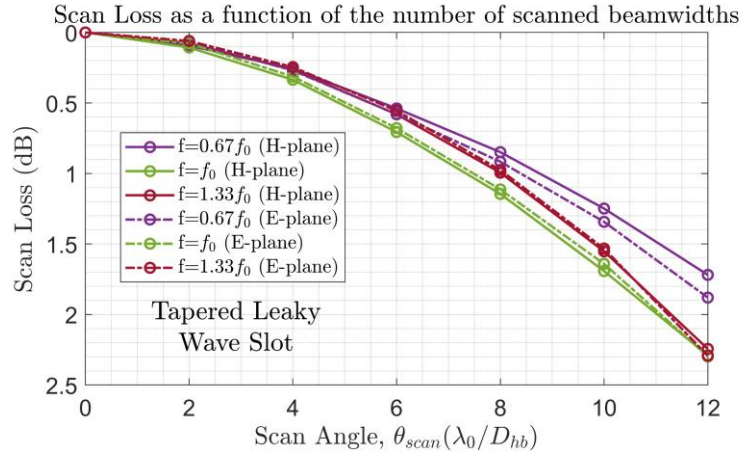
Figure 4-16. Scan Loss of Geometry II (Figure 4-7, Table 5), fed by a Tapered leaky wave slot, as a function of the scan angle, for different frequencies, within a bandwidth of 1:2. Solid lines are for scanning in the H-plane ($\varphi = 0^o$), while dashed lines correspond to scanning in the E-plane ($\varphi = 90^o$).

Overall, the geometry discussed in the current chapter features a more frequency dependent broadside aperture efficiency compared to the design of Chapter 3, arising from the diffractive coupling between the quasi-optical components, as well as the matching layers. Although the feeding element is designed such that it partly counteracts this frequency dependency of the quasi-optical system, still the response depends on frequency, due to the coupling and inherent limitations of the feed. As for the scanning performance, this geometry features a much better performance than the one of the geometry of Chapter 3, due to the positioning of the feeding elements closer to the actual focal plane of the hyperbolic lens.

4.7. Feed Displacement to Improve the Scanning Performance

Although the diffractively coupled system discussed in this chapter performs well in terms of scanning, compared to the previously examined architecture (Chapter 3, Geometrically coupled system of a hyperbolic and a hyper-hemispherical lens), this performance can be further improved without increasing the complexity of the design. In particular, based on the analysis performed in [19], one can optimize the design of the lens feeders by examining the properties

of the focal field, through the CFO spectrum of Eq. 2.18. In [19], the elements of a large format FPA are divided into regions, depending on the dominant source of scan loss. For elements not very far off the focus of the focusing component, like the ones examined in this work, the CFO field has a dominating linear phase term, indicating that a lateral displacement of the feed inside the lens could improve the field matching between the fields in reception and in transmission ($\vec{E}_l^{Rx}, \vec{E}_l^{Tx}$, Eq. 2.20-2.21, Figure 4-1). The lateral displacement is towards the direction of scanning and in this case is performed for elements scanning at $\theta_{scan} \geq 6\lambda_0/D_{hb}$ (below that the scan loss is already below 0.5 dB). For the geometry described in Table 6, the optimal displacements are given in Table 7. The scan loss before and after applying the displacement is presented in Figure 4-17, while the phase matching improvement for scanning at $N = 12$ beams is shown in Figure 4-18.

Table 7. Displacement of the feeding elements inside the elliptical lenses of Geometry II (Table 6)

Scan Angle (λ_0/D_{hb})	0	2	4	6	8	10	12
Feed displacement ($\Delta\rho_{feed}$)	0	0	0	$0.027\lambda_0$	$0.034\lambda_0$	$0.04\lambda_0$	$0.045\lambda_0$
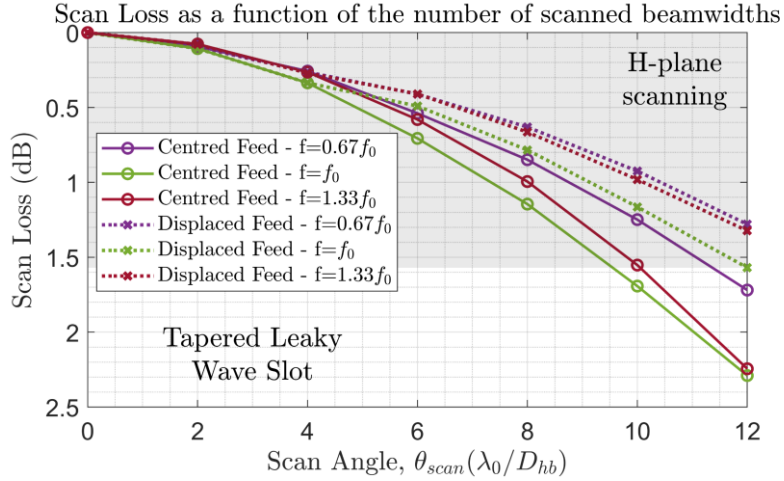
Figure 4-17. Scan Loss for Geometry II (Figure 4-7, Table 5), fed by a Tapered leaky wave slot, as a function of the scan angle, for different frequencies, within a bandwidth of 1:2. Solid lines are for the feeding elements positioned at the centre of the respective elliptical lens, while dashed lines are for displaced feeding elements towards the direction of scanning (H-plane in this case).
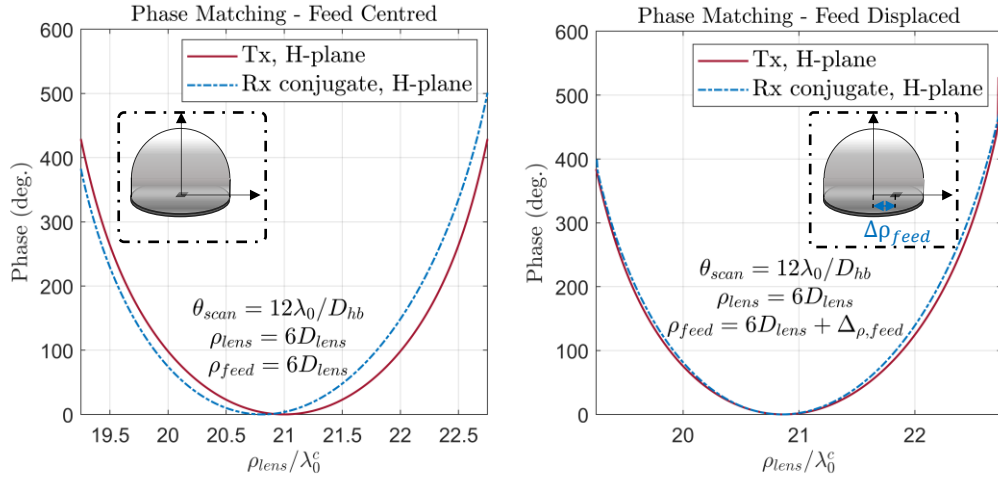
Figure 4-18. Phase matching on top of the elliptical lens, between the coherently summed plane wave spectrum in reception (Eq. 2.20) and the field transmitted out of the lens in transmission (Eq. 2.21). The phase matching is shown before and after displacing the feeding element inside the lens, for scanning at $\theta_{scan} = 12\lambda_0/D_{hb}$.

Having discussed the potential of both proposed architectures, in Chapter 5, the specific astronomical surveys of the TIFUUN project will be discussed and the systems analyzed in Chapter 3 and Chapter 4 will be adjusted to these science cases. To enable this, a comparison between the two architectures will also be presented in this section 5.1.

Chapter 5.
TIFUUN Science Cases and Proposed Architectures

TIFUUN's main target is to produce 3D maps of star-forming galaxies, cold interstellar matter (ISM) and young galaxy clusters. To achieve this, four types of observations are targeted and each of them is facilitated by one or more IFU designs. Firstly, TIFUUN aims on detecting bright emission lines, shifted to the mm-submm (0.8-3mm) wavelength regime. The prominent cooling line of the interstellar matter in dusty star-forming galaxies (DSFGs) is the [CII] line, able to probe star-formation at redshift (Eq. 1.1) $z > 4.4$, [29]. Thus, the first survey targets the detection of this line to probe dusty star-forming galaxies (***DSFG survey***). Subsequently, observations in the THz regime are ideal for complementing visible and near infrared (Vis-NIR) surveys, since dusty regions are invisible in Vis-NIR frequencies, while Terahertz emission lines are unattenuated by dust, rendering dust-obscured galaxies detectable (***Terahertz Line Emitting Galaxies (TLEG)*** [C_{II}] ***Tomography***). To add on this, TIFUUN equipped with medium spectral resolution IFUs can potentially trace the total 3D history of star formation over large cosmic volumes, without the need of detecting individual galaxies. The technique to achieve this is called ***Line Intensity Mapping (LIM)***. Finally, using the ***Sunyaev-Zeldovich (SZ)*** effect [30], TIFUUN equipped with a low spectral-resolution IFU can map the hot matter in galaxy clusters.

To summarize, the TIFUUN project will be developed to perform a set of astronomical surveys, with its main goal being the detection of star-forming galaxies and the exploration of the evolution of the Universe, using novel techniques of probing cold and hot ISM. To achieve these science goals, a number of IFUs, namely DSFG, SZ, TLEG and LIM, are planned to be developed. To facilitate the design, some of the astronomical surveys (DSFG and SZ) are divided into the fabrication of two IFU-wafers, each featuring a bandwidth of at most 1:2. Due to the "Plug-and-Play" compatibility, the two bands of the same survey can observe simultaneously the same sky field. Some of the specifications of the TIFUUN IFUs are summarized in Table 8.

Table 8. Specifications of the TIFUUN IFUs, for each of the science goals.

IFU Type	Frequency Band	Spectral Resolution / Spectral Channels per spatial pixel
DSFG Band 1	90 – 180 GHz	High / ~693 channels
DSFG Band 2	180 – 360 GHz	High / ~693 channels
SZ Band 1	100 – 175 GHz	Low / ~7 channels
SZ Band 2	200 – 355 GHz	Low / ~7 channels
TLEG [*CII*] *Tomography*	210 – 230 GHz 260 – 280 GHz 328 – 353 GHz	Medium / ~62 channels
LIM	200 – 370 GHz	Medium / ~62 channels

Taking into account the requirements of the different IFUs, as well as the field of view of the ASTE telescope, one can evaluate which architecture is more suitable for each IFU. The first aspect one should take into account is the number of beams required to fill the field of view of a telescope. The number of beams per plane can be estimated by simply dividing the field of view with the half power beamwidth of the antenna. For large antennas the half power beamwidth is approximately λ_0/D and thus the number of beams required per plane is given through Eq. 5.1, as also illustrated in Figure 5-1.
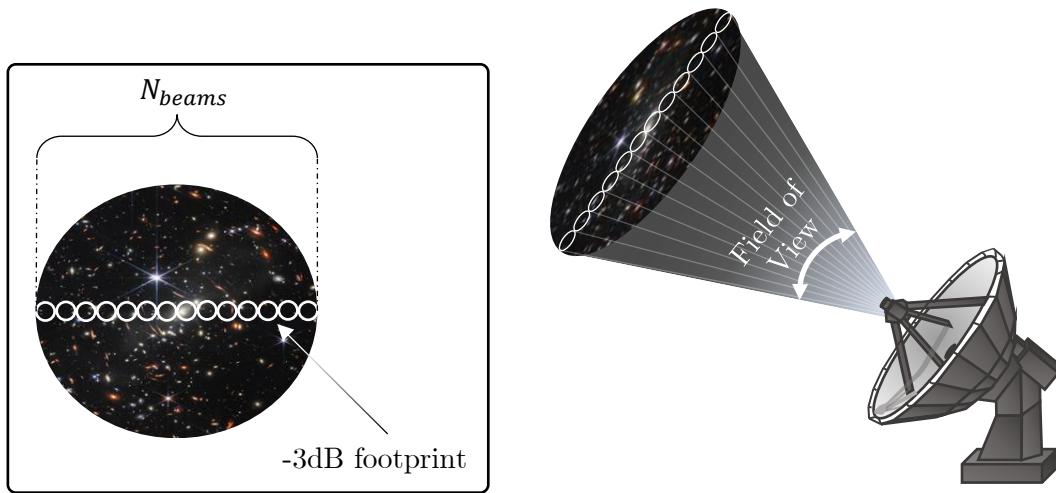
Figure 5-1. Field of view of a telescope. In the inset, the definition of the number of beams required to cover the FoV in one plane is illustrated.

$$N_{beams} \cong \frac{FoV_{ASTE}}{\left(\frac{\lambda}{D_{ASTE}}\right)}, \tag{5.1}$$

To design a focal plane array for each of the science cases presented in Table 8, except for the number of beams required to cover the field of view, one is also limited by the total number of detectors in the system, as expressed in Eq. 1.2. For instance, the DSFG survey requires high spectral resolution, limiting the number of antennas that can be utilized. Furthermore, depending on the frequency range in which the system operates, the number of beams required to cover the FoV is different.

Having discussed the targeted astronomical surveys of the TIFUUN instrument, in the following subsections (5.2 and 5.3), the surveys are divided into two categories, depending on the spectral resolution of the IFUs. In particular, low-medium spectral resolution IFUs are not limited by the number of detectors that can be hosted by the IFU and thus they can cover large part of the field of view of the telescope instantaneously. On the other hand, the number of antennas in high resolution IFUs is limited by the total number of detectors.

To facilitate the choice of the optimal architecture for each of these categories, the candidate geometries presented in Chapter 3 and Chapter 4 are compared in terms of their performance both as single element architectures and in an array configuration.

5.1. Comparison between the two architectures

To compare the geometries of Chapter 3 and Chapter 4 as single element architectures, the broadside aperture efficiency, is presented in Figure 5-2. To also evaluate the scanning performance of the two geometries, the aperture efficiencies of adjacent elements of the focal plane arrays are plotted as a function of the scan angle in the same figure. Although after shaping the lens surfaces, the scanning performance of Geometry I is significantly improved, allowing it to perform better than Geometry II for small angles as well, the sampling of the image plane is still limited by the physical size of the feeding element. This is represented in the aperture efficiency plots through the markers, corresponding to the scanning performance of each array element.
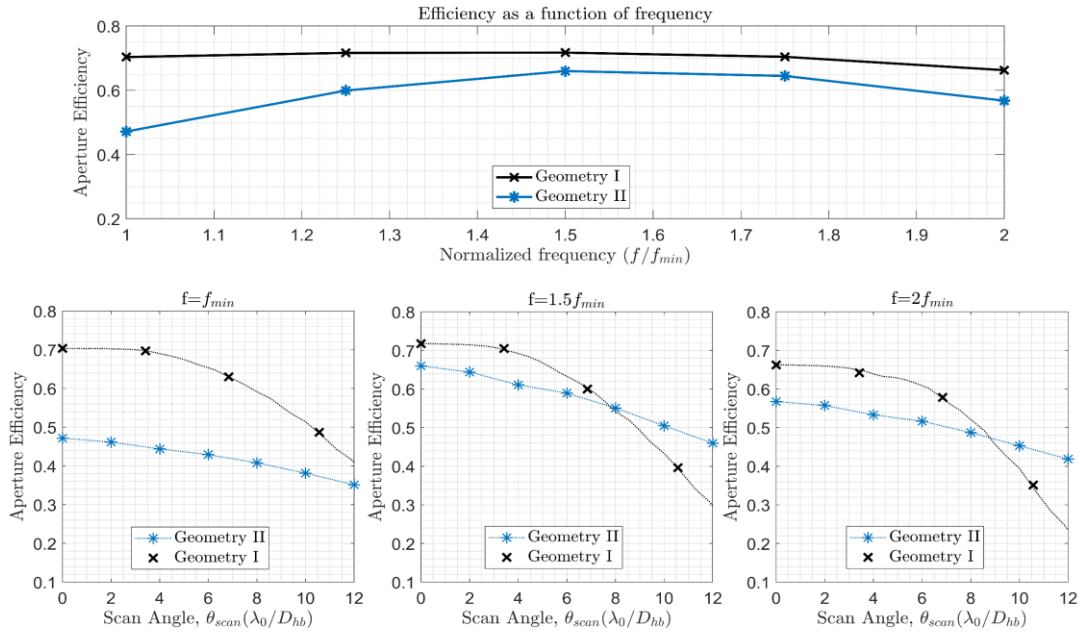
Figure 5-2. Comparison between Geometry I (with the parameters of Table 2 and Table 3) and Geometry II (with the parameters of Table 6 and Table 7). On the top figure, the broadside aperture efficiencies are plotted as a function of frequency (assuming ideal wideband matching layers) and on the bottom figures the aperture efficiencies are plotted as a function of the scan angle, for three frequency points within a bandwidth of 1:2.

To conclude, the geometrically coupled system performs better in a single element configuration, as well as for small scanning. However, it is not optimal for covering wide fields of view instantaneously, since the sampling of the image plane is sparse and thus the scan loss is significantly increased as the size of the array increases. The diffractively coupled system on the other hand features a lower and more frequency dependent efficiency for broadside, but it performs very well in an array configuration, since it allows for dense sampling of the field of view with low scan loss.

Taking into account the potential of each proposed architecture, an indicative geometry is suggested for each of the IFU categories discussed in the introductory part of this chapter, i.e. low-medium and high spectral resolution IFUs.

5.2. Low-Medium Spectral Resolution IFUs

For low-medium spectral resolution IFUs, the number of antennas forming the focal plane array is mostly determined by the field of view of the telescope, in combination with the frequency range of operation. To examine the science cases presented in Table 8, one can analyse two indicative frequency bands, around 137.5 GHz (referred to as low frequency) and around 277.5 GHz (referred to as high frequency), with bandwidths of operation of 1:2. For the low frequency band, the number of beams required to cover the field of view is around 10, while for the high frequency band around 21. It is noted that the Field of View of the ASTE telescope is $FoV_{ASTE} = 7.5 \ arcmin \ (0.125^o)$, while its diameter is equal to 10m.

As already discussed in section 5.1, the diffractively coupled system discussed in Chapter 4 (hyperbolic lens coupled to an array of elliptical lenses) is more fitting for surveys that need to cover a wide field of view instantaneously. Thus, with a sampling condition of $\Delta\theta = 2\lambda_0/D_{hb}$ in the image plane ($\Delta\rho_{lens} = 2.12\lambda_0 F_{hb}/D_{hb}$) and with a hexagonal lattice, the coverage of the

ASTE field of view requires an array of 19 lenses for the low frequency array and 91 lenses for the high frequency one. Setting an indicative diameter for the hyperbolic lens equal to 10cm, the two arrays are presented in Figure 5-3 (high frequency) and Figure 5-4 (low frequency). The parameters for the two designs are given in Table 9. It is noted that since the hyperbolic lens diameter is altered, the feed displacements inside the lenses is also altered, as shown in Table 10 and Table 11 for the high and low frequency architectures respectively.

To showcase the achieved efficiencies with these architectures, the aperture efficiency for broadside, as well as the aperture efficiency of the edge element of the FPA is shown in the top of Figure 5-5 and Figure 5-6. In the same figures, the -3dB footprint of the beams created by each FPA in the image plane is also depicted, both after one telescope pointing, and after four pointings, when the full field of view is sampled. In the -3dB footprint, a half power beamwidth of λ/D is assumed.

Table 9. Parameters of the designs presented in Figure 5-3 and Figure 5-4.

Tapered leaky wave slot		Hyper-hemispherical Lens		Hyperbolic Lens		
					f_{high}	f_{low}
Slot Length L_a	$0.4\lambda_0$	Permittivity ε_r^{hh}	11.9	Permittivity ε_r^{hb}	2.4	2.4
Cavity height h_{gap}	$0.016\lambda_0$	Diameter D_{hh}	$3.5\lambda_0$	Diameter D_{hb}	$92.5\lambda_0$	$45.83\lambda_0$
Tapering Angle γ	35°	Truncation Angle θ_{trun}	52°	F-number $f_{hb}^{\#}$	1.65	1.65
Phase Centre Position (from the ground plane)	$-0.72\lambda_0$			Thickness h_{hb}	$23.37\lambda_0$	$11.08\lambda_0$
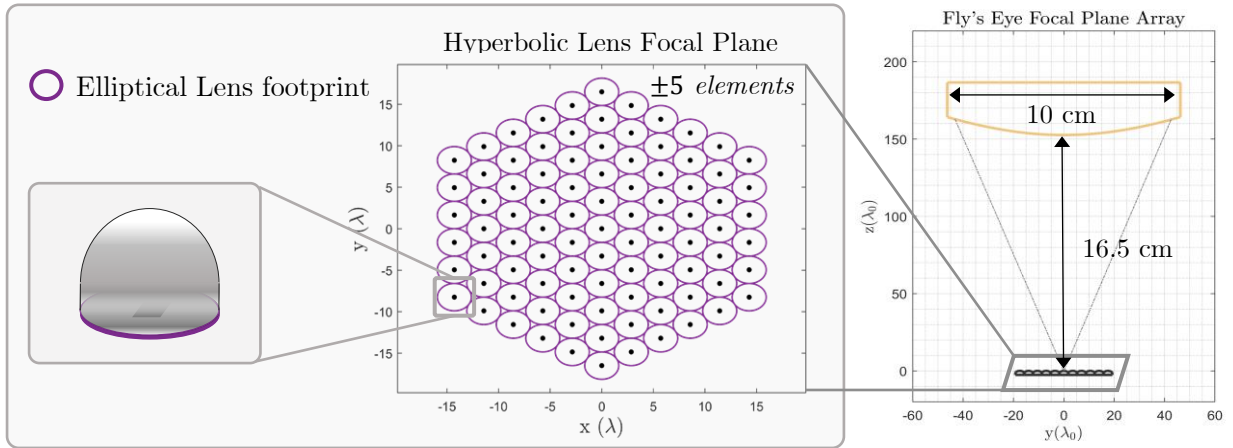
Figure 5-3. Focal plane array of 91 elliptical lenses of diameter $D_{lens} = 2.12\lambda_0 F_{hb}/D_{hb}$, in a hexagonal lattice, diffractively coupled to a 10cm diameter hyperbolic lens ($F_{hb}/D_{hb} = 1.65$), at a frequency of 277.5GHz.
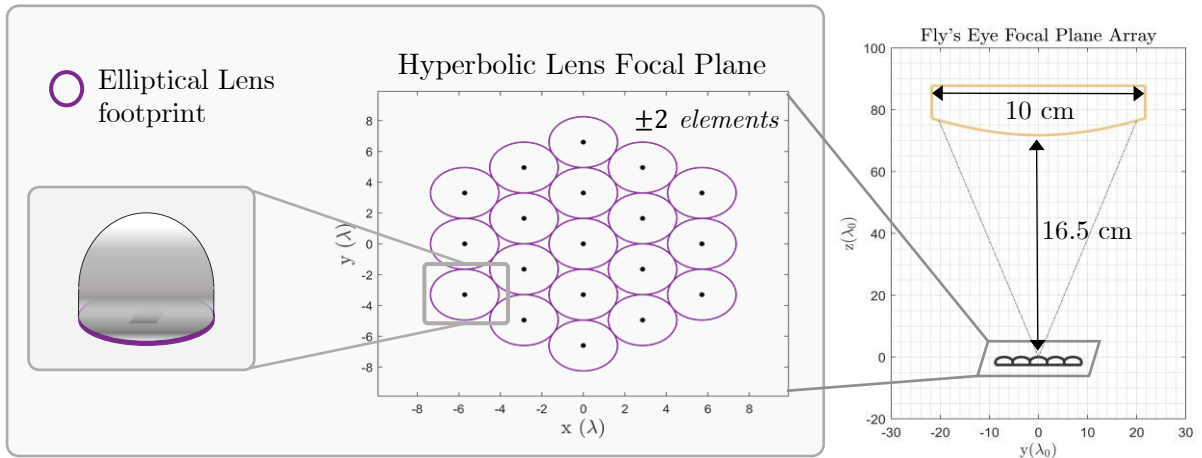
Figure 5-4. Focal plane array of 19 elliptical lenses of diameter $D_{lens} = 2.12\lambda_0 F_{hb}/D_{hb}$, in a hexagonal lattice, diffractively coupled to a 10cm diameter hyperbolic lens ($F_{hb}/D_{hb} = 1.65$), at a frequency of 137.5GHz.
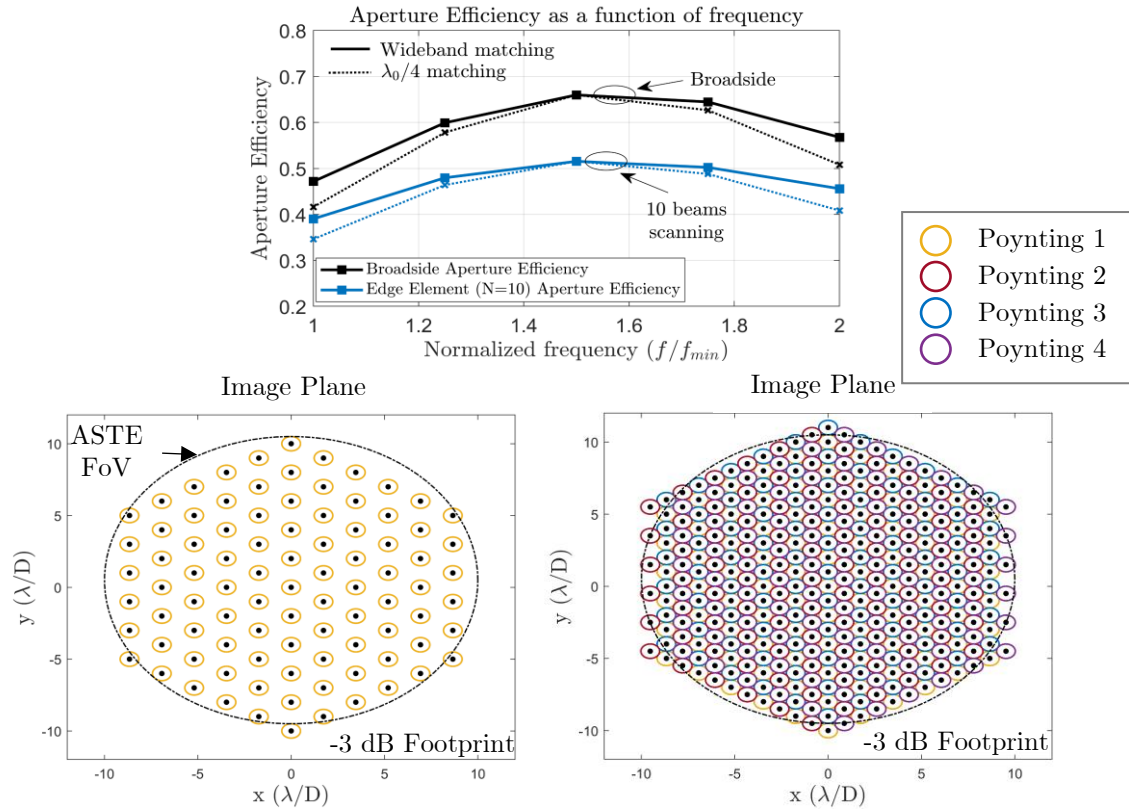
Figure 5-5. Aperture Efficiency for the broadside element and the edge element of the FPA of Figure 5-3 (top) and -3dB footprint of the beams created by the same FPA in the image plane after one telescope pointing (bottom left) and 4 telescope pointings (bottom right), assuming $HPBW = \lambda/D$.
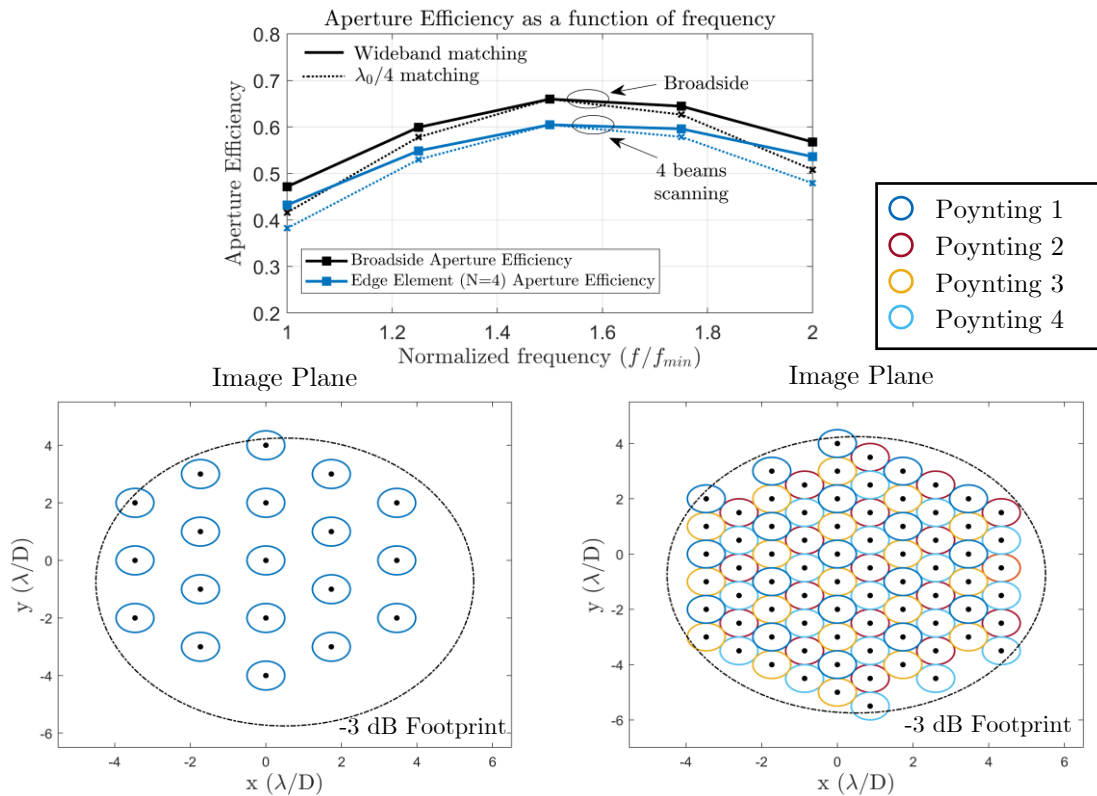
Figure 5-6. Aperture Efficiency for the broadside element and the edge element of the FPA of Figure 5-4 (top) and -3dB footprint of the beams created by the same FPA in the image plane after one telescope pointing (bottom left) and 4 telescope pointings (bottom right), assuming $HPBW = \lambda/D$.

Table 10. Displacement of the feeding elements inside the elliptical lenses of the geometry of Figure 5-3.

Scan Angle (λ_0/D_{hb})	0	2	4	6	8	10
Feed displacement $(\Delta\rho_{feed})$	0	0	0	$0.024\lambda_0$	$0.03\lambda_0$	$0.035\lambda_0$

Table 11. Displacement of the feeding elements inside the elliptical lenses of the geometry of Figure 5-4.

Scan Angle (λ_0/D_{hb})	0	2	4
Feed displacement $(\Delta\rho_{feed})$	0	0	$0.035\lambda_0$

5.2.1. Scalability of the proposed architectures

An important aspect in the design phase that has not been discussed so far, concerns the scalability of the discussed architectures in terms of their physical dimensions. In particular, to get from the presented results to the final design, one should take into account more parameters that are not discussed throughout this thesis, such as the available space after the polarizing grid, the thickness of the hyperbolic lens and the diameter of the wafer. This means that the actual physical dimensions of the utilized architectures are not yet defined and the presented results are indicative to showcase the potential of the geometries. For this reason, it is interesting to also examine the effect of the scanning performance if the diameter of the hyperbolic lens is decreased, without altering the f-number of this design, which has been chosen in Chapter 4 to achieve an optimal performance.

An important tool that allows us to decrease the diameter without much loss in the scanning performance is the feed displacement inside the lenses to correct for phase aberrations while scanning, as discussed in section 4.7. In Figure 5-7 and Figure 5-8, four different diameters of the hyperbolic lens/focal distance are examined, keeping the f-number constant. Each figure corresponds to the high and low frequency examples presented in the rest of this section. In (a), the aperture efficiency as a function of frequency is presented for these diameters/focal distances, while in (b), the scan loss is plotted as a function of the hyperbolic lens diameter and focal distance (bottom and top horizontal axis respectively). To also showcase the impact of the feed displacement, the scan loss is presented with and without displacing the feeding elements inside the lenses.

Overall, it can be observed that excess scan loss can be significantly compensated if the feeds are properly displaced inside the lenses. Also, the smaller the diameter of the hyperbolic lens (i.e. the closer the edge element to the rim of the hyperbolic lens), the larger is the impact of the feed displacement.

(a) Aperture Efficiency as a function of frequency

(b) Scan loss as a function of the hyperbolic lens diameter/focal distance
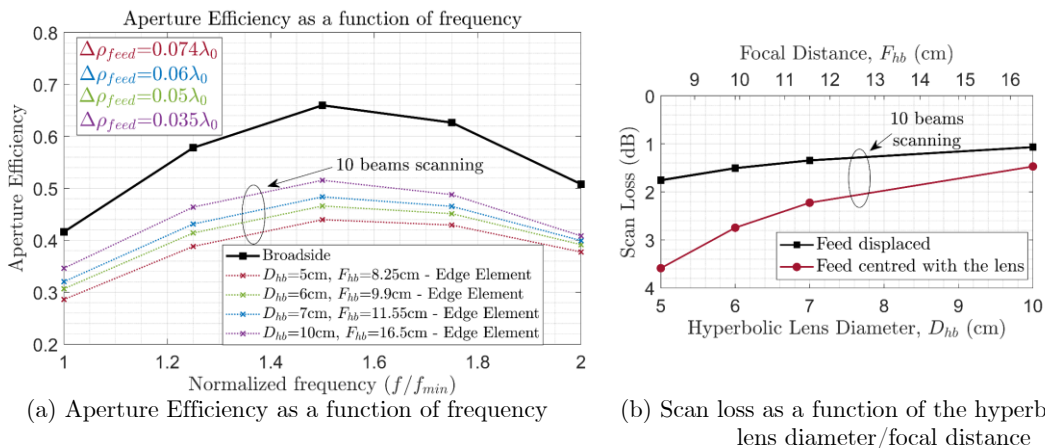
Figure 5-7. Dependency of the aperture efficiency and scan loss from the hyperbolic lens diameter, keeping the f-number constant ($F_{hb}/D_{hb} = 1.65$). In (a) the aperture efficiency for broadside and the edge element (10 beams scanning, at 277.5GHz) is shown, after displacing the feeds appropriately inside the respective lenses ($D_{lens} = 2.12\lambda_0 F_{hb}/D_{hb}$), while in (b) the scan loss as a function of the hyperbolic lens diameter/focal distance is showcased before and after displacing the feeds, at the central frequency. In all surfaces, quarter wavelength matching layers are assumed.

(a) Aperture Efficiency as a function of frequency

(b) Scan loss as a function of the hyperbolic lens diameter/focal distance
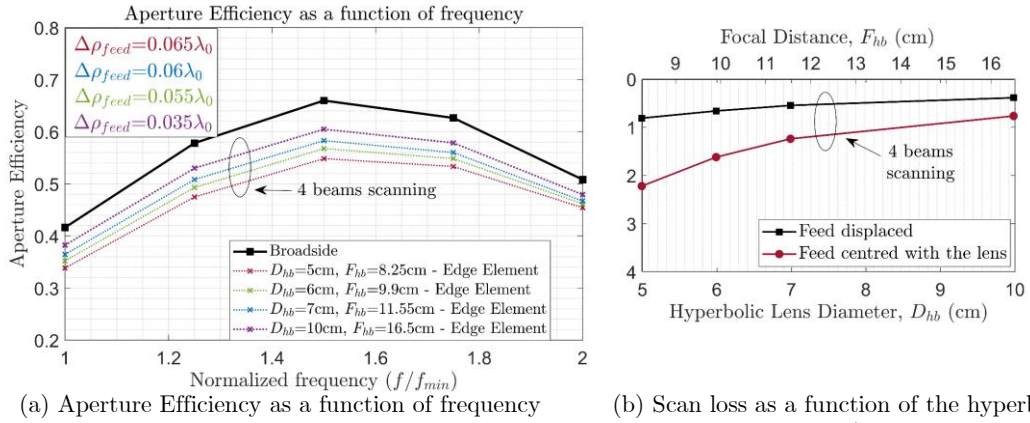
Figure 5-8. Dependency of the aperture efficiency and scan loss from the hyperbolic lens diameter, keeping the f-number constant ($F_{hb}/D_{hb} = 1.65$). In (a) the aperture efficiency for broadside and the edge element (4 beams scanning, at 137.5GHz) is shown, after displacing the feeds appropriately inside the respective lenses ($D_{lens} = 2.12\lambda_0 F_{hb}/D_{hb}$), while in (b) the scan loss as a function of the hyperbolic lens diameter/focal distance is showcased before and after displacing the feeds, at the central frequency. In all surfaces, quarter wavelength matching layers are assumed.

5.3. High Spectral Resolution IFUs

For high spectral resolution IFUs, the number of antennas that can be utilized is mostly limited by the available number of detectors per IFU (Eq. 1.2, $N_{ant} = N_{det}/N_{ch}$). Therefore, it is inherently not possible to instantaneously cover a large part of the field of view, as in the cases of section 5.2. As a result, the geometrically coupled system described in Chapter 3 is ideal for such systems, since it features high aperture efficiency for broadside and small scanning angles.

In Figure 5-9, an array of 7 elements in a hexagonal lattice configuration, under a hyper-hemispherical silicon lens, geometrically coupled to a plastic hyperbolic lens, is shown.
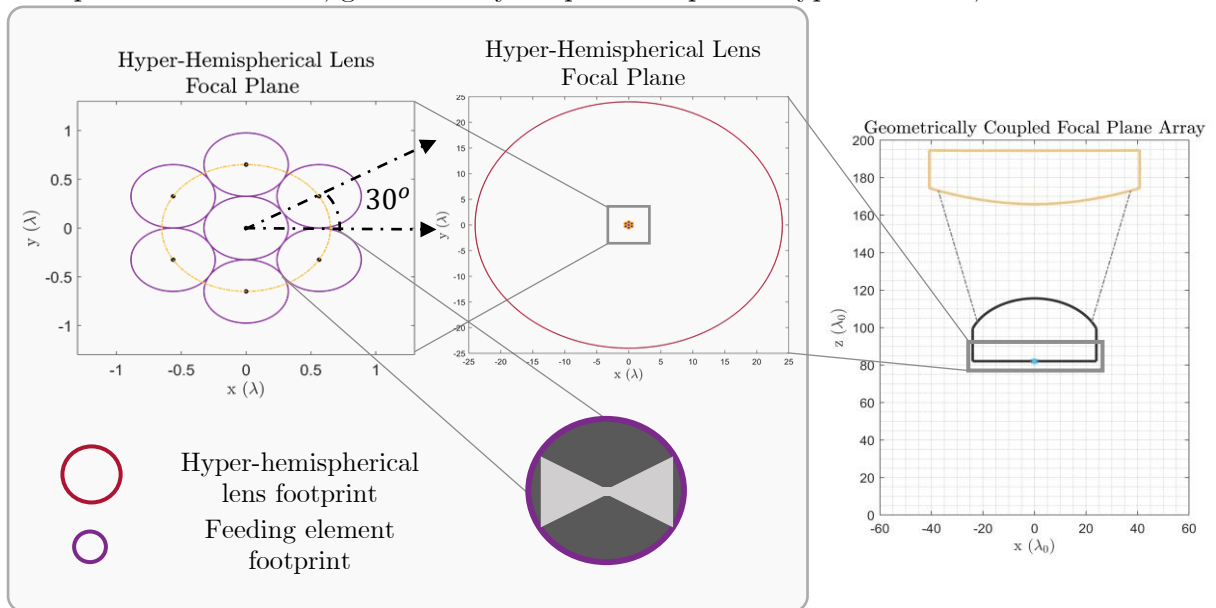
Figure 5-9. Focal plane array of 7 feeding elements in a hexagonal lattice, inside a hyper-hemispherical lens, geometrically coupled to a hyperbolic lens.

The efficiency terms of the broadside, as well as the edge elements are then shown in Figure 5-10, both with and without shaping the respective surfaces. For the non-shaped case, the parameters of the feed and lenses are given in Table 2, while after the shaping, the feeding elements remain the same, while the geometrical parameters of the lenses are given in Table 3. It should be noted that, as also discussed in section 3.6, the physical dimensions of the feeding element limit the sampling in the image plane, creating a sparse sampling, as shown in Figure 5-11.
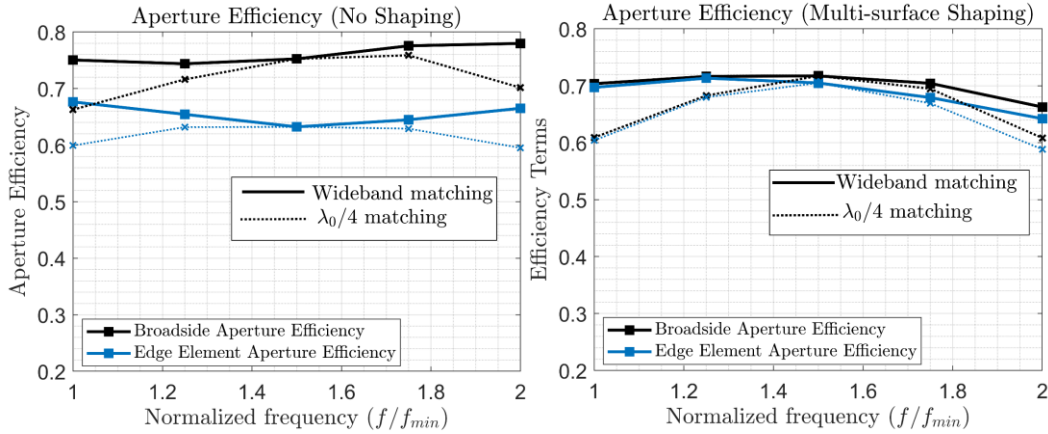
Figure 5-10. Aperture Efficiency for the broadside element and the edge element of the FPA of Figure 5-9, without shaping (left figure) and with the shaping parameters of Table 3 (right figure).
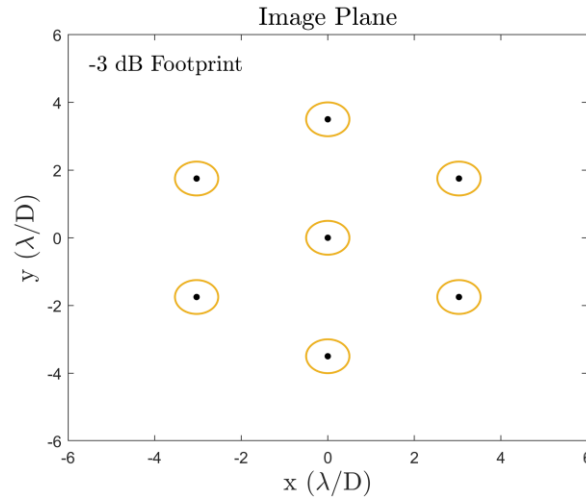
Figure 5-11. -3dB footprint of the beams created by the FPA of Figure 5-9 in the image plane after one telescope pointing, assuming $HPBW = \lambda/D$.

The physical dimensions of this geometry highly depend on the frequency of operation. If this system is decided to be used in the TIFUUN instrument for low frequencies, the dimensions of this architecture, as presented in Chapter 3, as well as in the current section, become prohibiting for use in the available space inside the cryostat. To decrease these dimensions, while retaining the performance, further research is required. A valuable tool for such research is the shaping of the dielectric lenses, since it can significantly improve the scanning performance.

Chapter 6.
Conclusions & Future Work

6.1. Conclusions

In this work, design guidelines for part of the quasi-optical system coupling the radiation from the ASTE telescope to the spectrometer array of the TIFUUN system are presented. In particular, two different approaches are introduced for the design of part of the cold optics, as well as of the focal plane array of antennas feeding the detectors.

The motivation behind the TIFUUN project is firstly described, which is then followed by a discussion about the requirements of the system. This leads to the definition of some initial guidelines about the design approach from the point of view of the antenna design. In particular, to achieve the "Plug and Play" functionality targeted by TIFUUN, the building block of each IFU should be comprised of not only an array of antennas and spectrometers, but also a focusing component, in this case a plano-hyperbolic lens. Since TIFUUN includes multiple IFUs with different requirements in terms of bandwidth and field of view, two different design approaches are explored, as candidate geometries for this system. Each geometry achieves a different trade-off between bandwidth and scanning performance, providing the option to optimize one IFU based on its own requirements and independently from the others. Prior to the discussion about the candidate geometries, the theoretical background regarding the methodologies utilized for the analysis of the examined quasi-optical systems is presented. The main focus is in the difference between diffractive and geometrical coupling of quasi-optical components and the techniques that can be employed for their accurate and time-efficient analysis. Those are, a combination of geometrical optics (GO) propagation and analysis in reception for geometrically coupled lens systems and Coherent Fourier Optics (CFO) when a lens array is placed close to the focal point of a primary focusing component.

The first geometry examined is comprised of a plano-hyperbolic lens, geometrically coupled to a hyper-hemispherical lens, fed by a focal plane array of tapered leaky wave slots. The analysis of this candidate geometry is based on a combination of GO propagation and analysis in reception. Regarding its performance, it is found to feature a high and nearly frequency independent aperture efficiency as a single element architecture (74.5%-78%, neglecting the impact of the matching layer, within a 1:2 bandwidth), but its scanning performance is intrinsically limited. To compensate for that, a multi-surface symmetrical shaping is applied on the lens surfaces, at the cost of reducing the aperture efficiency of the central element (66%-72%, neglecting the impact of the matching layer, within a 1:2 bandwidth). Even though the shaping significantly improves the scanning performance (from 5.5dB to 2.5dB maximum scan loss in a bandwidth of 1:2 for scanning at ±10 beams), this architecture does not allow for a dense sampling of the image plane, leading to gaps in the field of view.

The second geometry is comprised of a plano-hyperbolic lens, diffractively coupled to a focal plane array of elliptical lenses. The feeding elements are tapered leaky wave slots. Since the elliptical lenses are positioned close to the focal point of the hyperbolic lens, to make the analysis of this geometry computationally efficient, a Coherent Fourier Optics methodology is employed. The performance of this structure is characterized by a more frequency dependent aperture efficiency, even when the feeding element is designed to partly counteract the inherent frequency dependency of the quasi-optical system. The scanning performance of this geometry is very good, achieving a scan loss of less than 2.5dB in a bandwidth of 1:2 for scanning at ±12 beams, with a hyperbolic lens of $82\lambda_0$ diameter as primary focusing component. This

scanning performance is further improved to a maximum of 1.6dB scan loss by laterally displacing the feeding elements inside the off-focus elliptical lenses.

In both geometries, the analysis is initially performed with an ideal feeding element, featuring a Gaussian-shaped far field. This allows us to examine the quasi-optical system independently from the frequency dependency of the real antenna as a first step and subsequently define the desired characteristics of the feeding element.

As a final step, the two examined architectures are specifically linked to science cases targeted by TIFUUN. In particular, the geometrically coupled lens chain features high and nearly frequency independent aperture efficiency for broadside and small scan angles. However, the allowed sampling of the image plane is sparse and the scanning performance is degraded for larger angular regions. Therefore, it is optimal for high spectral resolution IFUs, where the use of large format FPAs is already prohibited by the number of detectors hosted by the IFU. On the other hand, the diffractively coupled system features a very good scanning performance (low scan loss) and allows for denser sampling of the image plane, at the cost of an overall reduced efficiency, especially at the lower portion of the frequency bands of interest. This makes this geometry optimal for cases where the number of spatial pixels of the IFU is determined by the field of view of the telescope, and thus large format focal plane arrays are required.

6.2. Future Work

▪ The next stage of the TIFUUN quasi – optical system development concerns the final design of these building blocks, together with that of the quasi-optical chain coupling the radiation all the way from the ASTE telescope to the IFU building blocks. Finalizing the design of these building blocks requires further research to explore the coupling to the rest of the quasi-optical chain, as well as the compatibility of their physical dimensions with the available space. In fact, having explored the potential of these geometries and gained insight into their principles of operation as well as the techniques to analyse them and improve their performance, the next step is to consider how they can be incorporated into the final system. A concern about that is the fact that the available space inside the cryostat is limited, rendering some of the designs presented in this work not directly compatible with the available space. Therefore, it should be investigated whether it is possible to reduce the dimensions or explore other variants of these designs, at the cost of reduced performance of the system.

As for the rest of the quasi-optical chain, this includes the warm optics inside the cabin of the telescope, i.e. at room temperature, as well as the cold optics, which are cryogenically cooled inside the cryostat. A concept sketch of the TIFUUN quasi-optical chain is shown in Figure 6-1. Similar quasi-optical systems have been designed for the purpose of the DESHIMA 1.0 and 2.0 projects, with their details given in Chapter 5 of [23]. A geometrical description of the optics presented in Figure 6-1 is given in the following paragraph.

A plane wave is incident on the ASTE telescope's 10m diameter main dish and reflected towards the sub-reflector of ASTE's Cassegrain system. The wave enters the telescope's cabin near the Cassegrain focus, where the spherical wave has just started to diverge once again. Subsequently, it is incident on a reflector system placed inside the cabin of the telescope, in room temperature (warm optics). Near the focal point of the warm optics, the aperture opening of the cryostat is placed. The diverging spherical wave is then incident on the cold optics, which transform it to a locally plane wave reaching the polarizing grid. The two orthogonal polarizations of this locally plane wave are then redirected towards the two plano-hyperbolic lenses of the IFU building blocks. The details of such a quasi-optical system, such as the type and number of mirrors utilized for the warm and cold optics design, as well as their dimensioning are yet to be determined. Furthermore, further research can be conducted to

explore different alternatives on the implementation of the cold optics, for instance with the use of transmitting instead of reflecting components (i.e., lenses instead of mirrors).

▪ Another aspect of this work that is interesting for future research concerns the use of the developed efficient procedure for multi-surface shaping of lens chains, to improve the scanning performance of other architectures. In particular, in the framework of this work, a combination of multi-surface geometrical optics (GO) propagation and symmetrical shaping of lens surfaces was employed to improve the scanning performance of the geometrically coupled system. The multiple surfaces involved in this geometry provide multiple degrees of freedom for the shape optimization, which allow for the correction of phase aberrations while scanning. Furthermore, the use of GO propagation in combination with an analysis in reception makes the utilized optimization kernel very fast, and thus suitable for integration into an efficient optimization algorithm.

Such a methodology is also very interesting for the design of other types of multi-lens architectures aiming to achieve good scanning performance in all azimuthal planes, correcting both for phase errors and for spill-over losses. In particular, for smaller electrical dimensions compared to the TIFUUN case, spill-over losses due to scanning also become significant. Therefore, the optimization process discussed in this thesis, i.e. the multi-objective optimization between spill-over and taper efficiency, can become very relevant. In general, the choice of cost function such that the optimizer converges to an optimal solution depending on the requirements is a topic that requires further investigation. Architectures that can be examined with such a process are integrated multi-surface lenses, similar to [31] or [32] in a scanning configuration, as well as free-standing lenses in combination with on-chip integrated lenses, similar to the geometry examined in this work.
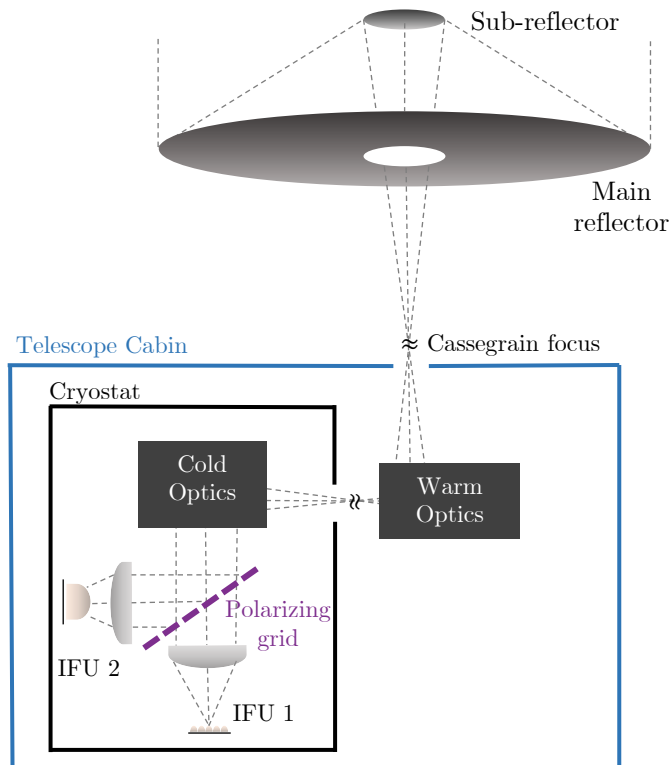
Figure 6-1. Concept sketch of the TIFUUN quasi-optical chain, coupling the radiation all the way from the ASTE telescope's main dish, to the imaging spectrometers. The QO chain is comprised of the Cassegrain system of the telescope, the warm optics, the cold optics, a polarizing grid and two IFU building blocks. Here, one IFU building block is based on the design presented in Chapter 3, while the second on the design presented in Chapter 4.

Appendices

Appendix A.
Lens Geometries

A.1. Extended Hemispherical Lens

An extended hemispherical lens is a dielectric lens type, comprised of a hemispherical part and an extension length. The properties of a wave front radiated through an extended hemispherical lens are defined by the length of the extension, with two typically used types of extended hemispherical lenses being the synthesized elliptical lens and the hyper-hemispherical one. While the synthesized elliptical lens aims to emulate the performance of an elliptical lens, i.e. locally radiate a plane wave, the hyper-hemispherical lens radiates a spherical wave, which seems to originate from its virtual focus, which is a point below the lens, at a distance F_v from its top.

a. Synthesized Elliptical   b. Hyper − Hemispherical
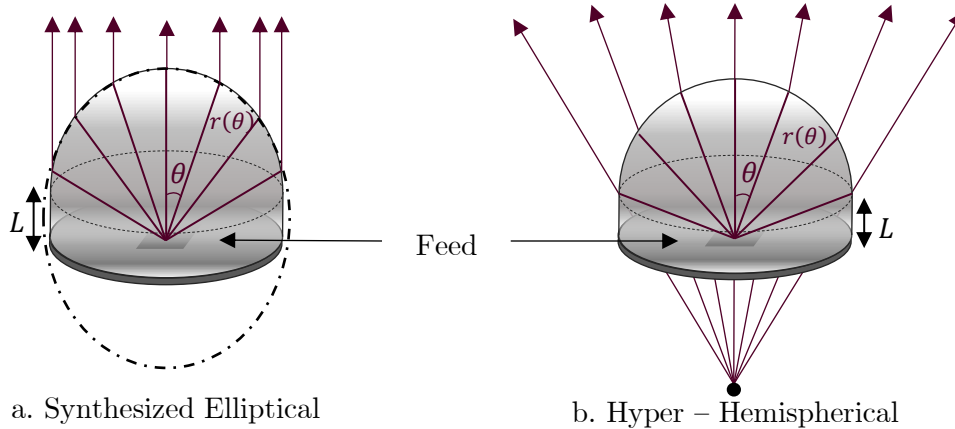
Figure A-1. Commonly used extended hemispherical lenses. In (a), a synthesized elliptical lens is shown, together with the elliptical shape it aims to emulate. In (b), a hyper-hemispherical lens is depicted, where the virtual focus of the lens is also drawn, to indicate the point from which the wave front seems to originate from.
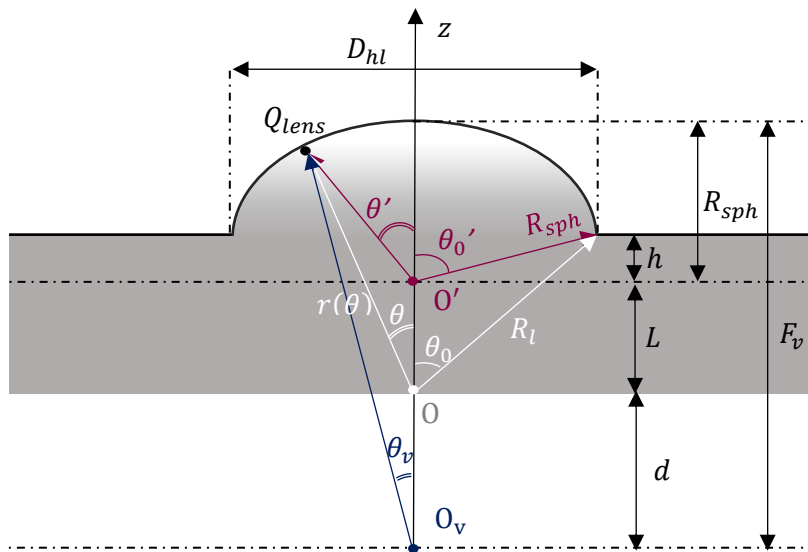
Figure A-2. Hyper-hemispherical lens geometry. Three reference systems can be used interchangeably at the analysis. One in the virtual focus, one at the feed position and one at the centre of the spherical part of the lens.

For the synthesized elliptical lens, the extension length is defined such that the shape of the lens approaches the elliptical one. For instance, for a silicon lens and a feeding element with its phase centre at point O (Figure A-2), the extension length is $L = 0.39 R_{sph}$ [33].

For the hyper-hemispherical lens, the extension length also depends on the refractive index of the material and the radius of the hemisphere R_{sph} and is given in Eq. A.1.

$$L = \frac{R_{sph}}{n}, \quad n = \sqrt{\varepsilon_r}, \tag{A.1}$$

The virtual focus position is given in Eq. A.2.

$$F_v = R_{sph}(n + 1), \tag{A.2}$$

If the lens is truncated, an extension h is also introduced, as shown in Figure A.2.

$$h = \sqrt{R_{sph}^2 - \left(\frac{D_{hl}}{2}\right)^2}, \tag{A.3}$$

For the analysis for such a lens geometry, one can interchange between three reference systems, one at the virtual focus (O_v), one at the lens base (O) and one at the centre of the hemisphere (O'). Based on the reference system centred on the base of the lens, the equation of the surface of a hyper-hemispherical lens is given in Eq. A.4.

$$z = L + \sqrt{R_{sph}^2 - \rho^2}, \tag{A.4}$$

where $\rho = \sqrt{x^2 + y^2}$, while $x, y \leq \frac{D_{hl}}{2}$.

The radial distance from the same point is given in Eq. A.5, while the subtended angle of the lens is given in Eq. A.6.

$$r(\theta) = L\cos\theta + \sqrt{R_{sph}^2 - L^2\sin^2\theta}, \tag{A.5}$$

$$\theta_0 = \tan^{-1}\left(\frac{D_{hl}}{2(h+L)}\right), \tag{A.6}$$

Finally, the rim distance is given in Eq. A.7.

$$R_l = \min\{r(\theta)\} = \frac{D_{hl}}{2\sin\theta_0}, \tag{A.7}$$

A.2. Plano – Hyperbolic Lens

A planar hyperbolic lens is a dielectric lens type, with the property of transforming a spherical wave into a plane wave and vice versa. As a result, it can be utilized as a focusing component, with its main difference with an on-axis reflector being its transmitting nature, compared to the reflecting nature of the parabola. Its bottom surface features a hyperbolic shape, while its top surface is planar, as shown in Figure A-3. The equation of the hyperbolic surface, based on a reference system centred on its focal point is given in Eq. A.8, while the radial distance $r(\theta)$ is given in Eq. A.9.
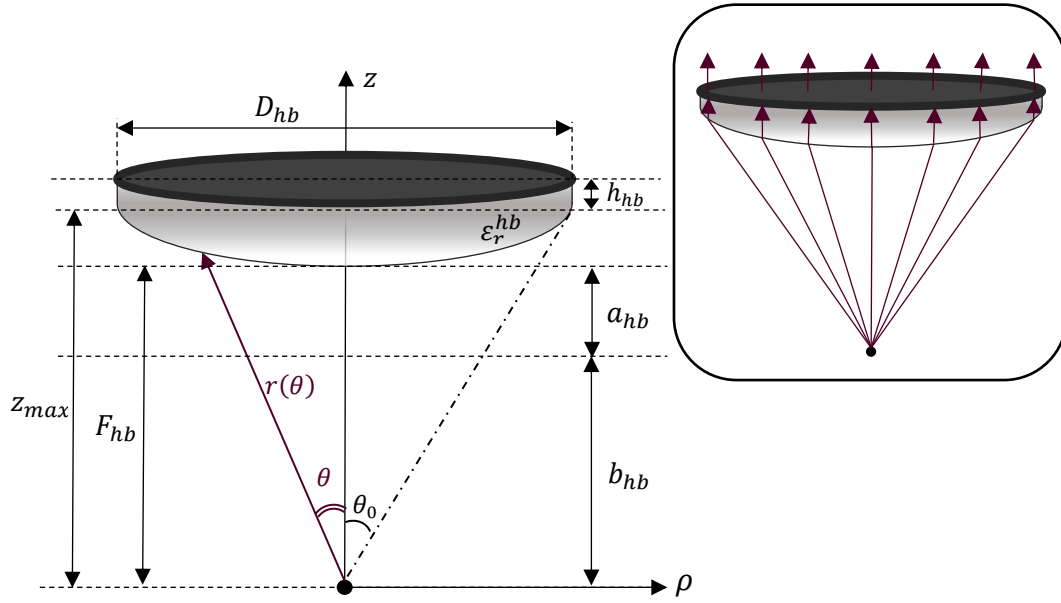
Figure A-3. Geometry of a planar hyperbolic lens.

$$\left(\frac{z-c_{hb}}{a_{hb}}\right)^2 - \left(\frac{\rho}{b_{hb}}\right)^2 = 1, \tag{A.8}$$

$$r(\theta) = -\frac{b_{hb}^2/a_{hb}}{a_{hb}-e_{hb}\cos\theta}, \tag{A.9}$$

where $e_{hb} = \sqrt{\varepsilon_r^{hb}}$ is the eccentricity of a lens with permittivity ε_r^{hb} and $a_{hb} = \frac{F_{hb}}{e_{hb}+1}$, $c_{hb} = a_{hb} \cdot e_{hb}$ and $b_{hb} = \sqrt{c_{hb}^2 - a_{hb}^2}$ are the parameters of the hyperbolic surface, as given in Figure A-3.

The subtended angle of the hyperbolic lens is then calculated as in Eq. A.10.

$$\theta_0 = \tan^{-1}\left(\frac{D_{hb}}{2z_{max}}\right), \tag{A.10}$$

where $z_{max} = a_{hb}\sqrt{1 + \left(\frac{D_{hb}}{2b_{hb}}\right)^2} + c_{hb}$, is the highest point of the hyperbola.

A.3. Elliptical Lens

One of the most commonly utilized lens types is the elliptical lens, the geometry of which is shown in Figure A-4. The elliptical lens transforms a spherical wave originating from its lower focus, to a locally plane wave, enhancing this way the directivity of any antenna.
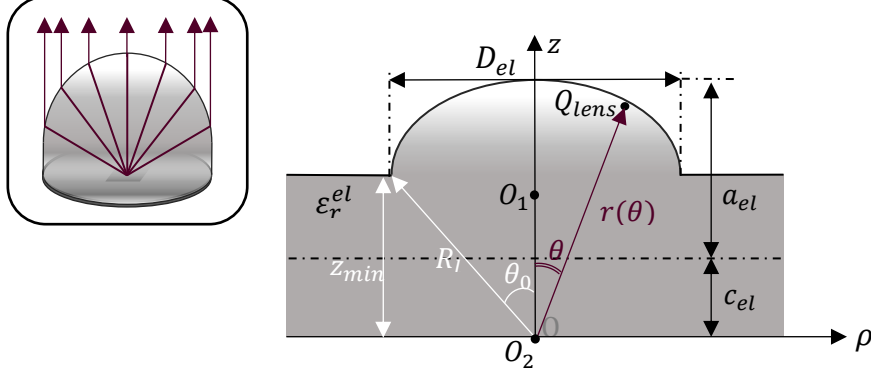
Figure A-4. Geometry of an elliptical lens.

The equation of the elliptical surface is given in Eq. A.11, while the radial distance from the lower focus of the ellipse (O_2) to its surface is given in Eq. A.12.

$$\left(\frac{z - c_{el}}{a_{el}}\right)^2 + \left(\frac{\rho}{b_{el}}\right)^2 = 1, \tag{A.11}$$

$$r(\theta) = a_{el} \cdot \frac{1 - e_{el}^2}{1 - e_{el}\cos\theta}, \tag{A.12}$$

where $e_{el} = 1/\sqrt{\varepsilon_r^{el}}$ is the eccentricity of an elliptical lens with permittivity ε_r^{el}, $c_{el} = a_{el} \cdot e_{el}$ and $b_{el} = \sqrt{a_{el}^2 - c_{el}^2}$ are the parameters of the elliptical surface, as given in Figure A-4.

Once the diameter (D_{el}) and subtended angle of the lens (θ_0) are defined, the parameter a_{el} of the ellipse, the rim distance (R_l) and the lower point of the elliptical surface (z_{min}) are given as in Eq. A.13-15.

$$R_l = \frac{D_{el}}{2\sin\theta_0}, \tag{A.13}$$

$$a_{el} = R_l \frac{1 - e_{el}\cos\theta_0}{1 - e_{el}^2}, \tag{A.14}$$

$$z_{min} = a_{el}\sqrt{1 - \left(\frac{D_{el}}{2b_{el}}\right)^2} + c_{el}, \tag{A.15}$$

For a non-truncated lens, the maximum angle for which a wave is transmitted out of the lens surface corresponds to the complementary angle of the critical angle, $\theta_0^{nt} = \pi/2 - \theta_{critical}$, where $\theta_{critical} = \sin^{-1}\left(\frac{\varepsilon_r^{out}}{\varepsilon_r^{el}}\right)$.

Appendix B.
Transmission through a generic surface

The field transmitted from a generic surface can be calculated as the product of the incident field and the transmission dyad, as in Eq. B.1.

$$\vec{E}_t = \bar{\bar{\tau}} \cdot \vec{E}_i,$$
(B.1)

The transmission dyad describes the change both in amplitude and in polarization of the incident field, when transmitted through the surface, and thus it can be written as in Eq. B.2.

$$\bar{\bar{\tau}} = T^{\parallel} \cdot \hat{p}_i^{\parallel} \cdot \hat{p}_t^{\parallel} + T^{\perp} \cdot \hat{p}_i^{\perp} \cdot \hat{p}_t^{\perp},$$
(B.2)

where $\hat{p}_{i/t}^{\parallel/\perp}$ are the unit vectors of the parallel/ perpendicular polarization, of the incident/ transmitted fields and $T^{\parallel/\perp}$ are the transmission coefficients for the two polarizations.

To calculate the polarization vectors, the propagation unit vectors associated to the incident, as well as the transmitted fields are required. The propagation unit vector of the incident field depends on the wave front type (for a spherical wave front it is a radial vector), while the one of the transmitted field can be derived using the vectorial version of Snell's Law. The final expressions are given in Eq. B.4, while the normal unit vector to a surface $\vec{Q}$ is given in Eq. B.3.

$$\hat{n}_Q = \pm \frac{\frac{\partial \bar{Q}}{\partial \theta} \times \frac{\partial \bar{Q}}{\partial \varphi}}{\left| \frac{\partial \bar{Q}}{\partial \theta} \times \frac{\partial \bar{Q}}{\partial \varphi} \right|},$$
(B.3)

$$\hat{s}_t = \sqrt{\frac{\varepsilon_r^i}{\varepsilon_r^t}} \cdot \hat{s}_i - \left[\sqrt{\frac{\varepsilon_r^i}{\varepsilon_r^t}} (\hat{s}_i \cdot \hat{n}_Q) + \sqrt{\frac{1}{\varepsilon_r^t}} \sqrt{\varepsilon_r^t - \varepsilon_r^i \left(1 - (\hat{s}_i \cdot \hat{n}_Q)^2 \right)} \right] \cdot \hat{n}_Q,$$
(B.4)

where ε_r^i is the permittivity of the first medium, where the field is incident on the surface and ε_r^t is the permittivity of the second medium, where the field is transmitted.

The polarization unit vector for the perpendicular (TE) polarization is always normal to the plane of incidence, thus it can be expressed as the unit vector of the cross product between any pair of vectors that are parallel to the plane of incidence. Thus, it is convenient to express it as the unit vector of the cross product between the propagation unit vector $(\hat{s}_{i/t})$ and the normal unit vector to the lens surface $(\hat{n}_Q)$. The polarization unit vector for the parallel (TM) polarization is then perpendicular to both the direction of propagation and to the perpendicular (TE) polarization and thus it is expressed as the cross product of the perpendicular polarization unit vector $(\hat{p}_{i/t}^{\perp})$ and the propagation unit vector $(\hat{s}_{i/t})$, as in Eq. B.5.

$$\begin{aligned} \hat{p}_{i/t}^{\perp} &= \frac{\hat{s}_{i/t} \times \hat{n}_Q}{|\hat{s}_{i/t} \times \hat{n}_Q|} \\ \hat{p}_{i/t}^{\parallel} &= \hat{p}_{i/t}^{\perp} \times \hat{s}_{i/t} \end{aligned},$$
(B.5)

Once those are known, the angles of incidence/transmission can be calculated through the dot products between the propagation vectors and the normal vector, as in Eq. B.6.

$$cos\theta_{i/t} = -\hat{s}_{i/t} \cdot \hat{n}_Q,$$
(B.6)

The Fresnel transmission coefficients are calculated in the following sections. The transmitted field can then be calculated from Eq. B.1, which is equivalent to:

$$\vec{E} = \left(T^\perp \cdot E_i^\perp\right) \cdot \hat{p}_t^\perp + \left(T^\perp \cdot E_i^\parallel\right) \cdot \hat{p}_t^\parallel$$

In the following sections, the Fresnel transmission and reflection coefficients are defined for two different scenarios, a generic surface with and without a relatively thin matching layer. While in both cases the derived coefficients arise from the boundary conditions applied to the respective surface(s), when a matching layer is present, the oblique incidence problem becomes more cumbersome and thus it is more convenient to represent the geometry and approach the solution via a transmission line model.

B.1. Fresnel Transmission Coefficients, surface without a matching layer

In the Physical Optics approximation, the transmission through an electrically large generic surface can be approached by considering the incident field impinging on a locally flat surface. Thus, the transmission/reflection coefficients can be calculated by imposing the boundary conditions on both the electric and the magnetic field. To solve such a problem, the fields are analyzed as a superposition of a parallel and a perpendicular to the plane of incidence components (Figure B-1). As a result, after imposing the boundary conditions for the two problems, the transmission/ reflection coefficients are given for the two components/ polarizations as in Eq. B.7.
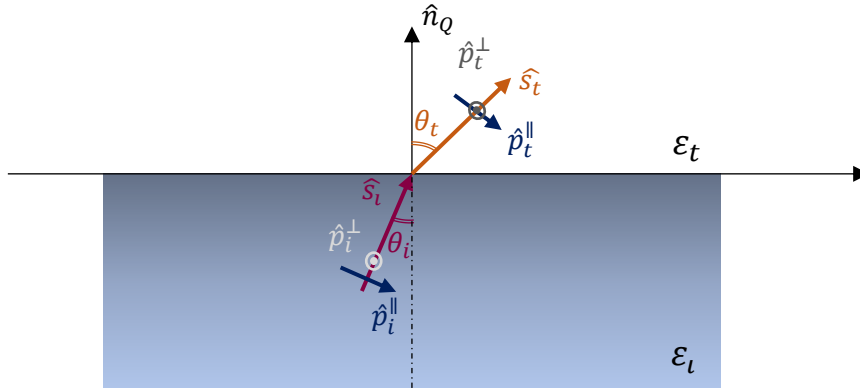
Figure B-1. Oblique Incidence on a locally flat interface between two mediums.

$$\begin{aligned}
T^\parallel &= \frac{2\zeta_t \cos\theta_i}{\zeta_i \cos\theta_i + \zeta_t \cos\theta_t} & \Gamma^\parallel &= \frac{\zeta_i \cos\theta_i - \zeta_t \cos\theta_t}{\zeta_i \cos\theta_i + \zeta_t \cos\theta_t} \\
T^\perp &= \frac{2\zeta_t \cos\theta_i}{\zeta_t \cos\theta_i + \zeta_i \cos\theta_t} & \Gamma^\perp &= \frac{\zeta_t \cos\theta_i - \zeta_i \cos\theta_t}{\zeta_i \cos\theta_i + \zeta_t \cos\theta_t}
\end{aligned} \tag{B.7}$$

where $\zeta_{i/t} = Z_0/\sqrt{\varepsilon_{i/t}}$ is the impedance of the medium in which the field is incident/ transmitted and $\theta_{i/t}$ is the angle of incidence/transmission. This is defined through the dot product between the propagation vector and the normal vector (Eq. B.6).

B.2. Fresnel Transmission Coefficients, Surface with a thin matching layer

In the case that there is a relatively thin matching layer between the two surfaces, the transmission/ reflection coefficients can be approximated using an equivalent transmission line problem for each field component/ polarization. Such a problem is shown in Figure B-3, with the difference between the two problems lying in the definition of the characteristic impedance of the medium (Eq. B.8), as well as the voltage – electric field relation.

$$\begin{aligned}
Z_m^\parallel &= \zeta_m \frac{k_{z_m}}{k} \\
Z_m^\perp &= \zeta_m \frac{k_m}{k_{z_m}}
\end{aligned} \tag{B.8}$$

The equivalent transmission line problem is defined using the electric field components tangential to the surface where the field is incident (transversed equivalent transmission line). This way, the electric field is continuous and thus the voltage continuity can be applied in every stratification. As such, the voltage wave defined for the transmission line problem is equal to:

- ▪ The perpendicular electric field for the perpendicular (TE) polarization.
- ▪ The tangential to the surface component of the electric field, for the parallel (TM) polarization (Figure B-2).

$$
\begin{aligned}
V^\perp &= E^\perp \\
V^\parallel &= E^\parallel \cos\theta
\end{aligned} \tag{B.9}
$$

It is noted that the problem is solved assuming propagation towards z (Eq. B.10). In a generic case, where the propagation of the incident field is towards $\hat{s}_i$, the angle of incidence/transmission is defined between the direction normal to the surface and the direction of propagation (Eq. B.6).

$$
k_{zm} = -j\sqrt{-\left(k_m^2 - k_{\rho_m}{}^2\right)}, \tag{B.10}
$$
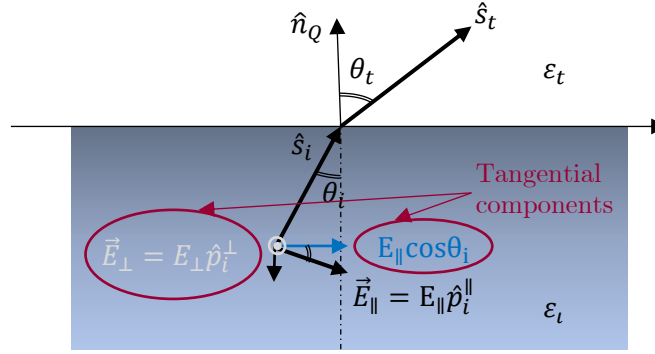
Figure B-2. Tangential components decomposition in a plane wave incidence scenario
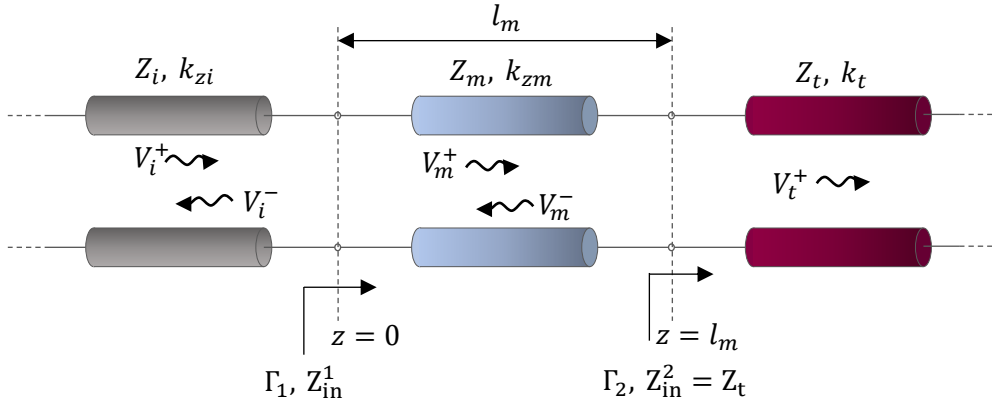
Figure B-3. Equivalent transmission line problem for a surface with a matching layer. For each polarization, one such problem is solved to derive the respective transmission/ reflection coefficients.

The transmission coefficients relating the field incident at $z = 0$ and transmitted at $z = l_m$ are:

$$
\begin{aligned}
T^\parallel &= \frac{E_t^\parallel(z=l_m)}{E_i^\parallel(z=0)} = \frac{V_t^{+\parallel}(z=l_m)}{V_i^{+\parallel}(z=0)} \cdot \frac{\cos\theta_i}{\cos\theta_t} \\
T^\perp &= \frac{E_t^\perp(z=l_m)}{E_i^\perp(z=0)} = \frac{V_t^{+\perp}(z=l_m)}{V_i^{+\perp}(z=0)}
\end{aligned}, \tag{B.11}
$$

The general expressions for the voltages in the three mediums are given in Eq. B.12.

$$V_i^{\parallel/\perp} = V_i^{+\parallel/\perp} e^{-jk_{zi}z} \left(1 + \frac{V_i^{-\parallel/\perp}}{V_i^{+\parallel/\perp}} e^{2jk_{zi}z}\right), \quad \frac{V_i^{-\parallel/\perp}}{V_i^{+\parallel/\perp}} = \Gamma_1^{\parallel/\perp}$$

$$V_m^{\parallel/\perp} = V_m^{+\parallel/\perp} e^{-jk_{zm}z} \left(1 + \frac{V_m^{-\parallel/\perp}}{V_m^{+\parallel/\perp}} e^{2jk_{zm}z}\right), \quad \frac{V_m^{-\parallel/\perp}}{V_m^{+\parallel/\perp}} = \Gamma_2^{\parallel/\perp} e^{-2jk_{zm}l_m}, \tag{B.12}$$

$$V_t = V_t^+ e^{-jk_{zt}z}$$

where the reflection coefficients at the two surfaces are given in Eq. B.13.

$$\Gamma_1^{\parallel/\perp} = \frac{Z_{in}^{1\ \parallel/\perp} - Z_i^{\parallel/\perp}}{Z_{in}^{1\ \parallel/\perp} + Z_i^{\parallel/\perp}}, \qquad Z_{in}^{1\ \parallel/\perp} = Z_m^{\parallel/\perp} \frac{Z_t^{\parallel/\perp} + jZ_m^{\parallel/\perp} \tan(k_{zm}l_m)}{Z_m^{\parallel/\perp} + jZ_t^{\parallel/\perp} \tan(k_{zm}l_m)},$$

$$\Gamma_2^{\parallel/\perp} = \frac{Z_{in}^{2\ \parallel/\perp} - Z_m^{\parallel/\perp}}{Z_{in}^{2\ \parallel/\perp} + Z_m^{\parallel/\perp}}, \qquad Z_{in}^{2\ \parallel/\perp} = Z_t^{\parallel/\perp} \tag{B.13}$$

To calculate the ratios defined in Eq. B.11, one needs to apply the continuity of the voltage on the two stratifications.

- At $z = 0$:

$$V_i^{\parallel/\perp}(z = 0) = V_m^{\parallel/\perp}(z = 0) \Rightarrow \frac{V_m^{+\parallel/\perp}}{V_i^{+\parallel/\perp}(z = 0)} = \frac{1 + \Gamma_1^{\parallel/\perp}}{1 + \Gamma_2^{\parallel/\perp} e^{-2jk_{zm}l_m}}$$

- At $z = l_m$:

$$V_m^{\parallel/\perp}(z = l_m) = V_t^{\parallel/\perp}(z = l_m) \Rightarrow \frac{V_t^{\parallel/\perp}(z = l_m)}{V_m^{+\parallel/\perp}} = e^{-jk_{zm}l_m}\left(1 + \Gamma_2^{\parallel/\perp}\right)$$

Thus, the voltage ratio in Eq. B.11 is given in Eq. B.14 to complement the derivation of the transmission coefficients.

$$\frac{V_t^{+\parallel/\perp}(z=l_m)}{V_i^{+\parallel/\perp}(z=0)} = \frac{e^{-jk_{zm}l_m}\left(1 + \Gamma_1^{\parallel/\perp}\right)\left(1 + \Gamma_2^{\parallel/\perp}\right)}{1 + \Gamma_2^{\parallel/\perp} e^{-2jk_{zm}l_m}}, \tag{B.14}$$

The final expressions for the Fresnel Transmission coefficients, with the presence of a thin matching layer are given in Eq. B.15.

$$T^{\parallel} = \frac{e^{-jk_{zm}l_m}\left(1 + \Gamma_1^{\parallel}\right)\left(1 + \Gamma_2^{\parallel}\right)}{1 + \Gamma_2^{\parallel} e^{-2jk_{zm}l_m}} \cdot \frac{cos\theta_i}{cos\theta_t}$$

$$T^{\perp} = \frac{e^{-jk_{zm}l_m}\left(1 + \Gamma_1^{\perp}\right)\left(1 + \Gamma_2^{\perp}\right)}{1 + \Gamma_2^{\perp} e^{-2jk_{zm}l_m}}, \tag{B.15}$$

Appendix C.
Ray Tracing

The GO propagation is very closely related to the ray picture, since the field on each point on the surface S is calculated through the dominantly contributing ray, i.e. the one following the direction of propagation of the field (Eq. C.1, Figure C-1).

$$\vec{E}(P) = \vec{E}(P_1) \sqrt{\frac{\rho_1 \rho_2}{(\rho_1 + s)(\rho_2 + s)}} \cdot e^{-jks}, \tag{C.1}$$

where $\rho_{1,2}$ the radii of curvature of the respective wave-front.

Thus, in order to calculate the field at a point $P(X, Y, Z)$ on the surface S, one needs to calculate the distance s between the dominant source point $P_1(X_1, Y_1, Z_1)$ and the surface point $P(X, Y, Z)$. To calculate those, the ray tracing equations given in Eq. C.2 are utilized.

$$X = X_1 + k_x s, \tag{C.2.a}$$
$$Y = Y_1 + k_y s, \tag{C.2.b}$$
$$Z = Z_1 + k_z s, \tag{C.2.c}$$

where $\hat{k} = k_x \hat{x} + k_y \hat{y} + k_z \hat{z}$ the unit vector of the direction of propagation.

In case the equations of the final surface (defined in the form $Z = f(X, Y)$) is simple, the ray tracing equations can be solved analytically, as shown below.

$$Z = f(X, Y) \xrightarrow{(C.2.a),\,(C.2.b)} Z = f(X_1, Y_1, k_x, k_y, s)$$
$$\xrightarrow{(C.2.c)} Z_1 + k_z s = f(X_1, Y_1, k_x, k_y, s)$$

with the only unknown being the distance between the two surfaces, s.

When the equation of the surface becomes more complicated, a numerical method can be utilized instead to derive both the distance s, and the coordinates of $P(X, Y, Z)$. One such method, based on the Newton-Raphson iteration technique [34], is described below.

General Ray Tracing - Iterative Method

The ray tracing technique currently described can be divided in two steps, where the first step is simply included to ensure the convergence of the second. In particular, in the first step one can calculate the distance (s_0) between the surface S and a planar surface with constant $Z = Z_0$. Subsequently, a numerical method can be employed to calculate the distance d between the plane $Z = Z_0$ and the surface S, as shown in Figure C-1.

Then, the original unknown distance s (between the source and the surface S) is calculated by subtracting the two, i.e. $s = s_0 - d$. The steps of this methodology are analytically described below.

1. Calculate the distance from the source to a plane with $Z = Z_0$.

The ray tracing equations to find the coordinates $P_0(X_0, Y_0, Z_0)$ and the distance s_0 are given in Eq. C.3.

$$X_0 = X_1 + k_x s_0, \tag{C.3.a}$$
$$Y_0 = Y_1 + k_y s_0, \tag{C.3.b}$$
$$Z_0 = Z_1 + k_z s_0, \tag{C.3.c}$$

Since Z_0 is constant and known (chosen for convergence), s_0 is calculated through Eq. C.3.c, as:

$$s_0 = \frac{Z_0 - Z_1}{k_z}, \tag{C.4}$$

2. Calculate the distance between the plane $Z = Z_0$ and the surface S.

The ray tracing equations to find the coordinates of $P(X, Y, Z)$ and the distance d are given in Eq. C.5.

$$X = X_0 + k_x d, \tag{C.5.a}$$
$$Y = Y_0 + k_y d, \tag{C.5.b}$$
$$Z = Z_0 + k_z d, \tag{C.5.c}$$

The problem now is to calculate the distance d, such that the point P satisfies the equation of the surface S. Here, an iterative Newton-Raphson technique, as the one given in [34], is employed. In fact, the distance is recalculated in each iteration, based on a reference value, which is the distance derived in the previous iteration, as expressed in Eq. C.6.

$$d_{j+1} = d_j - \frac{F(X_j, Y_j, Z_j)}{F'(X_j, Y_j, Z_j)}, \quad \begin{matrix} X_j = X_0 + k_x d_j \\ Y_j = Y_0 + k_y d_j \, , \\ Z_j = Z_0 + k_z d_j \end{matrix} \tag{C.6}$$

where $F'(X_j, Y_j, Z_j)$ is the directional derivative[3] of F, along the direction of propagation $\hat{k}(k_x, k_y, k_z)$ (Eq. C.7).

$$F'(X_j, Y_j, Z_j) = \nabla_{\hat{k}} F(X_j, Y_j, Z_j) = \frac{\partial F}{\partial s} |_{d=d_j} \Rightarrow$$

$$F'(X_j, Y_j, Z_j) = \left(\frac{\partial F}{\partial X} \cdot k_x + \frac{\partial F}{\partial Y} \cdot k_y + \frac{\partial F}{\partial Z} \cdot k_z \right)_{d=d_j}, \tag{C.7}$$

The initial condition of the iterative procedure is given as $d_1 = 0$ while the process is terminated when the condition $|d_f - d_{f-1}| < \varepsilon$ is satisfied. The chosen value of the acceptable error ε depends on the desired accuracy. In order for the starting condition $d_1 = 0$ to ensure convergence, the intermediate plane $Z = Z_0$ should be chosen very carefully. For a rotationally symmetric surface S, it is convenient to define Z_0 as the maximum or minimum Z coordinate of the surface (depending on the concavity of the surface).

A generic rotationally symmetric surface can be expressed through a conic surface expression, as in Eq. C.8.

$$F(X, Y, Z) = Z - \alpha_0 - \frac{c\rho^2}{1 + \sqrt{1 - \kappa c^2 \rho^2}} - \sum_{i=1}^{N} a_i \rho^{2i} = 0, \tag{C.8}$$

with c being the vertex curvature of the surface and κ the conic constant. The derivatives of this surface are then given as in Eq. C.9.

$$\frac{\partial F}{\partial X} = -X \left[c\sqrt{1 - \kappa c^2 \rho^2} + 2 \sum_{i=1}^{N} \{ i \cdot a_i \cdot \rho^{2(i-1)} \} \right]$$
$$\frac{\partial F}{\partial Y} = -Y \left[c\sqrt{1 - \kappa c^2 \rho^2} + 2 \sum_{i=1}^{N} \{ i \cdot a_i \cdot \rho^{2(i-1)} \} \right], \tag{C.9}$$
$$\frac{\partial F}{\partial Z} = 1$$

---

[3] The directional derivative $\nabla_{\hat{k}} F(X_j, Y_j, Z_j)$ is the rate at which the function F changes at a point (X_j, Y_j, Z_j) in the direction $\hat{k}$.
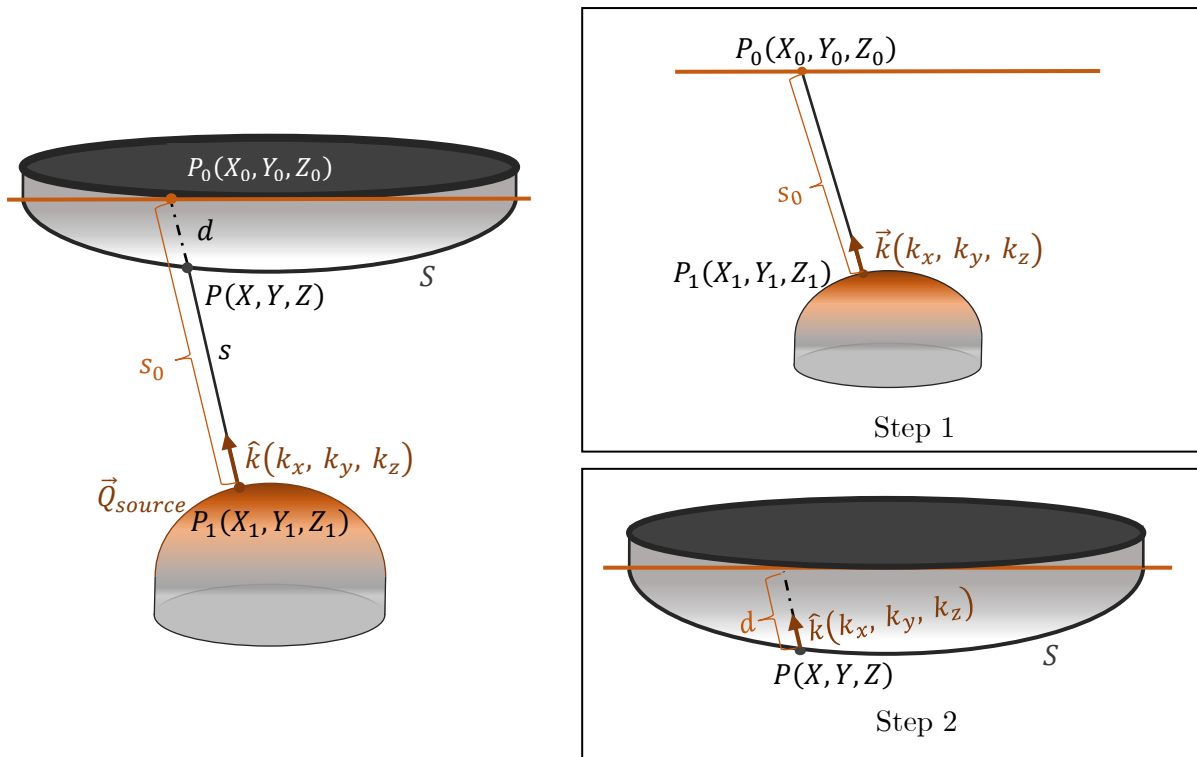
Figure C-1. Ray Tracing between Generic Surfaces. The process is split in two steps to ensure convergence. The first step calculates the distance to a planar surface, while the second step involves the calculation of the distance between the plane and the final surface S.

Appendix D.
Symmetric Shaping of Dielectric Lenses

Shaping dielectric lenses can be utilized as a technique to correct for phase aberrations, as well as spill-over losses while scanning. It can be either symmetric or asymmetric, but in this work only symmetric shaping is discussed. To make the shaping process more efficient, the lens profile can be expressed as a conic surface plus higher order polynomials. Then, the shape of the surface can be optimized utilizing its curvature (c), its conic constant (κ), as well as the weights of the higher order polynomial, a_i.

$$z = \frac{c\rho^2}{1+\sqrt{1-\kappa c^2 \rho^2}} + a_0 + \sum_{i=1}^{N} a_i \rho^{2i}, \tag{D.1}$$

where $\rho = \sqrt{x^2 + y^2}$.

The optimization of the surface can be performed by utilizing an optimization algorithm. In this case, a multi-objective genetic algorithm ("gamultiobj" of matlab) is used. The objectives are defined as cost functions that need to be minimized. The choice of the objective functions is a very important aspect of the optimization, determining the convergence of the genetic algorithm to an optimal solution, depending on the system requirements.

In the case that both spill-over and phase losses need to be corrected, the cost functions can be defined as the inverse of the taper and spill-over efficiencies of the quasi-optical system, to ensure that the maximization of the aperture efficiency is not performed at the cost of one of the two terms. If the shaping affects only the phase matching, the inverse of the aperture efficiency can be directly utilized as one of the cost function. The output of the optimization algorithm is a set of solutions, each achieving a different trade-off between the objective functions.

As a starting point for the optimization, it is convenient to use a canonical geometry, express it in terms of a conic surface and subsequently tweak its curvature, conical constant and vertical position with respect to the feeding element to minimize the required objective function. Some well-known canonical geometries expressed as conic surfaces are given below.

Lens Type	Equation	Curvature c	Conical Constant κ	Vertical position a_0
Extended Hemispherical	$z = R_{sph}\sqrt{1 - \frac{\rho^2}{R_{sph}^2}} + L$	$-\dfrac{1}{R_{sph}}$	1	$R_{sph} + L$
Elliptical	$z = a_{el}\sqrt{1 - \frac{\rho^2}{b_{el}^2}} + c_{el}$	$-\dfrac{a_{el}}{b_{el}^2}$	$\left(\dfrac{b_{el}}{a_{el}}\right)^2$	$a_{el} + c_{el}$
Hyperbolic	$z = a_{hb}\sqrt{1 + \frac{\rho^2}{b_{hb}^2}} + c_{hb}$	$\dfrac{a_{hb}}{b_{hb}^2}$	$-\left(\dfrac{b_{hb}}{a_{hb}}\right)^2$	$a_{hb} + c_{hb}$

Bibliography

[1]   J. J. Condon and S. M. Ransom, "Spectral Lines," in *Essential Radio Astronomy*, Princeton Series in Modern Observational Astronomy, 2016.

[2]   M. Janssen, H. Falcke, M. Kadler, E. Ros, M. Wielgus, K. Akiyama, M. Baloković, L. Blackburn, K. Bouman, A. Chael, C. Chan, K. Chatterjee, J. Davelaar, P. Edwards, C. Fromm, J. Gómez, C. Goddi, S. Issaoun, M. Johnson, J. Kim, J. Koay, T. Krichbaum, J. Liu, E. Liuzzo, S. Markoff, A. Markowitz, D. P. Marrone, Y. Mizuno, C. Müller, C. Ni, D. W. Pesce, V. Ramakrishnan, F. Roelofs, K. L. Rygl, I. van Bemmel and The Event Horizon Telescope Collaboration, "Event Horizon Telescope observations of the jet launching and collimation in Centaurus A," *Nature Astronomy,* vol. 5, p. 1017–1028, 2021.

[3]   M. D. Shaw, J. Bueno, P. Day, C. M. Bradford and P. M. Echternach, "Quantum capacitance detector: A pair-breaking radiation detector based on the single Cooper-pair box," *Physical Review,* vol. B, no. 79, pp. 144511-1 - 144511-10, 2009.

[4]   P. M. Echternach, K. J. Stone, C. M. Bradford, P. K. Day, D. W. Wilson, K. G. Megerian, N. Llombart and J. Bueno, "Photon shot noise limited detection of terahertz radiation using a quantum capacitance detector," *Appl. Phys. Lett.,* vol. 103, pp. 053510-1 - 053510-5, 2013.

[5]   T. Suzuki, P. Khosropanah, M. L. Ridder, R. A. Hijmering, J. R. Gao, H. Akamatsu, L. Gottardi, J. v. d. Kuur and B. D. Jackson, "Development of Ultra-Low-Noise TES Bolometer," *J. Low Temp. Phys.,* vol. 184, pp. 52-59, 2015.

[6]   B. S. Karasik and R. Cantor, "Demonstration of high optical sensitivity in far-infrared hot-electron bolometer," *Appl. Phys. Lett.,* vol. 98, no. 193503, pp. 1-3, 2011.

[7]   P. J. d. Visser, J. J. A. Baselmans, J. Bueno, N. Llombart and T. M. Klapwijk, "Fluctuations in the electron system of a superconductor exposed to a photon flux," *Nat. Commun.,* vol. 4, no. 3130, pp. 1-8, 2014.

[8]   J. J. A. Baselmans, J. Bueno, S. J. C. Y. O. Yurduseven, N. Llombart, K. Karatsu, A. M. Baryshev, L. Ferrari, A. Endo, D. J. Thoen, P. J. d. Visser, R. M. J. Janssen, V. Murugesan, E. F. C. Driessen, G. Coiffard, J. Martin-Pintado, P. Hargrave and M. Griffin, "A kilo-pixel imaging system for future space based far-infrared observatories using microwave kinetic inductance detectors," *A&A,* vol. A89, pp. 1-16, 2017.

[9]   E. S. Observatory, "Integral Field Units," [Online]. Available: https://www.eso.org/public/teles-instr/technology/ifu/.

[10]   A. Endo, P. v. d. Werf, R. Janssen, P. d. Visser, T. Klapwijk, J. Baselmans, L. Ferrari, A. Baryshev and S. Yates, "Design of an Integrated Filterbank for DESHIMA: On-Chip Submillimeter Imaging Spectrograph Based on superconducting resonators," *J. Low Temp. Phys.,* vol. 167, pp. 341-346, 2012.

[11]   A. Endo, K. Karatsu, Y. Tamura, T. Oshima, A. Taniguchi, T. Takekoshi, S. Asayama, T. J. L. C. Bakx, S. Bosma, J. Bueno, K. Wuy Chin, Y. Fujii, K. Fujita, R. Huiting, S. Ikarashi, T. Ishida, S. Ishii, R. Kawabe, T. Klapwijk, K. Kohno, A. Kouchi, N. Llombart, J. Maekawa, V. Murugesan, S. Nakatsubo, M. Naruse, K. Ohtawara, A. Pascual Laguna, J. Suzuki, K. Suzuki, D. J. Thoen, T. Tsukagoshi, T. Ueda, P. de Visser, P. P. van der Werf, S. J. C. Yates, Y. Yokoshimura, O.

Yurduseven and J. J. A. Baselmans, "First light demonstration of the integrated superconducting spectrometer," *Nat. Astron.,* vol. 3, pp. 989-996, 2019.

[12]   S. v. Berkel, O. Yurduseven, A. Freni, A. Neto and N. Llombart, "THz Imaging Using Uncooled Wideband Direct Detection Focal Plane Arrays," *IEEE Trans. Terahertz Sci. Technol.,* vol. 7, no. 5, pp. 481-492, 2017.

[13]   R. Olsson, P.-S. Kildal and S. Weinreb, "The Eleven Antenna: A Compact Low-Profile Decade Bandwidth Dual Polarized Feed for Reflector Antennas," *IEEE Trans. Antennas Propag.,* vol. 54, no. 2, pp. 368-375, 2006.

[14]   A. Akgiray, S. Weinreb, W. A. Imbriale and C. Beaudoin, "Circular Quadruple-Ridged Flared Horn Achieving Near-Constant Beamwidth Over Multioctave Bandwidth: Design and Measurements," *IEEE Trans. Antennas Propag.,* vol. 61, no. 3, pp. 1099-1108, 2012.

[15]   A. Gonzalez, K. Kaneko and S. Asayama, "Recent work on (Sub-)Mm-wave ultra wideband corrugated horns for radio astronomy," in *EuCAP*, Paris, France, 2017.

[16]   M. Ivashina, M. Kehn, P.-S. Kildal and R. Maaskant, "Decoupling efficiency of a wideband vivaldi Focal Plane Array feeding a reflector antenna," *IEEE Trans. Antennas Propag.,* vol. 57, no. 2, pp. 373-382, 2009.

[17]   J. Johansson, "Tapered slot antennas and focal plane imaging systems," Ph.D. dissertation, School Elect. Comput. Eng, Chalers Univ. Technol., Gothenburg, Swedden, 1988.

[18]   M. A. Campo, D. Blanco, S. Bruni, A. Neto and N. Llombart, "On the Use of Fly's Eye Lenses with Leaky-Wave Feeds for Wideband Communications," *IEEE Trans. Antennas Propag.,* vol. 68, no. 4, pp. 2480 - 2493, 2020.

[19]   S. O. Dabironezare, G. Carluccio, A. Freni, A. Neto and N. Llombart, "Coherent Fourier Optics Model for the Synthesis of Large Format Lens-Based Focal Plane Arrays," *IEEE Trans. Antennas, Propag.,* vol. 69, no. 2, pp. 734-746, 2021.

[20]   E. Gandini, A. Tamminen, A. Luukanen and N. Llombart, "Wide Field of View Inversely Magnified Dual-Lens for Near-Field Submilimeter Wavelength Imagers," *IEEE Trans. Antennas, Propag.,* vol. 66, no. 2, pp. 541-549, 2018.

[21]   C. A. Balanis, Advanced Engineering Electromagnetics, John Wiley & Sons, Inc., 1989.

[22]   M. Albani, G. Carluccio and P. H. Pathak, "Uniform Ray Description for the PO Scattering by Vertices in Curved Surface With Curvilinear Edges and Relatively General Boundary Conditions," *IEEE Trans. Antennas Propag.,* vol. 59, no. 5, pp. 1587-1596, 2011.

[23]   S. O. Dabironezare, "Fourier Optics Field Representations for the Design of Wide Field-of-View Imagers at Sub-millimetre Wavelengths," PhD Thesis, Delft University of Technology, Delft, the Netherlands, 2020.

[24]   G. L. James, "Geometrical Optics," in *Geometrical theory of diffraction for electromagnetic waves*, London and New York, Institution of Electrical Engineers, 1980, pp. 94-114.

[25]   "CST Microwave Studio," [Online]. Available: http://www.cst.com.

[26]   O. Yurduseven, "Wideband Integrated Lens Antennas for Terahertz Deep Space Investigation," PhD Thesis, Delft University of Technology, Delft, The Netherlands, 2016.

[27]   O. Yurduseven, N. Llombart and A. Neto, "A Dual-Polarized Leaky Lens Antenna for Wideband Focal Plane Arrays," *IEEE Trans. Antennas, Propag.,* vol. 64, no. 8, pp. 3330-3337, 2016.

[28]   A. Neto, "UWB, Non Dispersive Radiation From the Planarly Fed Leaky Lens Antenna— Part 1: Theory and Design," *IEEE Trans. Antennas Propag.,* vol. 58, no. 7, pp. 2238-2247, 2010.

[29]   Y. Khusanova, M. Béthermin, O. L. Fèvre, P. Capak, A. L. Faisst, D. Schaerer, J. D. Silverman, P. Cassata, L. Yan, M. Ginolfi, Y. Fudamoto, F. Loiacono, R. Amorin, S. Bardelli, M. Boquien, A. Cimatti, M. Dessauges-Zavadsky, C. Gruppioni, N. P. Hathi, . G. C. Jones, A. M. Koekemoer, G. Lagache, R. Maiolino, B. C. Lemaux, P. Oesch, F. Pozzi, D. A. Riechers, M. Romano, M. Talia, S. Toft, D. Vergani, G. Zamorani and E. Zucca, "The ALPINE-ALMA [CII] Survey: Obscured Star Formation Rate Density and Main Sequence of star-forming galaxies at z>4," *A&A,* vol. 649, pp. A152, 1-18, 2021.

[30]   T. Mroczkowski, D. Nagai, P. Andreani, M. Arnaud, J. Bartlett, N. Battaglia, K. Basu, E. Bulbul, J. Chluba, E. Churazov, C. Cicone, A. Crites, N. DeNigris, M. Devlin, L. D. Mascolo, S. Dicker, M. Gaspari, S. Golwala, F. Guglielmetti, J. C. Hill, P. Klaassen, T. Kitayama, R. Kneissl, K. Kohno, E. Komatsu, M. Lacy, B. Mason, K. Nyland, C. Romero, J. Sayers, N. Sehgal, S. Simon, R. Sunyaev, G. Wilson, M. Zemcov and J. ZuHone, "A High-resolution SZ View of the Warm-Hot Universe," *arXiv:1903.02595 [astro-ph.CO],* 2019.

[31]   N. v. Rooijen, M. A. delPino, M. Spirito and N. Llombart, "Core-Shell Leaky-Wave Lens Antenna for 150GHz Fly's Eye Communication Systems," in *IRMMW-THz*, Delft, the Netherlands, 2022.

[32]   M. G. S. a. C. A. F. Jorge R. Costa, "Evaluation of a Double-Shell Integrated Scanning Lens Antenna," *IEEE Antennas Wirel. Propag. Lett.,* vol. 7, pp. 781-784, 2008.

[33]   D. F. Filipovic, S. S. Gearhart and G. M. Rebeiz, "Double-Slot Antennas on Extended Hemispherical and Elliptical Silicon Dielectric Lenses," *IEEE Trans. Microw. Theory Tech.,* vol. 41, no. 10, pp. 1738-1749, 1993.

[34]   G. H. Spencer and M. K. Murty, "General Ray-Tracing Procedure," *Journal of the Optical Society,* vol. 52, no. 6, pp. 672-678, 1961.